Orcutt, J.A., Schultz, A., Davies, T.A., et al., 2003
Proceedings of the Ocean Drilling Program, Initial Reports Volume 203

3. Site 1243[1]

Shipboard Scientific Party[2]

SUMMARY

Site 1243, located in the eastern equatorial Pacific, is in a particularly advantageous location for understanding the interplay between ocean chemistry, productivity, climate, and plate tectonics in a fast-spreading environment. The climatic implications were studied in detail at a series of 11 holes during Leg 138. We chose to drill Site 1243 in the immediate vicinity of Site 852, drilled during Leg 138, to develop a cased legacy hole for purposes of supporting a long-term seafloor observatory.

The age of the lithosphere in this region, based on both a full spreading rate of 141 mm/yr and an East Pacific Rise subsidence curve, is in the range of 10–12 Ma; the age is also consistent with paleoceanographic results from Leg 138. The water depth is 3882 m at the location of Hole 1243A. Based on seismic profiles collected in the original site survey for Leg 138, new seismic profiles collected as we approached the site, as well as drilling at Site 852, we estimated the sediment thickness to be 120 ± 11 m. The actual sediment thickness was 117 m, essentially the same as that found during Leg 138.

The primary objective of Leg 203 at Site 1243 was to establish a deep cased legacy hole in a geographical region identified by a number of studies (e.g., Purdy, 1995) and agreed upon by the International Ocean Network (ION) as essential to the establishment of an unbiased global distribution of broadband digital seismic observatories. The target site was designated Ocean Seismic Network (OSN)-2 after the U.S.–based OSN seismic observatory planning effort, which is now subsumed into the Dynamics of Earth and Ocean Systems (DEOS) planning framework.

Our secondary objective at Site 1243 was to core the lower sediments through the basement interface, extend the core to ~100 m below that interface, and log the cored section. There are only three deep boreholes (>100 m of basement penetration) in the Pacific plate, the largest modern tectonic plate, and one of them is at Site 1243. In 30 yr of deep

[1]Examples of how to reference the whole or part of this volume.
[2]Shipboard Scientific Party addresses.

Ms 203IR-103

ocean drilling and more than 1000 Ocean Drilling Program (ODP)/Deep Sea Drilling Project holes worldwide, there have only been 17 holes with >10 m penetration into the "normal" igneous Pacific plate. Only five holes drilled by ODP (two of these during this leg) have reached this depth of penetration. Furthermore, there are no boreholes off axis in very fast spreading crust. Leg 203 drilling has provided a reference station in normal 12-Ma ocean crust that will constrain geochemical and hydrothermal models of crustal evolution.

A thorough site survey was conducted in the 6 hr prior to making a final decision about siting for the legacy hole. The track lines for the survey are depicted in Figure **F1.** The survey was largely conducted along 3½ east-west legs, each ~5 nmi in length, separated in the north-south direction by 0.5 nmi. The final north-south line (run to the south) replicated a profile collected during Leg 138. The profile on lines 5 and 6 runs in a direction perpendicular to the original profile collected during the site survey for Leg 138. This is shown in Figure **F2.** The two-way traveltime (TWT) through the sediments is quite uniform at ~0.15 s. Based on data collected from the site survey (Mayer et al., 1992) and from Leg 138 itself (Bloomer et al., 1992), we knew that Site 852 was located on a bathymetric high ~4 nmi in width. The data in Figure **F2** are consistent with this; note the increases in depth at each end of the profile. Figure **F3** is the seismic profile between points 8 and 9 and, as noted, replicates the earlier Leg 138 site survey. The profile is essentially identical to the earlier profile, and the sediment is quite uniform along the track.

In order to sharpen the images collected, we elected to migrate the seismic data. Figure **F4** shows the seismic section between points 5 and 6 migrated using a frequency wave-number technique, which is an integral part of the (SIOSEIS) processing package. In this case, we assumed that the sediment velocity was identical to the water velocity of 1500 m/s. We also migrated the data assuming a sediment velocity of 1700 m/s, and the result is shown in Figure **F5.** Although the migration does remove many of the reflection hyperbolae at the seafloor and, thereby, makes the image sharper, we felt there was no significant improvement realized from using 1700 vs. 1500 m/s. One final test was to migrate the data using a finite-difference method from SIOSEIS. The lines 5–6 section is shown in Figure **F6,** after finite difference migration. The added complexity of the finite-difference migration added no discernible improvement to the quality of the processed data. For completeness, we plotted the frequency wave-number migrated sections 8–9 in Figure **F7.**

Based on the site survey that revealed the proximity of a 100-m trough to the west of Site 852 and a broadening of the plateaulike high to the north, we moved the site for Hole 1243A 0.5 nmi to the north of the location originally intended. As shown in the seismic profiles, this places the location for the legacy hole in the central part of the plateau identified by the east-west lines. We felt this was prudent to avoid any possible reflections from the walls of the western trough, in particular, in future seismic data from the observatory.

Operations

At Site 1243, we drilled two holes (Table **T1**) offset from each other on an east-west line by ~600 m, with penetration depths of 224 meters below seafloor (mbsf) (Hole 1243A) and 195 mbsf (Hole 1243B). Basement penetration was 103 and 85 m, respectively. We had originally

F1. Track lines for the Leg 203 site survey, p. 31.

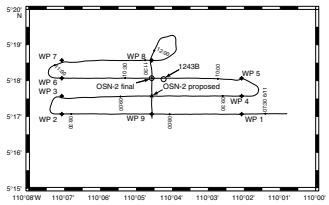

F2. Seismic reflection line between waypoints 5 and 6, p. 32.

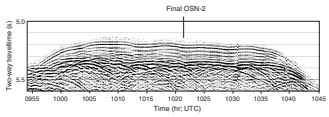

F3. Seismic profile collected between waypoints 8 and 9, p. 33.

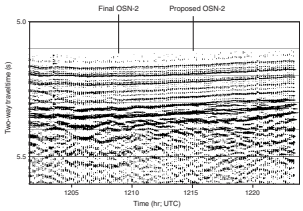

F4. Seismic profile migrated using a frequency-wavenumber technique, p. 34.

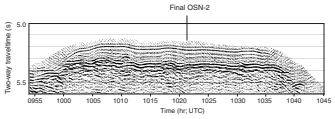

F5. Data migrated at 1700-m/s velocity compared to 1500-m/s velocity, p. 35.

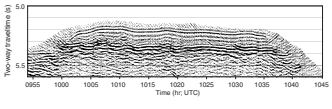

F6. Migration of data along profile 5–6 using at 1500 m/s, p. 36.

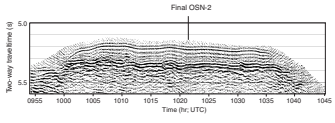

planned to core Hole 1243A following the insertion of 16-in casing into the basement but were forced to change plans when we found it was not possible to insert the casing to full depth. We decided to continue the hole with the 18½-in bit used previously, without coring to the target depth. At this point, the leg had been shortened by 4 days because of a change of port from San Francisco, California, to Victoria, British Columbia, Canada, as a consequence of a possible longshoremen's strike. Whereas the hole in the original plan would have included 20-, 16-, and 10¾-in casing, in the revised operation we ran 10¾-in casing to the bottom of the hole through the upper 20-in casing and cemented it in place. No core was recovered in this hole, and the casing obviated the use of the bulk of the logs. Only a cement bond log and a log to measure hole deviation were run in Hole 1243A. These logs were quite satisfactory, showing fair to excellent bonding in the lower 40 m of the casing and <1° inclinations everywhere in the hole.

Hole 1243B, in a water depth of 3868 m, was located 600 m to the east of Hole 1243A. We washed through the sediments to 102 mbsf and began rotary coring at that depth. In order to maximize recovery, we took half cores throughout the process. At 142 mbsf, we encountered the initial difficulties in Hole 1243B with packing off and continued to encounter problems to the bottom of the hole. As a result of concerns about the loss of the hole and the inability to log, we abandoned drilling after Core 203-1243B-18R. The final core returned to the surface with 5.3 m of fine basalt cuttings. We then logged the hole with the triple combination (triple combo) and Formation MicroScanner (FMS) tools followed by a three-component Well Seismic Tool (WST) vertical seismic profile (VSP) experiment. Data were collected successfully, and in the case of the first two logs, multiple trips to authenticate measurements were possible.

Scientific Results

Because our primary objective during Leg 203 was to drill a cased legacy hole for the subsequent installation of an observatory, coring was limited to a short section of basement rock in Hole 1243B. Little sediment was recovered, but was broadly equivalent to the large quantities of sediment recovered during Leg 138. Basement was cored to a total depth of 195.3 mbsf, including 87.1 m of basement. Seventeen cores were recovered, with an average recovery of 24.8%. This statistic does not include the basalt cuttings recovered in the last core.

The rocks recovered were largely from pillow basalt and comprised both aphyric and sparsely plagioclase and olivine phyric basalt. Based on hand specimens, thin section descriptions, and shipboard geochemical analyses, a total of eight units were identified. Unit 2 was a piece of limestone. There was no evidence of thicker massive lava flows in the material recovered or in the log analyses. Inductively coupled plasma–atomic emission spectroscopy (ICP-AES) analyses indicated that all units are tholeiitic, with the exception of Unit 4, which consists of alkali basalt.

The compressional seismic velocities measured in the samples were high, with a mean of 5.26 km/s. Whereas the triple combo log and vertical seismic tool (VST) velocities were lower, they were consistent with increasing integration of cracks and joints in the increasing wavelengths of the techniques applied.

Paleomagnetic measurements indicate that the basaltic cores recovered from Hole 1243B recorded a stable component of magnetization

F7. Data migrated using the frequency-wavenumber method at 1500 m/s, p. 37.

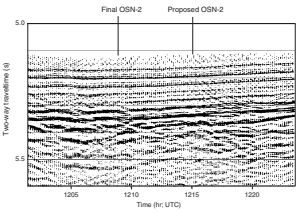

T1. Operations summary, p. 76.

with both normal and possibly reversed inclinations after the removal of the drilling-induced remagnetization. Subsequent shore-based analyses will seek to confirm the presence of both normal and reversed magnetizations.

In Holes 1243A and 1243B, we met the objectives of Leg 203. We completed a cased cemented legacy hole, penetrating nearly 100 m of basement, for the installation of broadband seismometers in a future observatory. We have accomplished this in an area of considerable interest to other disciplines in the Earth and ocean sciences, with the prospect of providing the infrastructure for a future DEOS multidisciplinary observatory. In addition, we were able to recover basalt in the upper oceanic crust in fast-spreading young lithosphere in the Pacific, well in excess of the depth drilled during most previous legs.

BACKGROUND AND OBJECTIVES

Leg 203 was somewhat unusual, although not unique, in its relatively brief length and its exclusive focus on a single site (Site 1243). The primary scientific objective at Site 1243 was to establish a cased legacy hole with a standard reentry cone deep in basement material in a sparsely instrumented region identified by DEOS/OSN and ION. Achieving this objective and subsequently installing a borehole, broadband seismic station, and supporting infrastructure is essential for purposes of global- and regional-scale geophysical observations. It is also anticipated that other geophysical sensors will be installed in the future at and around Site 1243 (e.g., magnetic observatory, etc.).

By conducting drilling, coring, and logging operations in an area of the young fast-spreading Pacific plate, we anticipate gaining significant contributions to the understanding of the formation and evolution of oceanic lithosphere. The age of the lithosphere in this region of the eastern equatorial Pacific is in the range of 10–12 Ma. Most Pacific lithosphere has been produced in a fast-spreading environment. There is, therefore, every reason to believe that the crustal section at the site is quite typical of Pacific oceanic crust. Site 1243 is one of only four Pacific locations where basement coring extends to ≥80 m subbasement penetration. This provides an important petrological, geochemical, and paleomagnetic window into a little-sampled period in Pacific plate formation history.

In addition, Site 1243 is in a particularly interesting location for understanding the interplay between ocean chemistry, productivity, climate, and plate tectonics in a fast-spreading environment. The importance of the region to paleoceanography, oceanography, and climate studies is reinforced by the high productivity of the region and the sensitivity of the rates of sedimentation to both climate and circulation pattern changes associated with tectonic changes.

Hole 1243A was designated OSN-2 after the U.S.-based OSN seismic observatory planning effort was subsumed into the DEOS planning framework. Specific operational requirements for successful installation of the intended broadband seismic station include the following:

1. Reflection seismic survey of the area around the intended location of Site 1243 to confirm the OSN-2 location is positioned on a flat area of sediments and basement (far from obvious faults, grabens, and valleys) suitable for drilling deep into basement

and for installing moorings, junction boxes, and other seafloor sensors as part of future observatory operations.
2. Drilling the hole to a nominal depth of 100-m penetration into basement.
3. Casing the length of the hole.
4. Cementing the bottom of the hole and the annulus surrounding the casing to adequate height above the hole bottom. This is done to ensure good coupling between the casing and the surrounding formation and to prevent the possibility of fluid circulation from below.
5. Ensuring that the deviation of the hole from vertical was within the operational limits of the gimbal system on the broadband seismometer (<5°).
6. Installing a standard ODP reentry cone.

Coring and logging objectives were to obtain an advanced piston core (APC) sediment sample immediately above the sediment/basement interface, to obtain the highest possible recovery from rotary coring into ~100 m of basement, and to carry out a comprehensive suite of downhole logging operations. All coring and logging operations were to be conducted in a manner that would not compromise the integrity of the first objective (i.e., the condition of the cased legacy hole, Hole 1243A).

OPERATIONS

After departing Balboa, Panama, at 1515 hr (CDT) on 3 June 2002, we cleared the Bridge of the Americas then made full speed for Site 852, the intended site of the OSN-2 observatory. Torrential rain in the doldrums was superseded by fine equatorial weather. This provided a pleasant, albeit brief, interlude before we encountered the persistent showers of the ITCZ. The 1921-nmi transit from Panama was completed in 179 hr at an average speed of 10.75 kt. The *JOIDES Resolution* arrived on location at 0015 hr on 11 June. A brief seismic survey was conducted, comprising four parallel east-west lines, each separated by 0.5 nmi in the north-south direction (Fig. **F1**). At the conclusion of the final east-west survey line, a north-south line was run 2 nmi southward to replicate an earlier site survey line. The survey was completed, and the ship was at the intended location of Site 1243 (5°18.0660′N, 110°04.5798′ W) by 0600 hr on 11 June. The hole was relocated ~0.5 nmi north of Site 852 based on the results of the site survey. The new location placed the site farther from a 100-m-deep trough to the west (Fig. **F8**).

F8. Site survey, Holes 1243A and 1243B, p. 38.

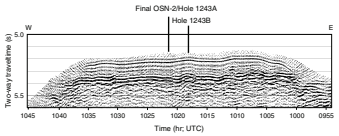

From 0600 hr on 11 June to 0300 hr on 12 June, a jet-in test was conducted in preparation for installing the reentry cone and casing. We stopped the jet-in test at 58 meters below seafloor (mbsf), pulled out of the hole, and cleared the seafloor at 2000 hr on 11 June.

After recovering the drill string, we offset the ship 20 m to the south to 5°18.0541′N, 110°04.5798′W in preparation for spudding Hole 1243A. The reentry cone and four joints (48 m) of 20-in casing were made up, and the reentry cone was lowered through the moonpool at 0800 hr on 12 June. The seafloor was reached at 1600 hr, the reentry cone was installed, and the drill string was released at 1815 hr. Satisfactory placement of the reentry cone was confirmed with the vibration isolated television (VIT) camera.

After tripping back to the surface to remove the running tool, we returned to the hole with an 18½-in bit. Reentry was achieved at 0943 hr

on 13 June. It was a textbook reentry, with an elapsed time of 8 min. We then drilled down below the 20-in casing, reaching the sediment/basement contact at 121 mbsf. Basement drilled well, with penetration rates ranging from 0.8 to 2.0 m/hr. Drilling concluded at 0745 hr on 14 June at a depth of 134 mbsf. We then made a wiper trip and prepared to install the 16-in casing.

At 1630 hr on 14 June, the crew commenced rigging up the casing tools to run the 16-in casing into basement. The target depth for the 16-in casing was 126 mbsf (4008 meters below rig floor [mbrf]), in order to isolate the 73 m of sediment and the top 5 m of basement as we drilled deeper. Reentry 2 occurred at 0440 hr on 15 June. The driller washed down through the 20-in casing and sediment and took weight at the basement contact at 121 mbsf (4003 mbrf). It took ~1 hr to work the 16-in-casing cement shoe through the basement contact. On repeated attempts to pass through the interval from 120 to 123 mbsf, the casing (17-in outside diameter) became stuck, and overpulls of up to 40 klb were required to free it, as it became wedged in the 18½-in basement open hole.

On the last attempt to land the casing in the reentry cone, it became stuck firmly and took 100 klb of overpull to free it. In light of these difficulties, we decided to pull out of the hole. On recovery, the cement shoe on the 16-in casing was found to have been damaged severely in attempting to get the casing to bottom. The 10 joints of casing were laid down by 1900 hr on 15 June.

The operations plan was then revised to complete Hole 1243A without coring, as a cased hole with only 20- and 10¾-in casing. The target depth for the 10¾-in casing was 216 mbsf. Following completion of Hole 1243A, we planned to drill, RCB core, and log a second hole to 200 mbsf to obtain cores across the sediment/basement interface and into the basement. Time estimates showed that this plan could be achieved within the available time, despite the change in location of the end of Leg 203 port call. (On 13 June, we were advised that the port call had been changed from San Francisco, California, to Victoria, British Columbia, Canada, in anticipation of a longshoremen's strike in San Francisco in early July. This change added almost 4 more days to the transit from Site 1243 to port.)

The third reentry of Hole 1243A took place at 0405 hr on 16 June. We washed down to 134 mbsf and then drilled ahead in basement to a depth of 224 mbsf at an average rate of 3 m/hr. At 180–184 mbsf, the drill string packed off and required 60 klb overpull to free it, but otherwise, no problems were encountered.

After cleaning the hole and displacing it with 250 bbl of sepiolite, we then prepared to set the 10¾-in casing. Reentry 4 was achieved with the casing at 2050 hr on 18 June. The casing landed in the hole at 2345 hr, and cementing was completed by 0200 hr on 19 June. This required 100 bbl of cement and is one of the largest cement jobs done by ODP to date. We pulled out of the hole, and the running tool was back on the rig floor at 1000 hr on 19 June. We then made a cleanout trip in preparation for the future installation of the OSN-2 seismometer. Reentry 5 was achieved at 2105 hr on 19 June, and after circulating the casing clean with seawater, we pulled out of the hole, clearing the seafloor at 0025 hr on 20 June. The depth of the hole, measured to the cement, is 199 mbsf (Fig. F9).

The ship was offset 600 m to the east with the drill pipe and VIT camera down, and Hole 1243B was spudded at 0245 hr on 20 June (5°18.0543′N, 110°4.2544′W) at a water depth of 3868 m. We washed

F9. Schematic representation, Hole 1243A, p. 39.

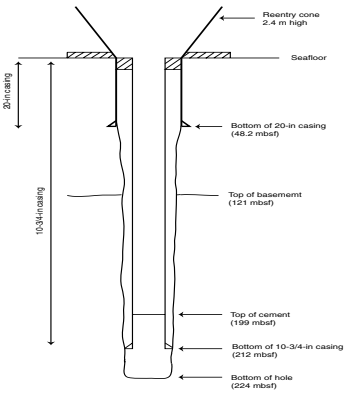

down through the sediment section to 102 mbsf, then pulled the center bit, and commenced RCB coring. To improve recovery, we took half cores (4.5 m). At a depth of 142 mbsf, the hole packed off, requiring 40 klb of overpull to free the bottom-hole assembly. We continued to have problems with packing off, and core recovery dropped. After repeated hole problems and poor recovery, the decision was made after Core 203-1243B-18R to abandon further attempts to core deeper. The final core returned to the surface with 5.3 m of fine black basalt cuttings.

After abandoning further attempts to core deeper in Hole 1243B because of deteriorating hole conditions, we prepared the hole for logging. Triple combo and FMS-sonic logs were run in Hole 1243B, followed by a WST log in the basement section of the hole. Poor hole conditions prevented successful running of the WST in the sediment section. Eight WST receiver stations were run from bottom to top of the basement section. We then dropped a free-fall funnel in Hole 1243B and offset the ship back to Hole 1243A, where we ran both inclination and cement bond logs in order to determine the characteristics of the cased hole in anticipation of future installation of the seismometer. Because the intervals to be logged at both Holes 1243B and 1243A were short, we had time to make more than one traverse with each suite of logging tools (except the WST and inclinometer), in order to verify that we were getting consistent good quality data.

After completing the cement bond log in Hole 1243A, we snagged the first beacon dropped at Site 1243, which had ceased operating, with a grapple on the VIT frame. The VIT frame and beacon were back on deck at 0915 hr on 25 June, and we began the final trip out of the hole. The second (active) beacon was retrieved at 1300 hr on 25 June, and we completed tripping pipe at 1330 hr, bringing operations at Site 1243 to a conclusion. The *JOIDES Resolution* got under way for Victoria at 1530 hr on 25 June, arriving there at 0700 hr on 7 July.

SEDIMENTOLOGY

No sediments were recovered from Hole 1243A, and few were recovered from Hole 1243B. Core 203-1243B-1R contains a slurry of mud with a few coherent pieces of nannofossil ooze that had caved into the hole. The pieces are of lithologies and colors like the oozes recovered during Leg 138. They are composed dominantly of coccoliths, with zero to a few percent planktonic foraminifers, discoasters, radiolarians, FeO globules, and glass.

Three intervals within the recovered basalt contain sediment. Section 203-1243B-2R-1 [Piece 6] is a centimeter-sized firm lump of nannofossil ooze that must have caved into the borehole. Section 203-1243B-2R-1 [Piece 9] is an oblate-shaped piece of white limestone with brown palagonite grains and is the main subject of this report. One end of Section 203-1243B-10R-2 [Piece 8] has a thin selvage of pinkish gray limestone with palagonite grains, black specks, and apparent relics of foraminifers adhering to the glassy rind of the basalt similar to that of Core 2R, which is described next.

The white limestone in interval 203-1243B-2R-1 [Piece 9, 45–47 cm] is in proper stratigraphic position, as some of the basalt pieces recovered above and below it are of sufficient diameter to have blocked any vertical shuffling. The 1-m interval from 3984 to 3985 m on borehole logs (1 or 2 m below top of basement) has distinctly lower density and porosity and very likely pinpoints the position of the limestone. This

rock is a palagonite- and peloid-bearing foraminiferal limestone. By texture and composition, it is a sparse foraminiferal pelbiomicrite; by its texture at time of deposition, it is a wackestone (Fig. **F10**). Small dots of a black mineral, up to 5 mm across (probably manganese oxide), mark the white surface on which small circles of finely crystalline calcite outline microfossils. Some flakes of brown palagonite, ~1 mm thick and up to 8 mm wide, are seen on the surface, and additional volcanogenic grains are seen in thin section. The prismatic shape of abundant pores in the rock indicates that authigenic anhydrite had been present in early diagenesis. Presumably, the limestone formed by the diagenesis of peloidal foraminiferal nannofossil ooze that had accumulated in a depression on a basalt surface, perhaps between pillows, and was covered by a later flow.

Calcite is the predominant mineral. The limestone's main component is micrite, based on examination of two thin sections and 650 points counted on one of them, excluding points that fell on voids and plucked areas. Most micrite is matrix between the foraminifers and peloids (44% of the slide), and additional micrite constitutes peloids (15%) and fills some foraminifer tests (7%). Some of the micrite is featureless, but scattered through parts of it are round darker areas or clots ~20 µm across (diameters are reported as observed, not as reduced by 87% to relate random slices to average sphere volumes). Their edges are fuzzy, and light does pass through them; they are dark but not opaque. The micrite is very finely crystalline to aphanocrystalline, with crystal diameters typically 1–2 µm. The ragged feather edge of a thin section, ground as a wedge from 30 to 0 µm, has a few coccoliths among the calcite crystals in the mounting medium. Those nannofossils, and several seen on an acetate peel from the limestone surface, are more numerous than would be expected from laboratory contamination. As nannofossils are the dominant component of the sediment above basement, the micrite of this limestone is thought to have crystallized from nannofossil ooze.

Peloids in this rock are rounded to somewhat irregular masses with a darker border and scattered fuzzy-edged darker clots, as described above, and are held to indicate origin as fecal pellets in modern and ancient peloids. They appear to be bimodal in texture, with modes in medium sand size at ~0.3–0.5 mm and in coarse silt size at ~0.04–0.06 mm. Points were not counted on the second thin section, but by visual estimation, it contains more foraminifers and fewer peloids (ratio of ~3:2) than the approximately equal proportions recorded here.

Walls of foraminifer tests account for 15% of the area of the slide. Many tests appear whole, whereas others are obviously broken. In addition, individual and multiple parallel grains of prismatic calcite within the matrix have lengths similar to the thicknesses of foraminiferal walls and, hence, are assigned as such. Thus, foraminiferal calcite is ~17% of the slide. Virtually all foraminifer walls have the shape of arcs, and many that are sectioned show interiors with globular shapes. Pores may be filled with opaque material, a situation that seems more common in those with globigerinoid-type wall structure. A few biserial, trochoid, and biconvex foraminifers may be present, according to test outlines and the patterns of calcite crystals.

Sparry calcite and straight-edged (commonly square to rectangular) pores fill foraminifer interiors lacking micrite. Spar acts as a patchy cement, with the distinctive pores also present in some areas between the allochemical grains (foraminifers and peloids), in particular between silt-sized peloids. Spar and pores also fill irregular veins and a burrow,

F10. Limestone cut surface photograph and thin section photomicrograph, p. 40.

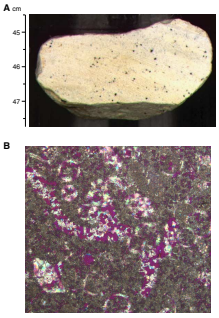

and some square voids are randomly distributed in micrite. About 11% of the rock is a mosaic of blocky calcite spar (in crystal sizes mainly <0.15 mm) but, in one instance, 0.25 mm × 0.25 mm. There is little evidence that the spar grew as syntaxial overgrowths on the foraminifers, but there is no doubt that the calcite grew against the earlier mineral now represented by pores. The rectangular pores were recorded on the traverses of points but not included in calculating components of the solid rock. If all were recalculated, the now-absent mineral would have been 6% of the volume of the limestone. The larger of the absent prisms were ~0.20 mm long and 0.06 mm across. Almost certainly, the missing mineral was anhydrite, but no anhydrite was detected by X-ray diffraction (XRD). The paragenesis was growth of euhedral anhydrite in pore spaces, growth of anhedral calcite against anhydrite, and dissolution of anhydrite leaving the distinctive moldic porosity.

The limestone's surface is speckled with black. Typically, when black minerals like these that appear on limestone are analyzed, they are found to be manganese oxides. In thin section, the opaque areas have different forms but provide few clues for their shipboard identification. The most abundant of the opaque grains are 10–25 µm in size and are present in clusters. They display straight sides and multiple sharp angular corners that must represent crystal faces and angles of an aggregate of opaque grains. They lack the bright red color of thin edges of hematite in conoscopic light; these are brownish black to reddish brown. Nor do they have the brassy luster of pyrite in reflected light; these are dull black. The three most common manganese oxide minerals in the marine environment (e.g., in ferromanganese nodules and crusts and in micronodules in pelagic sediments) are vernadite followed by birnessite and todorokite. Only todorokite is represented in the MacDiff XRD database; its lines are not present on the diffractogram. Nor are there any lines for the principal d-spacings given in Burns and Burns (1979) and Roberts et al. (1990) for vernadite (2.39 main; 4.80 and 2.39) and birnessite (7.27 main; 3.56, 2.44, and 1.41). Thus, the actual mineralogy of these opaque minerals remains unidentified, even though they are probably manganese oxides.

The largest totally opaque areas are as wide as 0.25 mm in one section and 0.90 mm in the second. Their edges seem more ragged than edges of the smaller masses mentioned above, but in conoscopic and reflected light their appearance is similar; probably, they are dense accumulations of that mineral. By their size, distribution, and distance apart, these opaque masses represent the black specks seen on the sample.

A very minor constituent of the slide is a cluster of brown, platy, nearly opaque unidentified grains that are ~30 µm long × 7 µm wide. Seen, but not encountered by the cross hairs during the traverses, are a few pieces of fish debris.

Glass with plagioclase microlites was not counted because the traverses avoided the plucked areas where it is present. Laths of plagioclase (to 0.3 mm long) are sheathed in glass, which has been partly replaced by swelling clay and calcite. Plagioclase and smectite are confirmed by small peaks on the X-ray diffractogram and by grains of the feldspar and clumps of the clay in the insoluble residue. The residue also has some glass grains (mainly heavily etched), some spicules, and a mass of zeolites that grew in what may have been a radiolarian test.

PETROLOGY AND GEOCHEMISTRY

Basement material from Hole 1243B was first recovered in Core 203-1243B-2R at 108.6 mbsf (curated depth). Basement was drilled and cored to a total depth of 195.3 mbsf, which represents 87.1 m of basement section. Recovery averaged 25%, ranging from 1.6% in Core 203-1243B-16R to 63.7% in Core 7R (this recovery statistic does not include 5.3 m of drilling breccia/cuttings recovered in the deepest core) (Fig. F11). On the basis of hand specimens, thin section descriptions, and shipboard geochemical analyses (see also "Core Descriptions," p. 4, in the "Explanatory Notes" chapter), eight basement units were defined (Fig. F11; Table T2). Units 1, 3, 4, 5, 6, 7, and 8 are volcanic basaltic units. Units 1, 3, and 7 are aphyric basalt. Units 4, 5, and 6 are sparsely plagioclase and olivine phyric basalt. Unit 8 consists of moderately plagioclase and olivine phyric basalt. Unit 2 is formed by a piece of limestone (see also "Sedimentology," p. 7). All basement basaltic units are interpreted as pillow lavas based on the presence of glassy margins and associated vesicular zones. No evidence of thicker massive lava flows was found in the cores. This interpretation of the environment of eruption is further confirmed by downhole measurements in Hole 1243B (see "Downhole Measurements," p. 22). ICP-AES analyses conducted on board indicate that all units are tholeiitic except Unit 4, which consists of alkali basalt (see also "Geochemistry," p. 13). The basement units range in thickness from 0.065 m (Unit 2) to 11.175 m (Unit 3) (Table T2). At the bottom of Hole 1243B, 5.3 m of drilling breccia was recovered. This consists of broken angular fragments of pillow basalt (Core 203-1243B-19B).

F11. Lithology summary, Hole 1243B, p. 41.

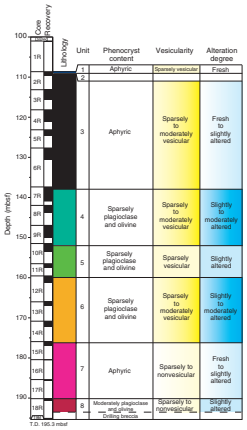

T2. Basement unit characteristics, p. 77.

T3. Mineral assemblage and proportions, p. 78.

Macroscopic and Petrographic Description

This section describes the different lithologies and petrographic primary features of the basement sequence in Hole 1243B as observed in hand specimens and thin sections. Detailed descriptions of each core section can be found in "Site 1243 Visual Core Descriptions." Detailed description of the thin section can be found in "Site 1243 Thin Sections." The main features of thin sections are reported in Table T3. Further information on alteration assemblages, veins, and vesicle fillings can be found in "Alteration," p. 15.

Basalt recovered from Hole 1243B is aphyric to sparsely plagioclase and olivine phyric (Fig. F11). Textures in the groundmass are generally aphanitic to fine grained. The degree of alteration, overall, is low (see Fig. F11) (see "Alteration," p. 15). Glassy rinds are present throughout the recovered basement section, and most of the glass is slightly altered, though some samples of fresh glass were found. Textural gradations were observed along pillow margins, with coarser-grained material present further from the glassy rind. Vesicularity ranges from nonvesicular in Units 7 and 8 up to sparsely vesicular with some moderately vesicular pieces in Units 3, 4, and 6 (Fig. F11). Rounded to elongate vesicles are present throughout the units, ranging in size from <1-mm- to 2-cm-long pipe vesicles. Twenty-three shipboard samples were taken for thin section observations from both pillow rims and pillow interiors, including some samples selected for alteration features. Microphenocrysts of plagioclase and olivine are mostly fresh and euhedral to subhedral. Quenched plagioclase crystals are evidenced in thin sections by

skeletal and swallow-tail structures. Opaque minerals in the groundmass include euhedral magnetite and needle-shaped ilmenite.

Unit 1

Basement Unit 1 is composed of aphyric basalt (Fig. F12A). This unit consists of pillow lavas, some showing glassy margins. The groundmass is holocrystalline and composed of euhedral lath-shaped plagioclase ($An_{48–50}$), subhedral, prismatic augite clinopyroxene, interstitial glass, and opaque minerals (Fig. F12B, F12C). Opaque minerals are euhedral to subhedral cubic magnetite crystals and rare elongate needles of ilmenite. Blotches of primary sulfides are also present. Unit 1 is sparsely vesicular, with randomly distributed empty (60%) and filled (40%) round vesicles.

F12. Main macroscopic and microscopic characteristics, Unit 1, p. 42.

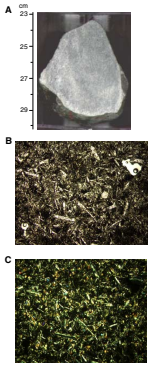

Unit 2

Unit 2 is a palagonite- and peloid-bearing foraminiferal limestone with manganese oxide granules up to 5 mm across and randomly distributed throughout the rock. The texture is sparse foraminiferal pelbiomicrite, formerly wackestone (see "Sedimentology," p. 7).

Unit 3

Unit 3 comprises aphyric pillow basalt very similar to that of Unit 1 (Fig. F13A). The groundmass is hypocrystalline and consists of plagioclase, clinopyroxene, glass, and opaque minerals (Fig. F13B, F13C). The plagioclase crystals are euhedral to subhedral with tabular, lath, swallow-tail, needlelike, and radial shapes/forms. The clinopyroxene crystals (augite) are generally subhedral to anhedral, ranging in size from 0.1 to 0.5 mm. Magnetite is the dominant opaque mineral, identified by its euhedral cubic form. Unit 3 is sparsely to moderately vesicular with randomly distributed filled and empty vesicles.

F13. Main macroscopic and microscopic characteristics, Unit 3, p. 43.

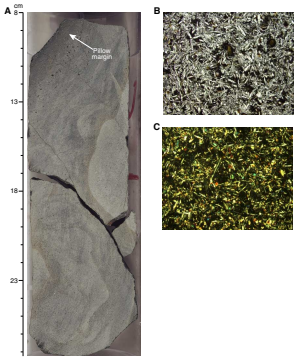

Unit 4

Unit 4 comprises pillowed sparsely plagioclase and olivine phyric basalt (Fig. F14A). The boundary between Units 3 and 4 was not clearly observed but was inferred from the appearance of microphenocrysts in Unit 4. Plagioclase microphenocrysts ($An_{48–50}$) are euhedral and tabular to lath shaped, range in size from 0.4 to 2 mm, and are associated with minor amounts of euhedral olivine microphenocrysts (Fig. F14B, F14C). The groundmass is aphanitic to fine grained with a hypocrystalline texture and consists of plagioclase, clinopyroxene, olivine, glass, and opaque minerals. The presence of olivine in the groundmass denotes the alkaline affinity of the basalt (see also "Geochemistry," p. 13). Two different types of clinopyroxene were identified in thin section: augite, clinopyroxene, and scarce, but easily distinguishable, brown Ti-enriched augite (Fig. F14D). Some minor amounts of spinel (<1%) were identified in thin section. Unit 4 is sparsely to moderately vesicular with rounded to elongate, randomly distributed vesicles ranging up to 2 mm in length.

F14. Main macroscopic and microscopic characteristics, Unit 4, p. 44.

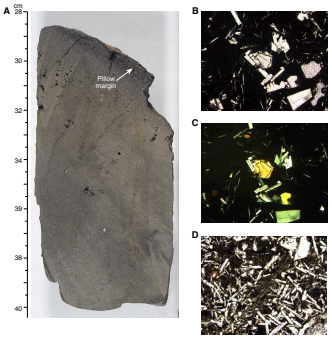

Unit 5

Unit 5 comprises pillowed sparsely plagioclase and olivine phyric basalt (Fig. F15A). The boundary between Units 4 and 5 was inferred from the absence of olivine in the groundmass, brown clinopyroxene, and geochemical differences (see "Geochemistry," p. 13). Microphenocrysts of plagioclase and olivine are euhedral to subhedral (Fig. F15B, F15C). The groundmass in Unit 5 is fine-grained hypocrystalline comprising plagioclase, augite clinopyroxene, glass, and opaque minerals (Fig. F15D). Unit 5 is sparsely vesicular, having rounded randomly distributed filled and empty vesicles (Fig. F15E).

F15. Main macroscopic and microscopic characteristics, Unit 5, p. 45.

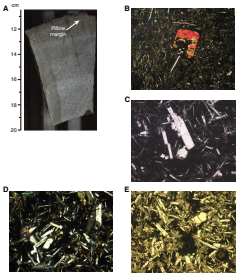

Unit 6

Unit 6 comprises pillowed sparsely plagioclase and olivine phyric basalt (Fig. F16A). The boundary between Units 5 and 6 was inferred from the presence in groundmass of brown clinopyroxene (likely Ti-enriched augite) (Fig. F16B, F16C). Tabular to lath-shaped plagioclase and olivine microphenocrysts are euhedral to subhedral, varying in size from 0.6 to 2 mm and from 0.5 to 1 mm, respectively (Fig. F16D). The groundmass is aphanitic to fine-grained hypocrystalline and consists of plagioclase, clinopyroxene, glass, magnetite, and ilmenite (Fig. F16A). Vesicularity ranges from sparse to moderate. Rounded empty and filled vesicles are randomly distributed through the unit (Fig. F16A).

F16. Main macroscopic and microscopic characteristics, Unit 6, p. 46.

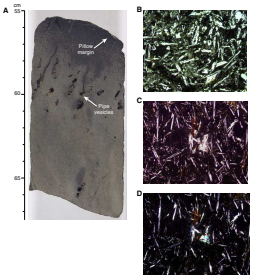

Unit 7

Unit 7 comprises pillowed aphyric basalt (Fig. F17A). The boundary between Units 6 and 7 was inferred from the disappearance of microphenocrysts in Unit 7. The groundmass is holocrystalline and composed of plagioclase, augite clinopyroxene, glass, and opaque minerals (mainly magnetite) (Fig. F17B, F17C). Several plagioclase aggregates were observed through the unit. Vesicularity ranges from nonvesicular to sparsely vesicular; filled and empty vesicles are <0.5 mm, equant, and randomly distributed (Fig. F17A).

F17. Main macroscopic and microscopic characteristics, Unit 7, p. 47.

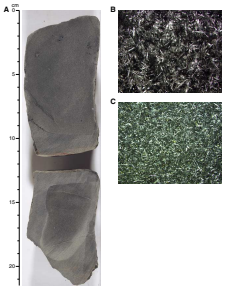

Unit 8

Unit 8 comprises pillowed moderately plagioclase and olivine phyric basalt (Fig. F18A). Skeletal plagioclase microphenocrysts up to 0.7 mm in size are present, sometimes aggregated. Olivine microphenocrysts are euhedral, fresh, and have an average size of 0.3 mm (Fig. F18B, F18C). The groundmass texture is aphanitic, hypohyalline, and variolitic (Fig. F18D). The groundmass is composed of plagioclase, augite clinopyroxene, glass, and opaque minerals. Textural gradation is well observed in Section 203-1243B-18R-1 [Pieces 4, 5, and 7] from a glassy rim to a vesicular interior with vesicles ranging up to 1 mm in diameter. Vesicularity ranges from nonvesicular to sparsely vesicular with rounded empty or filled vesicles.

F18. Main macroscopic and microscopic characteristics, Unit 8, p. 48.

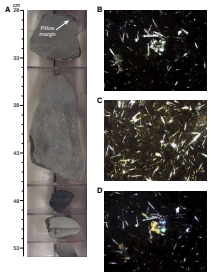

Relations between Recovery Rate and Pillow Texture in Hole 1243B

The pillow lavas of the Hole 1243B basement sequence show the following characteristic zones, from their upper outer part to their interior:

1. Black to dark gray glassy margin, commonly <5 mm thick;
2. Dark gray to brownish gray variolitic zone, normally 5–20 mm thick;
3. Gray to pale-brown vesicular zone, usually 20–40 mm thick;
4. Brown to dark-brown transitional zone, up to 100 mm thick; and
5. Dark-green crystalline interior.

The lower part of the pillow displays identical features, but the thickness of each zone is approximately one-half that of the upper part. Glassy margins may be observed from the tops of pillows (upper glass zone [UGZ]), bottoms (lower glass zone [LGZ]), or both (upper and lower glass zone [ULGZ]). In Hole 1243B, basement sequence glassy margins were observed in 46 rock pieces (12.8% of basement recovered). Among those 46 samples, only 11 pieces are oriented. Nine pieces (19.6%) and two pieces (4.3%) are from UGZ and LGZ, respectively. Rock pieces with ULGZ were not recovered in Hole 1243B nor was interpillow material recovered. More glassy pillow tops than pillow bottoms were recovered, which can be explained by:

1. Pillow lava formation. Glassy margins are produced by quenching when hot magma contacts cold seawater. At the bottom of pillows, the chilling effect can be reduced by preexisting pillows.
2. Drilling physics. The pillows contain many joints as a result of their cooling history and break easily into drill core pieces before drilled cores are pushed into the core barrel. However, coring might be more effective in the upper part of the pillow because the glass zone is thicker.

The relationship between core recovery and pillow texture is discussed further in the "Appendix," p. 29.

Geochemistry

Major and trace element abundances were determined by ICP-AES (see "Core Descriptions," p. 4, in the "Explanatory Notes" chapter) for nine samples from Hole 1243B. The selected samples were taken from pillow interiors, and the results are reported in Table T4. At least one sample from each basement unit was analyzed, except Unit 6, which was not sampled for ICP-AES.

Basement Units 1, 3, 5, 7, and 8 are tholeiitic basalt, and Unit 4 is composed of alkali basalt, following chemical (alkali silica diagram) and petrographic classifications (Fig. F19). Al_2O_3, Ti/Zr, and Ba/Sr are reported vs. depth in Figure F20. No systematic variations were observed downhole except for the distinctive characteristics of alkali basalt in Unit 4. Units 1, 3, 5, and 8 display very similar geochemical characteristics, whereas Unit 7 shows a slightly lower content of Al_2O_3 and lower Ti/Zr ratios.

Within the tholeiitic units, the samples are almost unaltered, as evidenced by their low loss on ignition (LOI) values (LOI = <0.90 wt%) (see Table T4) (see "Alteration," p. 15), and this confirms the petrographic observations. The samples exhibit moderate compositional variation within narrow ranges of SiO_2 (49.99–51.64 wt%), MgO (5.74–7.29 wt%), or TiO_2 (1.43–2.12 wt%) (Table T4). Mg# (Mg# = Mg/[Mg+Fe^{2+}] × 100, with Fe^{2+} estimated as 85% of total iron) for this group of units, ranges from 50.2 to 65.7 (Fig. F21; Table T4). The samples from Units 1 and 3

T4. Element concentrations, p. 79.

F19. Igneous rock composition on the $Na_2O + K_2O$ vs. SiO_2, Hole 1243B, p. 49.

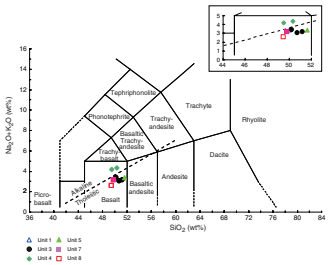

F20. Downhole variations of Al_2O_3 and trace element ratios, p. 50.

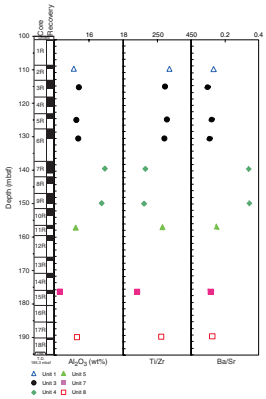

F21. Al_2O_3 and Ti/Zr ratios vs. Mg#, p. 51.

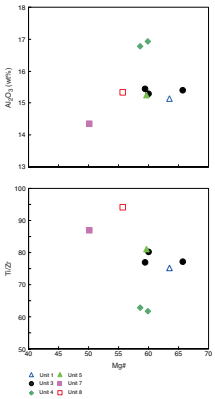

display the most primitive compositions (Mg# = 59.4 – 65.6). Variation diagrams of Al_2O_3 vs. Mg# show a trend consistent with slight variations in the proportions of fractionated phases (i.e, olivine, plagioclase, and clinopyroxene) between the different units (Fig. **F21**). Units 1, 3, and 5 display very homogeneous characteristics; Units 7 and 8 are slightly more differentiated (Mg# = 55.6–50.1). Massive fractionation of plagioclase, and subsequently magnetite, is consistent with the lower Al_2O_3 content of Unit 7. The trace element ratio Ti/Zr is plotted against Zr/Y and Ba/Sr ratios in Figure **F22.** Ti/Zr ratios are slightly higher in Units 7 and 8 as are Zr/Y ratios, which is consistent with their more fractionated characteristics. The relatively unaltered nature of these samples allows us to consider Ba and Sr concentrations as representing the original magmatic elemental composition. We observe a constant Ba/Sr ratio for these units (Fig. **F22**). In a primitive mantle–normalized trace element diagram (Fig. **F23**), samples from Units 1, 3, 5, 7, and 8 have generally subparallel patterns, with $(Zr/Ti)_N$ and $(Zr/Y)_N$ ranging from 1.2 to 1.9 and from 1.1 to 2.2, respectively.

The alkali basalt from Unit 4 shows distinctive geochemical features. Because the LOI contents of these samples are higher (up to 2.7 wt%), we expected their alkali abundances to be affected by postmagmatic alteration. However, abundances in Y, Nb, Ba, and Sr are very similar in the altered (LOI = 2.7 wt%) and least-altered (LOI = 1.4 wt%) samples from Unit 4, indicating that secondary processes have not affected these elements (Figs. **F20, F21, F22;** Table **T4**). On this basis, we tentatively conclude that the high TiO_2 (2.11–2.12 wt%), along with Ba, Zr, and Nb contents, are original magmatic features of Unit 4 basalt. Compared to the tholeiitic basalt of Units 1, 3, 5, 7, and 8, basalt from Unit 4 has higher Ti/Zr, Ba/Sr, and Zr/Y ratios (Fig. **F22**). In a primitive mantle–normalized incompatible element diagram, they show an enriched pattern with $(Zr/Ti)_N$ ranging from 1.8 to 1.9 and $(Zr/Y)_N$ from 2.2 to 2.3, similar (at least for the shipboard incompatible trace element data) to those of alkali basalt worldwide (Fig. **F23**). The alkaline signature of Unit 4 is consistent with the fractionation of Ti-enriched clinopyroxenes, which appear to join olivine rather than plagioclase as a fractionation phase.

The shipboard petrographic and geochemical data led to the following preliminary conclusions, which will require careful testing as additional geochemical and isotopic data become available. The petrographic and geochemical characteristics of Units 1, 3, 5, 7, and 8 indicate relatively unevolved lavas with minimal differentiation at the crustal level. These tholeiitic units likely derived from a single mid-ocean-ridge basalt (MORB)-type mantle source. The partial melting event that led to the formation of these magmas probably took place at a shallow level with moderate partial-melting degree (>5%). The distinctive geochemically enriched signature of Unit 4 does not match with the identical moderate–high degree of partial melting of a depleted MORB-type mantle source (the terms "enriched" and "depleted" are used to indicate relative enrichment/depletion in the highly incompatible element abundances). Such enrichment in trace elements can be related to (1) the low partial-melting degree of a depleted MORB-type mantle source—a source similar to the one from which the tholeiitic basalt originated or (2) the partial melting of a distinctive (enriched) mantle source such as metasomatized upper mantle. No systematic spatial and temporal relationships were determined for the Hole 1243B basement section, and the petrogenetic conditions in which these

F22. Abundance ratios of Zr/Y and Ba/Sr vs. Ti /Zr, p. 52.

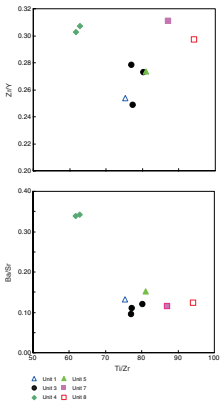

F23. Incompatible trace element pattern for tholeiitic and alkalic basalt, p. 53.

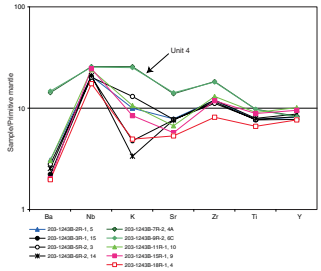

tholeiitic and alkaline magmas formed remain tentative, pending further shore-based studies.

Alteration

Eight basaltic basement units were identified in Hole 1243B. Most basaltic rocks have undergone slight secondary alteration. Alteration mineralogy was defined in rocks from Hole 1243B by color, habit, and hardness in hand specimens, by optical properties in thin sections, and by analogy with well-studied minerals identified during previous legs. Because of the low degree of alteration, no XRD measurements were conducted on samples from Hole 1243B, and the identification of secondary minerals in Hole 1243B, therefore, remains tentative pending further shore-based studies.

The effects of alteration in rocks from Hole 1243B are defined within the basaltic units in terms of alteration assemblages, vein and vesicle filling when present, and alteration chemistry.

Alteration Assemblages

In this section, we describe the alteration paragenesis for each basaltic unit, as recorded during core description and following thin section examination. We also include the vein and vesicle filling as recorded during hand-specimen observation. Additional data are available in the thin section descriptions and the alteration and vein logs (see the "Core Descriptions" contents list).

Units 1, 3, and 7

All the aphyric basalt recovered in Unit 1 is generally fresh, but the extent of alteration slightly increases toward vesicles and fine-grained margins. Units 3 and 7 are slightly altered. The alteration assemblages and vein and vesicle fillings are identical for these three units, and typical assemblages are presented in Figure F24. Color throughout the units varies from medium gray to medium light gray to light gray (N5–N6–N7) in the interior of lobes to light brown (5YR 5/6), dark yellowish orange (10YR 6/6), brownish brown (10YR 5/4), moderate brown (5YR 4/4), and moderate reddish brown (10YR 4/6) at altered fine-grained lobe margins, around veins, and next to vesicles. In very few sections, a greenish black (5G 2/1) was recorded. As the colors show, Fe oxyhydroxide formation is pervasive through the unit and is most prominent at the margins. Most of the groundmass is fresh or slightly altered to brown clay mineral (nontronite) and Fe oxyhydroxide. Glass is unaltered to moderately replaced by palagonite. In Unit 1, vesicles are sparse, and some are filled and/or lined with Ca carbonate (calcite) and zeolite. One vein was observed to be filled by small amounts of greenish clay minerals and Ca carbonate (calcite). Unit 3 is sparsely veined. Veins are 1–2 mm wide and are mostly filled with Ca carbonate (calcite), brown clay (nontronite), zeolite (analcite), and Fe oxyhydroxide (Fig. F24). Unit 3 is sparsely to moderately vesicular. Some vesicles are filled with and/or lined by Ca carbonate (calcite), brown clay (nontronite), and zeolite (analcite). In one section, vesicles are filled with green clay (saponite) (Fig. F24). Unit 7 is sparsely vesicular to nonvesicular, some vesicles are filled with and/or lined by Ca carbonates (calcite), brown clay (nontronite), and Fe oxyhydroxide.

F24. Main alteration features in Units 1, 3, and 7, p. 54.

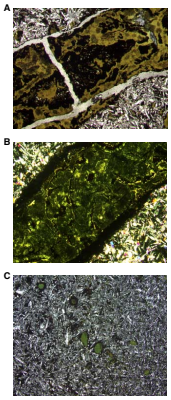

Units 4, 5, and 6

Units 4, 5, and 6 consist of sparsely plagioclase and olivine phyric basalt. The degree of alteration is slight to moderate through Units 4 and 6, although it should be noted that the extent of alteration rarely exceeds 10% replacement, with a maximum of 15%. Unit 5 is slightly altered. The alteration assemblages and vein and vesicle fillings are identical for these three units, and typical features are presented in Figure F25. Color varies from medium gray to medium light gray to light gray (N5–N6–N7) to dark yellowish orange (10YR 6/6), moderate yellow brown (10YR 5/4), and pale yellowish brown (10YR 6/2). The maximum degree of alteration is found in Section 203-1243B-7R-2 [Pieces 1A–1C], which shows a light olive-gray color (5Y 5/2). Olivine microphenocrysts are partly replaced by reddish brown Fe oxyhydroxide (iddingsite). Plagioclase microphenocrysts are slightly altered to sericite. Part of the groundmass is replaced by brown clay (nontronite) and Fe oxyhydroxide. Glass is replaced by palagonite in the margins (Fig. F25). Veins are sparse (0.1–1 mm wide) and filled with Ca carbonate (calcite), brown clay (nontronite), and Fe oxyhydroxide (Fig. F25). One wider vein (4 mm) is found in Section 203-1243B-7R-1 [Piece 11] and is filled with the same assemblage. Some vesicles are filled with and/or lined by Ca carbonate (calcite), zeolite (analcite and phillipsite), brown clay (nontronite), and Fe oxyhydroxide.

F25. Main alteration feature in Units 4, 5, and 6, p. 55.

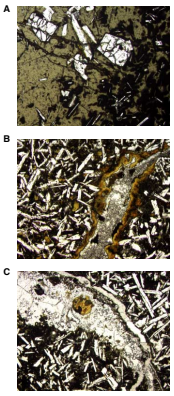

Unit 8

Unit 8 consists of slightly altered moderately plagioclase and olivine phyric basalt. Color varies within the unit from medium light gray (N6) to dark gray (N3). The altered part is dark yellowish orange in color (10YR 6/6) because of the Fe oxyhydroxide formation. Olivine is partly replaced by reddish brown Fe oxyhydroxide (iddingsite). Some plagioclase microphenocrysts are slightly altered to sericite. Groundmass is altered to brown clay and Fe oxyhydroxide. Glass is replaced by palagonite. Unit 8 is sparsely vesicular to nonvesicular. Some vesicles are filled with and/or lined by zeolite.

Alteration Chemistry

All shipboard samples analyzed during Leg 203, except one (Sample 203-1243B-9R-2, 135–138 cm), have LOI values <2 wt%. LOI is a proxy for the degree of alteration and is reported vs. depth on Figure F26. LOI values vary downhole from 0.1 to 2.7 wt%, with an increase in Unit 4. This trend confirms macroscopic and petrographic observations of the samples, with a very low degree of alteration for the all basement section recovered. Mobile elements such as K, Sr, or Ba show the same geochemical characteristics as immobile elements such as Ti, Zr, or Y, indicating very low to no chemical mobility related to alteration (see Fig. F20) (see "Geochemistry," p. 13).

Overall, the basement sampled in Hole 1243B is fresh to slightly altered. The alteration paragenesis is clearly dominated by Fe oxyhydroxide, brown clay (nontronite), Ca carbonate, and zeolite. These mineral associations are indicative of low-temperature interactions between rocks and seawater-derived fluids. This paragenesis is typical of the lowest-temperature stage of oceanic crust alteration (also known as "seafloor weathering" stage) (Alt, 1995). Temperature estimates for smectite (nontronite) formation are within the range of 30° to <150°C.

F26. Loss on ignition vs. depth, p. 56.

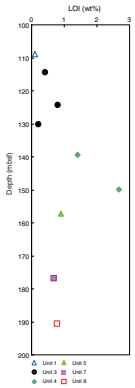

The presence of Fe oxyhydroxide and smectite (nontronite and saponite) suggests circulation of large volumes of oxidizing fluids within the lava pile with a coeval precipitation of Ca carbonate (calcite) and zeolite formation.

PALEOMAGNETISM

Pass-through cryogenic magnetometer measurements were taken on all split-core archive sections and a few discrete samples from working sections. In addition, magnetic susceptibility (MS) was measured for whole cores, all archive-half core sections, and discrete samples. Coherent basalt pieces that could be oriented unambiguously with respect to the top were measured at 1-cm intervals. In order to isolate the characteristic remanent magnetization (ChRM), archive-half core sections were subjected to alternating-field (AF) cleaning. The number of AF demagnetization steps and peak field intensity varied, depending on lithology and the natural remanent magnetization (NRM) intensity. On average, the basalt half cores were treated using a minimum of eight AF steps. The maximum applied field ranged between 40 and 70 mT. A total of 26 minicores (~10.5 cm^3 in volume) were taken from the working halves for AF treatment. Of these, five samples were each cut into two subminicores (5.2 cm^3 in volume) before AF treatment for the purpose of comparison between AF and thermal treatments. One set of the subdiscrete samples was stepwise thermally demagnetized to 580°C, to determine the directional stability during stepwise demagnetization, to verify the pass-through measurement from the cryogenic magnetometer, and to help identify the magnetic mineralogy. All the other samples were progressively AF demagnetized up to a peak field of 70 mT. We analyzed all results from long-core and discrete samples in Zijderveld and stereoplot diagrams and calculated the ChRM direction using principal component analysis (Kirschvink, 1980). To investigate rock magnetic properties, we also conducted isothermal remanent magnetization (IRM) experiments on some of the previously AF-treated discrete samples followed by thermal demagnetization of the IRM samples.

Split-Core Section Pass-Through Measurements

One of the major experimental requirements in paleomagnetic research is to isolate the ChRM by selective removal of secondary magnetization. In Figure F27, we show the NRM intensities and inclinations before and after 25-mT AF demagnetization for all the recovered cores. All split-core and discrete samples exhibited strong signs of drilling-induced remagnetization (overprint), as shown by the NRM inclinations that are strongly biased toward relatively high positive values (with a mean of +40°), which are significantly higher than that expected for the actual geocentric axial dipole inclination at Site 1243 (~+10°). The effect of removing this overprint by AF cleaning is a significant decrease in intensity, from a mean value of 3.3 A/m (all measurements without cleaning) to 1.7 A/m (all measurements after 25 mT cleaning) and a shift toward shallower or even negative inclination (Fig. F27). Although the amount and coercivity of overprinting varied, most of it seems to be removed with 25- to 35-mT AF demagnetization for the majority of samples, allowing us to isolate the ChRM direction using the principal component analysis method on higher field demagnetization steps. For rocks from Cores 203-1243B-6R through 7R, the drill-

F27. NRM intensity and inclination before and after 25-mT AF treatment, p. 57.

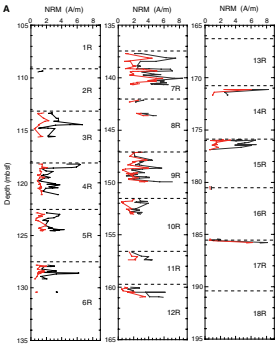

ing overprint is more resistant to demagnetization, requiring AF treatment up to 70 mT to remove most of the overprint. In some cases the ChRM is not resolved, suggesting that additional AF and thermal demagnetization is needed on these cores at a shore-based laboratory.

After the drilling overprint was removed, the intervals measured generally display linear vector paths that trend toward the origin of the vector plots. In Table T5, we list the ChRM direction, NRM intensity, and the maximum angular deviation angle for all coherent basalt pieces longer than 15 cm. A downhole plot of ChRM inclinations is also shown in Figure F28. The 15-cm threshold was considered to be a reasonable size to allow reliable and consistent estimations of directions and magnetization within a sample, as the first few centimeters of both section ends are affected by edge effects. The edge effects translate into an incorrect assumed volume in the ODP database, as determined by the shipboard software used for NRM calculations and bias in directions detected by the 2-G sensor because of the changing geometry of the sample. For coherent pieces longer than 50 cm, we list data roughly every 5 cm and for smaller pieces every 4 or 2 cm, excluding the edges. The ChRM inclinations obtained from different parts of long coherent pieces generally agree within a few degrees as shown in the detailed results from Section 203-1243B-9R-2 represented on Figure F29.

Alternating-Field and Thermal Demagnetization of Discrete Samples

Because many core sections recovered in Hole 1243B contain small and unoriented pieces, long, continuous, and vertically oriented core sections are limited in number. Consequently, oriented samples for shipboard studies had to be shared between research groups. For this reason, we were able to perform AF demagnetization on only 26 discrete samples and thermal demagnetization on 5 of the subsamples, as mentioned previously. Experiments revealed that samples have two magnetic components, a low-coercivity drilling overprint, which is removed after 20- to 50-mT or 400°C demagnetization, and the ChRM. Several representative examples are shown in Figure F30. It appears that thermal demagnetization is more effective in isolating the ChRM. Judging from the unblocking temperatures, the ChRM is carried by a fine-grained magnetite or titanomagnetite. This is further confirmed by IRM acquisition and thermal demagnetization of IRM experiments (Fig. F31).

The ChRM directions from discrete samples agree roughly with those obtained from split-core measurements (note the 180° change in declination resulting from the change from archive- to working-half cores), but the inclinations are shallower in almost all the cases (see blue dots in Fig. F29). Particularly interesting is the variation in demagnetization behavior within a pillow lava of Unit 6, where a pair of closely spaced samples were targeted for a comparison study. As shown in Figure F32, AF demagnetization of 25 mT on Sample 203-1243B-12R-1, 85–87 cm, removes the drilling-induced overprint and reveals a well-defined ChRM component. The drilling-induced remagnetization component is more resistant to AF demagnetization for Sample 203-1243B-12R-1, 88–90 cm, which is only 1 cm distant from Sample 12R-1, 85–87 cm (see inserted core photo in Fig. F32). The ChRM in this sample (Sample 203-1243B-12R-1, 88–90 cm) was not revealed until after 50-mT demagnetization. We propose that as this sample is farther away from the chilled margin it may contain a higher concentration of multido-

T5. Results of paleomagnetic analyses of cores, p. 80.

F28. ChRM inclinations, p. 59.

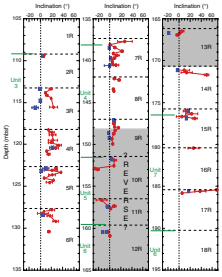

F29. ChRM intensity, declination, and inclination, p. 60.

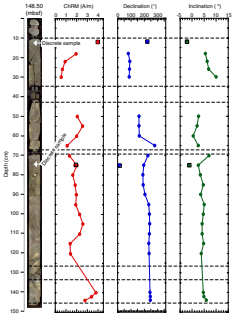

F30. Representative vector endpoint diagrams, p. 61.

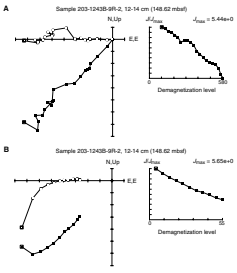

F31. Acquisition and thermal demagnetization of IRM, p. 62.

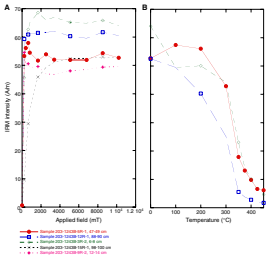

main titanomagnetite grains more sensitive to the drilling overprint. This explanation is consistent with observations made on magnetic properties of young MORB (e.g., Carlut and Kent, 2002).

Magnetic Polarity

A reliable magnetostratigraphy at Site 1243 is hampered by several factors. First, recovered cores at Site 1243 are azimuthally unoriented; therefore, the declination does not provide direct evidence for magnetic polarity. Second, although it is a common practice to use the magnetic inclination derived from the ChRM as the indicator of magnetic polarity where positive inclinations indicate normal polarity and negative inclinations indicate reversed polarity (for Northern Hemisphere sites), positive and negative inclinations at Site 1243 are not reliable indicators for polarity changes. Because Site 1243 was located only 3°N of the equator 11 m.y. ago (Pisias et al., 1995), the corresponding mean magnetic inclination would change only ~12° from a normal state to a reversed state (i.e., from ~+6° or ~–6°). Yet, the magnitude of ordinary secular variations during a period of stable polarity at that latitude would encompass >12° (see McFadden et al., 1991). Third, there are no independent age constraints available for the recovered basalt; thus, it is impossible to correlate polarity intervals, if any, with the geomagnetic polarity timescale.

Nevertheless, we tried to use a "statistical" approach to identify the magnetic polarity in this study. The 26 AF-demagnetized discrete samples provide the most reliable estimate of ChRM and, when averaged, give a null mean inclination. This tends to demonstrate that the section encompasses periods of reversed and normal polarity (otherwise, given the sample-set size, a mean close to +6° or –6° should be found). Indeed, variations in inclination, with respect to depth, indicate that drilling in Hole 1243B may have penetrated through a period of magnetic field reversal. The magnetic inclinations for cores in aphyric basalt from Unit 3 show normal polarity, with a mean positive inclination of ~20°. In the plagioclase olivine phyric basalt from Units 4, 5, and 6, the ChRM inclinations of discrete samples range from 0° to –20°, suggesting a reversed polarity zone. The fresh to slightly altered aphyric basalt from Unit 7 once again shows normal magnetization with a mean inclination of ~25°. Two observations need further mention:

1. We note that the negative or near-zero ChRM inclinations are not randomly distributed throughout the sequence but are confined to Cores 203-1243B-7R through 13R, within which most long continuous basalt pieces are contained (Fig. **F29**). Thus, the negative inclinations in these long continuous core sections suggest that these pieces were homogeneously magnetized and lend support to the notion that the ChRM in these core sections may indicate a reversed polarity.
2. As shown in Figure **F28,** there is a discrepancy between mean inclinations calculated using the discrete samples and long-core measurements. The steeper inclination values observed in the long-core measurements may be due to an overprint that has not been completely removed, to paleosecular variation, or to tectonic rotation. For the last possibility, however, we note that the sediment–basement seismic reflection is horizontal and there is no evidence for local tectonic rotation of the basalts at Site 1243.

F32. Vector endpoint diagrams showing the results of AF demagnetization for two samples, p. 63.

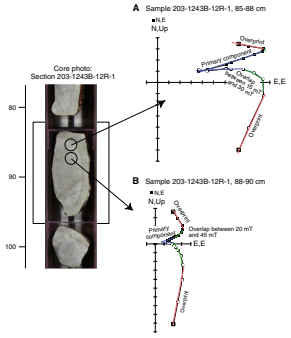

Shore-based studies of discrete samples are required to confirm the polarity results and explain the steep inclination in the long-core measurements. One implication of this polarity result, if confirmed, is that the ChRM data probably give a reasonable indication of the time-averaged direction, and the thin igneous section we cored may have erupted in several phases separated by at least several tens of thousands of years.

Magnetic Susceptibility

MS was measured independently at 2-cm intervals with the Bartington meter along whole-core sections of all cores recovered and every 1 cm on the point susceptibility meter. The two MS data sets compare very well with each other (Fig. F33). Susceptibility peaks in lithologic units commonly correlate with lithologic changes. For example, the peak at 166.4 mbsf (Fig. F33) corresponds to a pillow top at Section 203-1243B-13R-1 [Piece 8]. The higher susceptibility value may be explained by a finer grain size of the pillow lava top. Another signal of particular interest is the sharp peak in MS between 128.60 and 130.49 mbsf, corresponding to intervals in Sections 203-1243B-6R-1 and 2. This peak was verified by further individual sample susceptibility measurements from the minicores that were used for demagnetization experiments. Thus, it is not due to contamination from core liners. We note that the susceptibility maximum also coincides with the stronger NRM intensities in the pass-through magnetic measurements. The origin of this spike is unknown at present. Shore-based rock magnetic studies on discrete samples will be used to investigate the cause of the MS anomaly. Interestingly, this may have implications about whether these strongly magnetized rocks may have remagnetized the rocks in the uppermost part of Unit 4 (Fig. F28).

F33. MS vs. depth, p. 64.

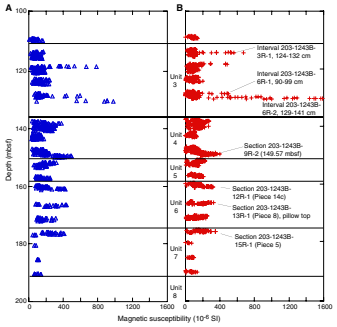

Summary

In summary, the basaltic cores recovered from Site 1243 appear to record a stable component of magnetization with possibly both normal and reversed inclinations after removal of the pervasive drilling-induced remagnetization. Shipboard AF and thermal demagnetization studies and comparison between continuous and discrete samples indicate that some of the drilling-induced magnetization may remain on a part of the long-core measurements even at the highest AF demagnetization level (up to 70 mT) and that thermal demagnetization is probably more effective for removing this component. Preliminary data from IRM acquisition experiments, unblocking temperatures, and coercivity determinations suggest that magnetite and titanomagnetite, with varying titanium content, are the most likely magnetic carriers in these cores. The lava sequence recovered at Site 1243 may have recorded a reversal sequence (normal–reversed–normal). These hypotheses will be tested in subsequent shore-based investigations.

PHYSICAL PROPERTIES

Physical Properties of Basalts

Although the small interval of sediments (26 cm) recovered in Core 203-1243B-1R was disturbed and not suitable for physical properties

measurements, moisture, density, and sonic velocities of 20 basalt samples from Cores 203-1243B-2R through 18R were measured in the laboratory.

The samples were minicores cut from the working half. The minicores are right circular cylinders 2.5 cm in diameter and 2.0–2.2 cm long. The same samples were used to make paleomagnetic measurements. Sonic velocities were measured using the modified Hamilton frame velocimeter (PWS3) then the wet mass was measured as described in "Physical Properties," p. 15, in the "Explanatory Notes" chapter. The samples were then dried for 48 hr at 100°C before the dry mass and dry volume were measured.

Wet bulk densities, grain densities, porosities, and sonic velocities are summarized in Table T6. The sonic velocities range from 4.3 to 5.7 km/s, with a mean of 5.26 ± 0.08 km/s. Porosities range from 4% to 17%, with a mean of 7.7 ± 0.7%. Wet bulk densities range from 2.52 to 2.82, with a mean of 2.69 ± 0.02 g/cm³, whereas the grain densities range from 2.64 to 2.98 g/cm³, with a mean of 2.85 ± 0.02 g/cm³.

The relationships among these properties are summarized in Figure F34. Except for two samples that have particularly high porosities (Samples 203-1243B-7R-1, 106–108 cm, and 14R-1, 36–38 cm) (see Table T6), wet bulk densities decrease markedly with increasing porosity. We also observe a marked decrease of grain density with increasing porosity and a strong increase of wet bulk density with increasing grain density. Lower grain densities are likely to reflect the abundance of low-temperature, low-density alteration products such as clay minerals in the samples. Hence, taken together, these relationships suggest that higher porosities are associated with higher permeabilities, which in turn lead to higher degrees of hydrous alteration.

A relationship between sonic velocity and porosity is expected because cracks in the rock have a profound effect on the elastic properties of the material. Probably because the low-density phyllosilicate minerals produced by alteration also have very low elastic moduli, Figure F34 shows a positive correlation between the sonic velocity and the grain density of the samples. Velocity decreases with increasing porosity and with decreasing grain density. Thus, if the grain density is an index of alteration, the seismic velocities in these samples reflect the combined effects of porosity (cracks) and alteration on the properties of the rocks.

Well Seismic Survey

In addition to the usual suite of downhole logs, including gamma density, porosity, and sonic logs, the Schlumberger WST was used to conduct a seismic survey through the basement section in Hole 1243B. Details of the survey are given in the "Downhole Measurements," p. 22. The data are summarized in Table T7. Data were recorded at eight stations; except for the interval between stations 7 and 8 (at the top of the basement section), the stations were located 10 m apart, and 5–16 shots were stacked at each station to improve the signal-to-noise ratio. Traveltimes were determined automatically by a threshold method. Table T7 lists the average traveltimes and their standard errors (estimated from the standard deviations of the measured traveltimes).

The traveltimes recorded in Table T7 were used to compute interval velocities between the stations; the results are given in Table T8 and shown in Figure F35. The precision of the interval velocities, estimated from the uncertainties in the traveltimes, is 5%–7.5%. Also shown in Figure F35 are the downhole sonic (DTCO) log and the sonic velocities

T6. Physical properties of basalt samples, p. 82.

F34. Physical properties of basalt samples, p. 65.

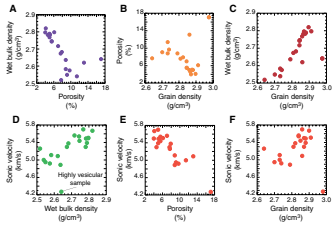

T7. WST data, p. 83.

T8. WST internal velocities, p. 84.

F35. Porosities and measured sonic velocities, p. 66.

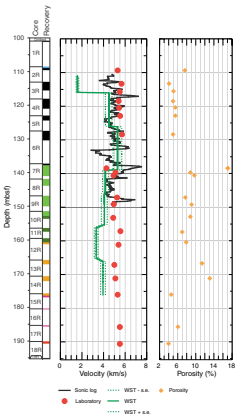

and porosities of the laboratory samples (see Table T6). There is a discrepancy between the WST and downhole log depths and the core depths. The log depths have been adjusted to conform to the core values, which place the top of basement near 110 mbsf.

In general, Figure F35 shows good agreement between the velocities in the laboratory samples, the sonic log, and the well seismic data. The laboratory velocities are, on average, higher (5.26 km/s) than the velocities recorded by the sonic log, which average 4.72 km/s. Cracks cause markedly lower seismic velocities in rocks (e.g., O'Connell and Budiansky, 1974; Kuster and Toksöz, 1974; Gangi, 1978) and are known to have a profound effect on the seismic properties of the uppermost oceanic basement (e.g., Hyndman and Drury, 1976; Wilkens et al., 1991). Thus, the difference between the laboratory velocities and the sonic log probably reflects the presence of large-scale cracks in the formation that are not present in the laboratory samples.

The uppermost interval velocity from the WST survey is anomalously low (1.59 ± 0.12 km/s), which is more characteristic of the overlying sediments than of the basaltic basement. On average, the variation of velocity with depth in deep-sea sediments is given by (Carlson et al., 1986)

$$V(z) = 1.57\exp(-0.33z).$$

Accordingly, the velocity of the sediments overlying basement in Hole 1243B should be near 1.63 km/s. Similarly, the average velocity in the 117-m sediment column in Hole 1243A, where the one-way traveltime is near 0.075 s, is 1.56 km/s. Elsewhere, the WST interval velocities are slightly lower than the sonic velocities (Fig. F35); over the logged interval, excluding the uppermost interval of low velocities, the average of the WST velocities is 4.60 km/s. The difference may be interpreted in two ways. One possibility is that the difference between the WST interval velocities and the sonic log velocities reflects a systematic error in the WST traveltime picks. If so, a more rigorous analysis of the data using correlation techniques will resolve the difference. The second possibility is that the observed difference reflects the different scales to which the sonic log and seismic experiments are sensitive. The sonic tool samples the formation over intervals of 2 ft (0.6 m). Large-scale cracks that occur at intervals of >0.6 m are recorded as dropouts or abrupt minima, such as the one near 133 mbsf in Figure F35. The sonic log is, thus, likely to record the properties of the formation between these features. Seismic waves, on the other hand, sample the formation on scales of tens to hundreds of meters, and the WST interval velocities may, therefore, reflect the presence of cracks that occur on this larger scale.

DOWNHOLE MEASUREMENTS

Logging Operations

The downhole logging program during Leg 203 was comprised of measurements from Holes 1243A and 1243B. Measurements in Hole 1243B were performed first, using the triple combo tool string, the FMS-sonic tool string, and the WST. Two runs were performed with each of the two tool strings and one for the WST. After logging had been completed in Hole 1243B, the ship moved back to Hole 1243A. Logging in Hole 1243A comprised measurements of hole deviation with the Gen-

eral Purpose Inclinometer Tool (GPIT) and cement bond quality with the cement bonding tool (CBT). Although the GPIT was lowered for only one run, the CBT was deployed three times.

Hole 1243B

The first part of the Leg 203 logging program was performed in Hole 1243B, after it had been drilled to a total depth of 195.2 mbsf. Pack-off (PO) zones had been detected during drilling and coring at depths of 142, 159, and below 175 mbsf. Below the last PO zone (175 mbsf), we experienced problems because the lower portion of the hole filled with cuttings. Drilling/coring was stopped because of concern over a possible hole collapse. The bottom of hole (BOH) was established at 184 mbsf. After drilling and coring operations were stopped in Hole 1243B, the borehole was conditioned with a mixture of sepiolite drilling mud and seawater and a wiper trip was conducted. A wiper trip involves pushing the pipe all the way back to the base of the hole and then pulling the bit back to the required depth. The rotary core barrel bit was released at the BOH, and the base of the bottom-hole assembly was pulled up to 79 mbsf (drilling depth). The hole was then ready for logging.

Logging in Hole 1243B started at 1600 hr on 23 June, with wireline rig up. The first tool string (triple combo) was lowered at 1830 hr, passed the end of pipe (EOP) at 82 mbsf (logging depth), and reached the BOH at 2040 hr without difficulties. The depth of the borehole was determined to be 181 mbsf (logging depth; 4049.0 meters below rig floor [mbrf]). The first run was performed logging upward at a speed of 900 ft/hr to the seafloor. The tool was then lowered to the BOH, and a second run was performed logging upward at a speed of 900 ft/hr. Upon completion of the second run, logging with the triple combo tool ended, and the tool string was pulled up, reaching the rig floor at 2345 hr. The tool string was rigged down at 0045 hr on 24 June.

The second tool string (FMS-sonic) was rigged up and lowered downhole at 0145 hr on 24 June. The BOH was reached at 0330 hr, and the tool string was prepared for the first run. The previously determined the BOH logging depth (181 mbsf) was confirmed by this run. The tool string was pulled up at a constant speed of 900 ft/hr until it reached seafloor. The tool was then lowered to the BOH, and a second run was performed at a speed of 900 ft/hr. Logging was completed when the tool string reached the depth of the seafloor. The tool string was then pulled up and reached the rig floor at 0630 hr. The tool string was rigged down by 0715 hr.

The WST was the next tool deployed in Hole 1243B. The ODP generator-injector (GI) air gun (Sodera 210-in^3 Harmonic) was used as the source. The air gun was lowered ~2 m into the water at a 55.8 m offset from the hole, and two hydrophones were attached (one at the source and one below the source). The WST was rigged up and lowered downhole at 0800 hr. It reached the BOH at 1120 hr. Because of spikes on the caliper arms and the small inner diameter of the drill pipe, the WST required a slower speed and closing of the caliper arms many times during descent. Several test measurements (~30–40 shots) were conducted in the drill pipe (at ~1150 mbrf) as well as at the BOH. During these tests, the lower hydrophone gave a bad response, whereas the upper hydrophone gave a very good break signal. Full measurements were performed at station intervals of 10 m beginning at the BOH; each station comprised 10 shots on average. Eight stations within the basement section gave excellent results with high-quality data. The last sta-

tion of the basement section was at 3985 mbrf (117 mbsf, close to the sediment/basement interface). One test shot within the sediment section at 3975 mbrf (107 mbsf) was attempted but yielded poor results because of poor tool contact caused by large borehole diameter. The wireline tension indicated that the tool was slipping downward during attempts to couple the tool to the borehole wall within the sediment section. Consequently, the WST survey was terminated, and the tool was pulled up to the rig floor and rigged down by 1600 hr.

Hole 1243A

The GPIT was the first tool deployed in Hole 1243A. The tool was rigged up and lowered at 2130 hr. It passed the EOP at a depth of 3967 mbrf (drillers depth = 84.6 mbsf) and reached the BOH at 2300 hr. The logging depth to the BOH was determined to be 4088 mbrf (205.6 mbsf). One measurement uphole was performed at a speed of 3600 ft/hr and completed at 3911 mbrf (28.6 mbsf). The tool was pulled up to the rig floor and rigged down by 0045 hr on 25 June.

The CBT was deployed in Hole 1243A to measure cement bond quality. The tool was rigged up and lowered at 0115 hr. The tool reached the BOH at 0330 hr and was pulled up at a speed of 3000 ft/hr. It passed the EOP at a logging depth of 3968.5 mbrf (86.1 mbsf; determined by an increase in gamma ray activity and an increase of transit time from pipe to casing). A second run was performed at the same speed after the tool had been lowered to the BOH. After the second run was completed and the tool was lowered to the BOH, a third run was performed uphole at a speed of 2000 ft/hr and stopped at the EOP. All three runs confirmed the BOH at 4088 mbrf (205.6 mbsf). The tool was then pulled up to the rig floor and rigged down by 0600 hr, at which time logging was completed. The wireline was rigged down at 0800 hr 25 June.

Data Quality

Hole 1243A

The GPIT device recorded only the borehole deviation reliably. Because of the magnetization of the drill pipe and the casing, the magnetometer-derived inclinometry measurements were recorded but may be inaccurate.

The casing bond log (CBL) as well as the variable density log (VDL) showed excellent results within the entire cased hole. The data can be used to determine the depth to the BOH, the top of cement, and, to a certain extent, the bond quality. The starting depths of the three CBT runs were 3908.5 mbrf (26.1 mbsf) for the first run, 3971.4 mbrf (89.0 mbsf) for the second run, and 3970.5 mbrf (88.1 mbsf) for the third run.

Hole 1243B

The deployment of the triple combo, the FMS-sonic, and the WST recorded downhole data of excellent quality and very good repeatability. Despite hole filling at the BOH and breakout zones between 158 mbsf and the BOH, the borehole proved to be in very good shape and gave absolutely no problems from start to finish of the logging operations. The deployment of the Lamont-Doherty Earth Observatory Temperature/Acceleration/Pressure tool yielded no results, probably be-

cause of an internal loss of electrical contact between the sensors and the recording devices. Loss of electrical contact could have occurred at any time between tool closure and opening.

In general, logging data recorded in Hole 1243B range from poor to high quality. In the upper 114.5 mbsf (sediment section), the calipers of the Hostile Environment Litho-Density Sonde (HLDS) and FMS reached their maximum aperture (18 in). Degraded borehole width affects measurements, which require eccentralization and good contact between the tool and the borehole wall. Despite the large borehole size, most of the recorded parameters provide reliable results except for the Dipole Sonic Imager (DSI) and the FMS data. In the sediment section, the wide hole caused problems and the DSI data are unreliable. The DSI recorded low-frequency and high-frequency dipole shear in addition to compressional (*P*)- and shear (*S*)-wave monopole. First motion detection (FMD) was attempted, but no data were obtained for unknown reasons. It appears that the *P*- and *S*-wave monopole and dipole high-frequency tools provided adequate response in the basement section, but the sediment section did not yield any good results. There appeared to be a response in this sediment zone, but it was most likely a tool wave phenomenon observed only at higher gains. The response was simply too rapid to be realistic in such a slow sediment, and the caliper data show that the hole was too large. The high-frequency dipole and *P*- and *S*-wave modes were logged, and the data compared well to the first pass. FMD was again attempted, but no usable data were obtained. FMS data in the sedimentary section are of low quality because the FMS pads did not contact the wall of the enlarged borehole. Most of the time, only one or two pads recorded reliable data.

In the basement section, the HLDS and FMS calipers confirmed that the borehole is enlarged in a few intervals (see **"Results of Log Interpretation,"** p. 26). In these intervals, FMS data quality is highly variable, ranging from poor to good. In the basaltic basement, the HLDS and FMS calipers recorded a borehole diameter ranging from 9.875 to 12.5 in. Shipboard processing provided preliminary FMS images; these images captured most of the important features of the cores.

HLDS density measurement clearly detected the seafloor at 3868.0 mbrf. DSI measurements indicated seafloor at 3866 mbrf (Fig. **F36**), 2 m higher than that detected by the HLDS tool. Above 3866 mbrf, the response from the monopole transmitter-receiver pairs show a fast waveform with a slowness of ~50–55 µs/ft, probably caused by the drill pipe itself. The next significant amplitude recorded exhibited a slowness of ~160–170 µs/ft and is most likely the *S*-wave traveling in the pipe. The slowest wave, with a range of ~200–210 µs/ft, ends at 3866 mbrf, which is most likely the seafloor interface. This very slow waveform, with the velocity of water or mud, could be the response from the seawater behind the drill pipe. As soon as the environment changes to formation around the pipe, this waveform disappears.

A possible mismatch in depth determination of seafloor between the different logging runs has an impact on the measurements. Differences in depth determinations can be related to tool setups as well as to variable cable elongations. To detect these depth mismatches, data from the gamma ray tools (Hostile Environment Gamma Ray Sonde and Natural Gamma Ray Spectrometry Tool) are used to match the various runs with each other. For a first rough estimation, the FMS-sonic data of both runs have been shifted downward, using a constant value of 0.8 m.

F36. Full waveform images from the DSI sonic tool, p. 67.

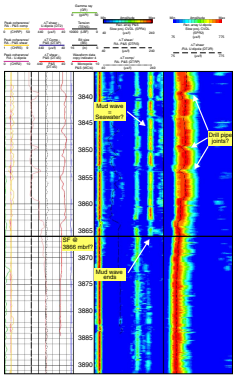

Results of Log Interpretation

Hole 1243A

Logging in Hole 1243A comprised measurements of hole deviation (GPIT) and cement bond quality (CBT) (Fig. F37). The GPIT recorded a hole deviation that does not exceed 1° from the vertical. All three CBL runs indicated a bond/no bond interface at 4037 mbrf (154.6 mbsf) and confirmed the BOH at 4088 mbrf (205.6 mbsf). Bond quality is indicated by the amplitude response of the CBT—lower amplitudes are consistent with good cementing quality. However, low amplitudes can also be produced by other effects, such as tool decentralization or casing collars/joints. Good bond, as seen in relation to no/poor bond areas, is indicated in the following depth ranges: 4040–4045 (157.6–162.6 mbsf), 4058–4063 (175.6–180.6 mbsf), and 4071–4079 mbrf (188.6–196.6 mbsf). Because higher-amplitude readings can be observed periodically, these areas might also be a result of the influence of the casing joints. Thus, the quality estimations have to be regarded with care. Observations from VDL readings, which "look" deeper into the formation, might help to distinguish between artificial effects (e.g., casing joints) and "real" bond quality. Readings below 4083 mbrf (200.6 mbsf), although indicating a good bond zone, have to be interpreted with caution because the tool starts recording reliably a few meters above the lowermost logging depth.

Hole 1243B

To reconcile the difference between the logging depth and the core depth, the core derived lithology has been shifted 6.3 m downward.

The sediment/basement interface was clearly detected at 114.5 mbsf (3982.5 mbrf) in most of the wireline logs. Porosity, density, and resistivity data show the expected changes as soon as the logging tools pass the sediment/basement interface (Figs. F38, F39). In general, the porosity decreases from average values of 89.2% (±9.6%; maximum = 100%) in the sediment section to average values of 14.8% (±4.6%; minimum = 6%) in the basement. In turn, density and resistivity increase. Density increases from average values of 1.50 g/cm³ (±0.10 g/cm³; minimum = 1.11 g/cm³) in the sediments to average values of 2.59 g/cm³ (±0.25 g/cm³; maximum = 3.07 g/cm³) in the basement. Resistivity shows very low average values of 0.59 Ωm within the sediment (minimum = 0.26 Ωm), increasing to average values of 21.09 Ωm (maximum = 48.33 Ωm) in the basement.

No abrupt transition from the sediment to the basement section is evident in the total gamma ray profile (Fig. F38). Within a depth range from 82 to 140 mbsf, gamma ray measurements with an average response of 5.73 American Petroleum Institute gamma ray units (gAPI) only showed small variations of ±2.96 gAPI. The maximum value in this section of 11.1 gAPI was reached at 130 mbsf. This transition points to formations that are not affected by alteration. This was confirmed by core observations (see "Petrology and Geochemistry," p. 10). The gamma ray response appears to be controlled mainly by the potassium content in the formation. Thorium and uranium show minor variations and are roughly anticorrelated.

In the transition from the sediment to the basement section, the amplitude of the sonic waveform (Fig. F40) in dipole acquisition mode (DAM) shows a decrease in slowness from 180–200 to 140–70 µs/ft in

F37. Full waveform images from the CBT, p. 68.

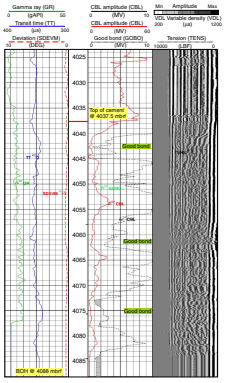

F38. Composite plot of downhole measurements in the sediment and basement section, Hole 1243B, p. 69.

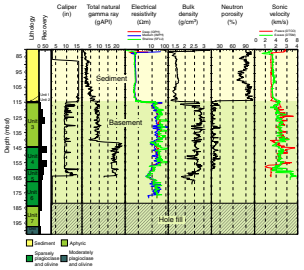

F39. Scatter plots, Hole 1243B, p. 70.

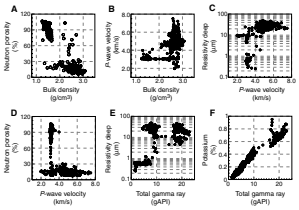

F40. Full waveform images from the DSI, p. 71.

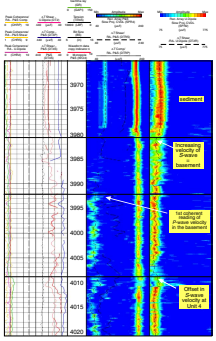

the basement. The sonic waveforms, as inferred from the monopole acquisition mode (MAM) show only minor response, with low coherency in the sediments and often in the basement as well. *S*-waves recorded in this mode yielded poor data in general. The end of the mud wave, from the sediment into the basement, can be regarded as the only qualitative indicator of the beginning of the basement. The first qualitative estimate of *P*-wave velocity was obtained at a depth of 124 mbsf (3992 mbrf).

The detection by core lithology of a thin sediment layer below the first basalt unit (see **"Sedimentology,"** p. 7) at depths of 116–117 mbsf (logging depth) is supported by the downhole porosity and density data. Within this zone, porosity increases slightly to maximum values of 28.9% and density decreases to a lower average of 1.96 g/cm³ (minimum = 1.73 g/cm³) compared to the surrounding basalts. Again, gamma ray response does not seem to be affected by this interlayer. Images derived from FMS data (Fig. **F41**) at a depth of 115.4–116.7 mbsf show a structure that apparently differs from the typical shapes of pillow basalts. This "cloudy" structure suggests the presence of a sediment interlayer.

Below 141.5 mbsf (Fig. **F42**), the gamma ray response increases rapidly up to average values of 18.9 gAPI (±1.6 gAPI; maximum = 23.0 gAPI). This change correlates with a unit change in core lithology from aphyric (Unit 3) to sparsely olivine-plagioclase phyric basalts (Unit 4) (see **"Petrology and Geochemistry,"** p. 10). A small offset in shear wave velocity (DAM) and in mud wave (MAM) at this depth (Fig. **F40**) indicates the beginning of a new unit. In contrast, the *P*-wave as well as the *S*-wave (MAM) velocities show a continuing incoherent response of poor quality. Only the *P*-wave recording begins with a more or less coherent reading, after a small offset in amplitude between 138.8 and 140.7 mbsf (4006.8 and 4008.7 mbrf). FMS images of this transition zone (Fig. **F43**) reveal pillow basalts that are highly fractured and partly vesicular (top of Unit 4), allowing for the detection of a change in lithologic unit.

The increase in total gamma ray at 141.5 mbrf correlates with strong increases in potassium and thorium (Fig. **F44**). This change can be related to the beginning Unit 4. Uranium remains low (~0.1 ppm). The subsequent decrease of potassium (<0.6 wt%) at 144.5 mbsf correlates with an increase in uranium (~0.7 ppm), whereas thorium appears to experience a slightly retarded decrease. Potassium remains low until 155 mbsf, with values of ±0.6 wt%. In that zone, thorium and uranium, partly alternating with each other, are the inferred elements in the total gamma ray reading. Below 155 mbsf, the uranium response appears to drop below the minimum detector threshold, whereas potassium increases again, reaching its maximum of 1.2 wt% at 159.2 mbsf. However, these effects are most likely related to secondary changes within the basalt succession.

F41. FMS image of the sediment–basement transition, p. 72.

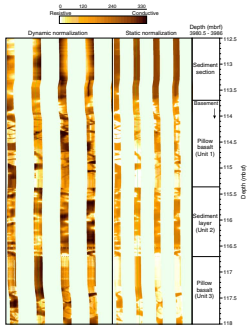

F42. Downhole vs. core measurements, Hole 1243B, p. 73.

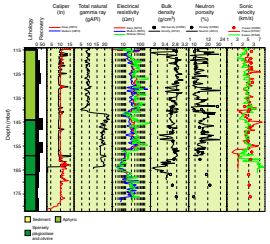

F43. FMS image of a succession of pillow basalts, p. 74.

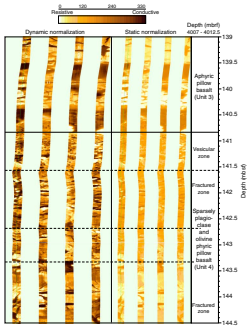

F44. Gamma ray response compared to K, Th, and U readings, p. 75.

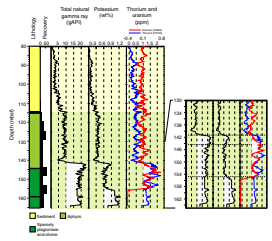

REFERENCES

Alt, J.C., 1995. Subseafloor processes in mid-ocean ridge hydrothermal systems. *In* Humphris, S.E., Zierenberg, R., Mullineaux, L., and Thomson, R. (Eds.), *Seafloor Hydrothermal Systems: Physical, Chemical, Biological and Geological Interactions within Hydrothermal Systems*. Geophys. Monogr., Am. Geophys. Union, 91:85–114.

Bloomer, S.F., and Shipboard Scientific Party, 1992. Underway geophysics. *In* Mayer, L., Pisias, N., Janecek, T., et al., *Proc. ODP, Init. Repts.,* 138 (Pt. 1): College Station, TX (Ocean Drilling Program), 43–63.

Burns, R.G., and Burns, V.M., 1979. Manganese oxides. *In* Burns, R.G. (Ed.), *Marine Minerals*. *Reviews in Mineralogy.* Min. Soc. Am., 6:1–46.

Carlson, R.L., Gangi, A.F., and Snow, K.R., 1986. Empirical reflection travel time versus depth and velocity versus depth functions for the deep sea sediment column. *J. Geophys. Res.,* 91:8249–8266.

Carlut, J., and Kent, D.V., 2002. Grain-size-dependent paleointensity results from very recent mid-oceanic ridge basalts. *J. Geophys. Res.,* 10:1–12.

Dunlop, D.J., and Ozdemir, O., 1997. *Rock Magnetism: Fundamentals and Frontiers:* New York (Cambridge Univ. Press).

Gangi, A.F., 1978. Variation of whole and fractured rock permeability with confining pressure. *Int. J. Rock Mech. Min. Sci.,* 15:249–257.

Hyndman, R.D., and Drury, M.J., 1976. The physical properties of oceanic basement rocks from deep drilling on the Mid-Atlantic Ridge. *J. Geophys. Res.,* 81:4042–4052.

Kirschvink, J.L., 1980. The least-squares line and plane and the analysis of palaeomagnetic data. *Geophys. J. R. Astron. Soc.,* 62:699–718.

Kuster, G.T., and Toksöz, M.N., 1974. Velocity and attenuation of seismic waves in two-phase media, Part I: theoretical formulations. *Geophysics,* 39:587–606.

Le Bas, M.J., Le Maitre, R.W., Streckeisen, A., and Zanettin, B., 1986. A chemical classification of volcanic rocks based on the total alkali-silica diagram. *J. Petrol.,* 27:745–750.

Macdonald, G.A., and Katsura, T., 1964. Chemical composition of Hawaiian lavas. *J. Petrol.,* 5:82–133.

Mayer, L.A., Pisias, N.G., Mix, A.C., Lyle, M.W., Arason, P., and Mosher, D., 1992. Site surveys. *In* Mayer, L., Pisias, N., Janecek, T., et al., *Proc. ODP, Init. Repts.,* 138 (Pt. 1): College Station, TX (Ocean Drilling Program), 93–100.

McFadden, P.L., Merrill, R.T., McElhinny, M.W., and Lee, S., 1991. Reversals of the Earth's magnetic field and temporal variations of the dynamo families. *J. Geophys. Res.,* 96:3923–3933.

O'Connell, R.J., and Budianski, B., 1974. Seismic velocities in dry and saturated cracked solids. *J. Geophys. Res.,* 79:5412–5426.

Pisias, N.G., Mayer, L.A., and Mix, A.C., 1995. Paleoceanography of the eastern equatorial Pacific during the Neogene: synthesis of Leg 138 drilling results. *In* Pisias, N.G., Mayer, L.A., Janecek, T.R., Palmer-Julson, A., and van Andel, T.H. (Eds.), *Proc. ODP, Sci. Results,* 138: College Station, TX (Ocean Drilling Program), 5–21.

Purdy, G.M., 1995. A five year plan. *In* Purdy, G.M., and Orcutt, J.A. (Eds.), *Broadband Seismology in the Oceans—Towards a Five-Year Plan:* Washington (Joint Oceanographic Institutions), 68–75.

Roberts, W.J., Campbell, T.J., and Rapp, G.R., Jr., 1990. *Encyclopedia of Minerals* (2nd ed.): New York (Van Nostrand Reinhold).

Sun, S.-S., and McDonough, W.F., 1989. Chemical and isotopic systematics of oceanic basalt: implications for mantle composition and processes. *In* Saunders, A.D., and Norry, M.J. (Eds.), *Magmatism in the Ocean Basins*. Spec. Publ.—Geol. Soc. London, 42:313–345.

Wilkens, R.H., Fryer, G.J., and Karsten, J., 1991. Evolution of porosity and seismic structure of upper oceanic crust: importance of aspect ratios. *J. Geophys. Res.,* 96:17891–17995.

APPENDIX

Relations between Recovery Rate and Pillow Texture in Hole 1243B, Leg 203

T. Ishii[3]

Pillow textures apparently affected core recovery at Site 1243. The pillows within the igneous sequences of Hole 1243B show the following zonal characteristics from their upper outer crust to their interiors:

1. A black to dark gray glass zone commonly <5 mm thick;
2. A dark gray to brownish gray variolitic zone normally 5–20 mm thick;
3. A gray to pale brown vesicular zone ~20–40 mm thick,
4. A brown to dark brown transitional zone ordinarily up to 100 mm thick; and
5. A dark green crystalline interior.

Lower outer crusts are similarly texturally zoned, but the thickness of the each zone is approximately half or less than those of the upper part. Glass zones are good indicators of pillow boundaries. They may be present on the tops of the pillows (upper glass zone [UGZ]), on the bottoms (lower glass zone [LGZ]), or on both (upper and lower glass zone [ULGZ]), depending upon the mode of pillow formation.

Cored samples were assigned piece numbers. Hole 1243B yielded a total of 359 pieces (with rock samples numbered 5A, 5B, and 5C are counted as one piece) (Table AT1). A glass zone is observed in 46 pieces of rock (12.8%). Among those 46 samples, only 11 pieces can be clearly oriented and assigned to the appropriate lithologic unit; nine pieces (19.6%) are from the UGZ, and two pieces (4.3%) are from the LGZ. No rock piece from the ULGZ was recovered from this hole. Interpillow fragments, including pillow breccia as well as hyaloclastite, were not recovered from Hole 1243B, except for one piece <10 mm in diameter of pillow glass cemented with clay materials (from the cuttings in Section 203-1243B-19B-1). The observed ratio of UGZ to LGZ is 5/1. Two reasons are proposed for the bias toward more glassy tops than bottoms—pillow-lava formation or drilling mechanics or both.

1. Pillow-lava formation: when lava erupts onto the seafloor, the UGZ forms by chilling the hot lava as it comes into contact with cold seawater. On the other hand, the chilling effect on the pillow bottom is less abrupt and hence the LGZ is thinner, because either a pre-existing underlying pillow was still hot or contact with seawater was too brief to chill the lava of the pillow bottom rapidly.
2. Drilling mechanics: abyssal pillows contain many visible radial joints induced by the cooling of magma from the pillow surface to the interior. In addition, incipient radial joints may be induced by the stress of cooling. The rotary core barrel (RCB) bit is 25 cm in diameter, but its throat is only 6 cm in diameter. During drilling with the RCB, the maximum recovered core volume is only ~6% of the volume of rock penetrated by the bit. The proportion of cored rock to cuttings is very small, and any fractures increase the tendency of the rock to be crushed into cuttings

AT1. Glass sample, Hole 1243B, p. 85.

[3]Ocean Research Institute, University of Tokyo, 1-15-1 Minamidai, Nakano-ku, Tokyo 164-8639 Japan.
ishii@ori.u-tokyo.ac.jp

rather than to be transported into the core barrel. This may be one of the primary reasons it is difficult to recover full cores with the RCB, except under very good rock conditions such as coring a massive joint-free rock with moderate hardness.

Pillows form with so many joints that pillow lavas break very easily into drill core pieces at these joints before any drilled cores are pushed into the core barrel. Coring may be more effective in the lower part than in the upper part of the pillow because the glass zone at pillow-on-pillow contacts is far weaker and smoother than is the pillow interior. This may be one of main reasons why we recognize more pillow pieces with UGZ than those with LGZ. Generally speaking, the recovery rates of basement rocks in Hole 1243B are relatively poor, as the rocks collected total only 22.55 m in 85.3 m of penetration. Recovery in three cores (Cores 203-1243B-4R, 7R, and 9R) is 48%–64%. Recovery in the other 14 basement cores reached a maximum of 35% and averaged 20%.

As shown in Table AT1, core recovery rates in Hole 1243B correlate well with the degree of alteration and the existence of visible secondary veins. The three cores mentioned as having good recovery are moderately altered and show fillings. Both alteration and secondary precipitation in some veins were induced by ocean floor diagenesis under low-temperature conditions. Hydrothermal alteration was not observed among the drilled rocks. On the other hand, the rock specimens of the 14 other cores are fresh or only slightly altered and free from joint filling by secondary precipitation. The alteration may weaken rock hardness, and secondary joint filling makes massive and solid rocks out of fragile highly jointed ones. Both effects contribute to the increase in core recovery rates.

Figure F1. Track lines for the Leg 203 site survey, using a single-channel streamer and an 80-in^3 water gun as a source. The east-west tracks are ~5 nmi in length and are separated north-south by 0.5 nmi. The proposed location for the Ocean Seismic Network (OSN)-2 hole was at the location of Site 852, drilled during Leg 138, and is shown on the plot as a triangle. The location chosen for OSN-2 (Hole 1243A) is 0.5 nmi to the north. Hole 1243B was offset 600 m to the east of the final OSN-2 site. The various navigational waypoints (WPs) are shown as diamonds with labels.

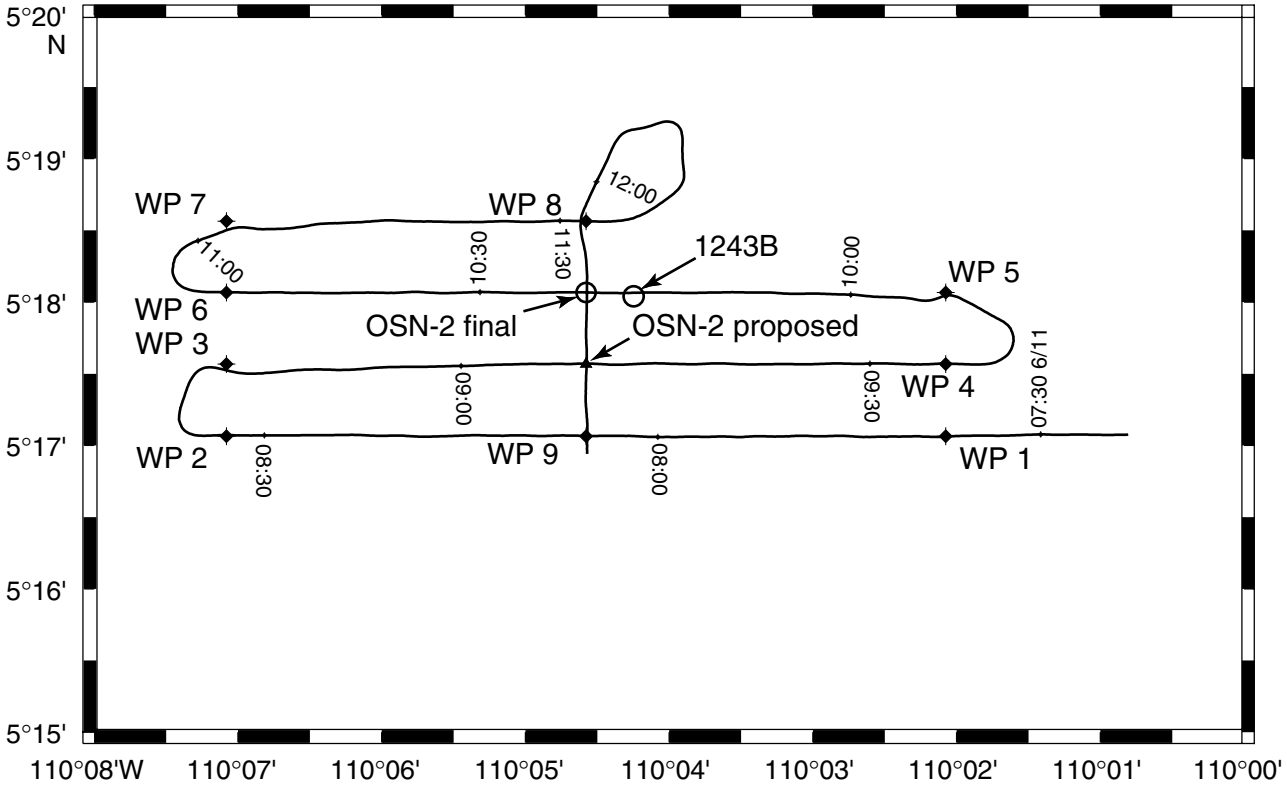

Figure F2. The seismic reflection line between waypoints 5 and 6 (west to east) is shown with the eventual location of Hole 1243A Ocean Seismic Network (OSN)-2. The basement is a clear reflection at the bottom of the sediments, with a TWT of ~0.15 s. The basement reflection is often associated with reflection hyperbolae associated with minor roughness. Two bad traces associated with an eventual loss of an air gun can be seen at ~1031 Universal Time Coordinated (UTC) (bottom axis) and 1039 UTC.

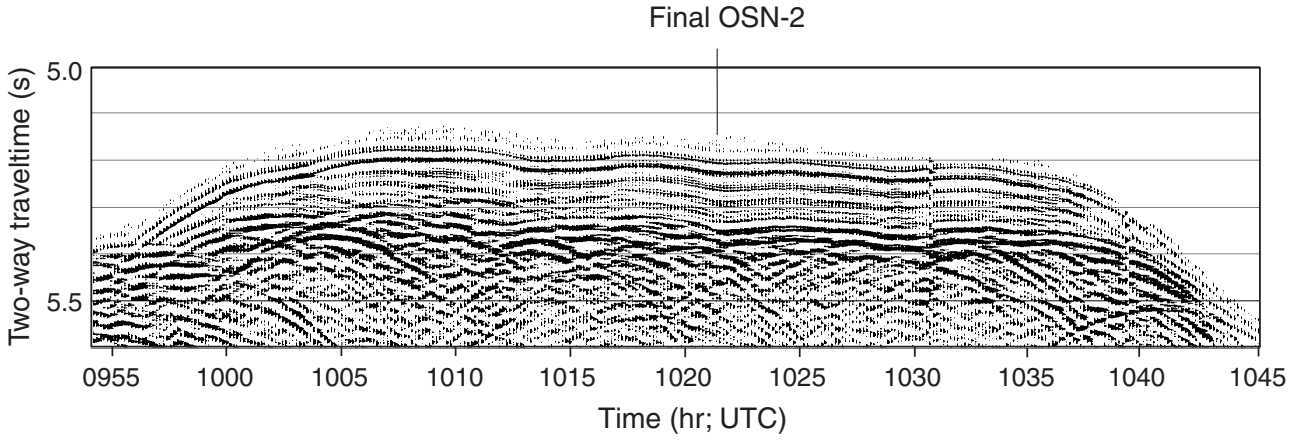

Figure F3. The seismic profile collected between waypoints 8 and 9, which is coincidental with the profile collected for Leg 138, is shown with markers showing the location of the original Site 852 and the site selected for Hole 1234A Ocean Seismic Network (OSN)-2. The basement is quite clear in this direction, and few reflection hyperbolae are observed. UTC = Universal Time Coordinated.

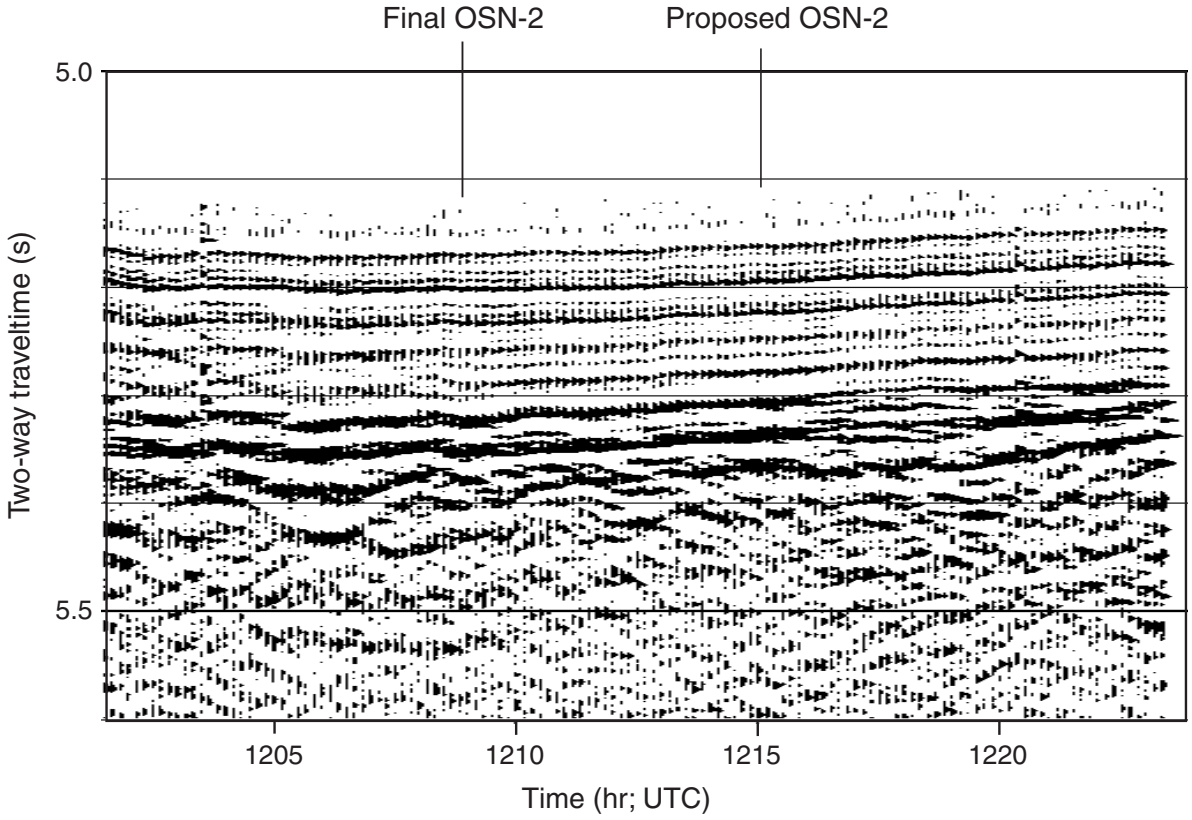

Figure F4. This profile, between waypoints 5 and 6, has been migrated using a frequency-wavenumber technique. The profile can be compared directly with Figure F2, p. 32. The reflection hyperbolae that obscured the basement at the site of Hole 1243A have been collapsed into variations in basement topography. Note, for example, the removal of the large hyperbola at ~1005 UTC. OSN-2 = Ocean Seismic Network-2, UTC = Universal Time Coordinated.

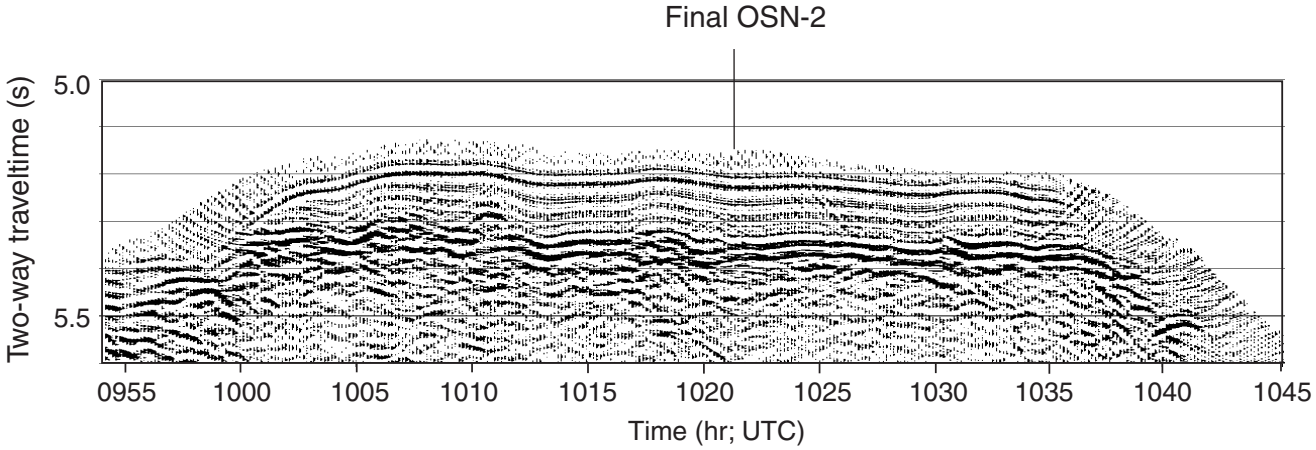

Figure F5. The data from Figure F2, p. 32, were migrated at 1700-m/s sediment velocity compared to the 1500-m/s velocity used in Figure F4, p. 34. Generally, the reflection hyperbolae have been over migrated into "smiles" in this case. Because of this overmigration, we have elected to use a migration velocity of 1500 m/s throughout. UTC = Universal Time Coordinated.

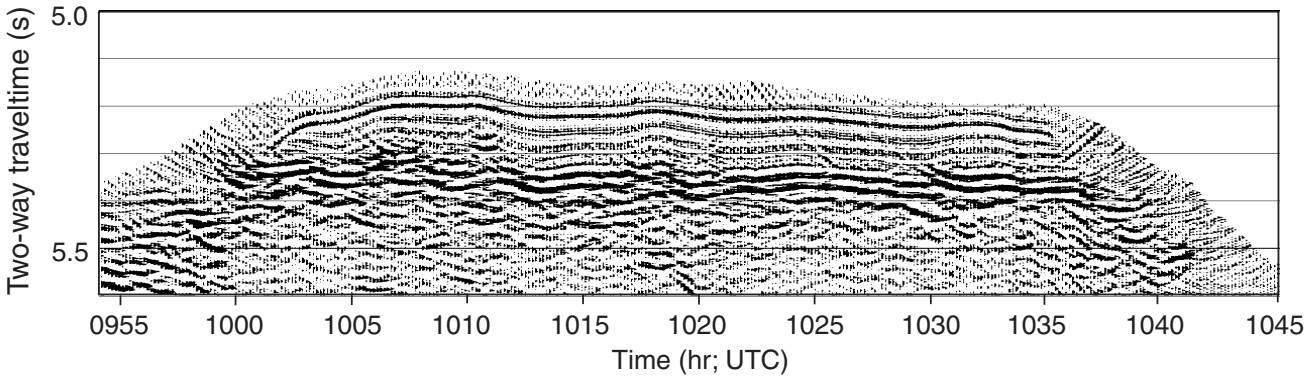

Figure F6. This figure shows the result of migrating the data along profile 5–6, using a medium velocity of 1500 m/s. Although frequency-wavenumber migration is computationally efficient, migration using a finite-difference scheme is often superior. Despite the fact that the results are satisfactory, the additional computational complexity is not merited by any perceived improvement in resolving the sediment/basement interface. Consequently, we chose frequency-wavenumber migration for routine processing of the data. OSN-2 = Ocean Seismic Network-2, UTC = Universal Time Coordinated.

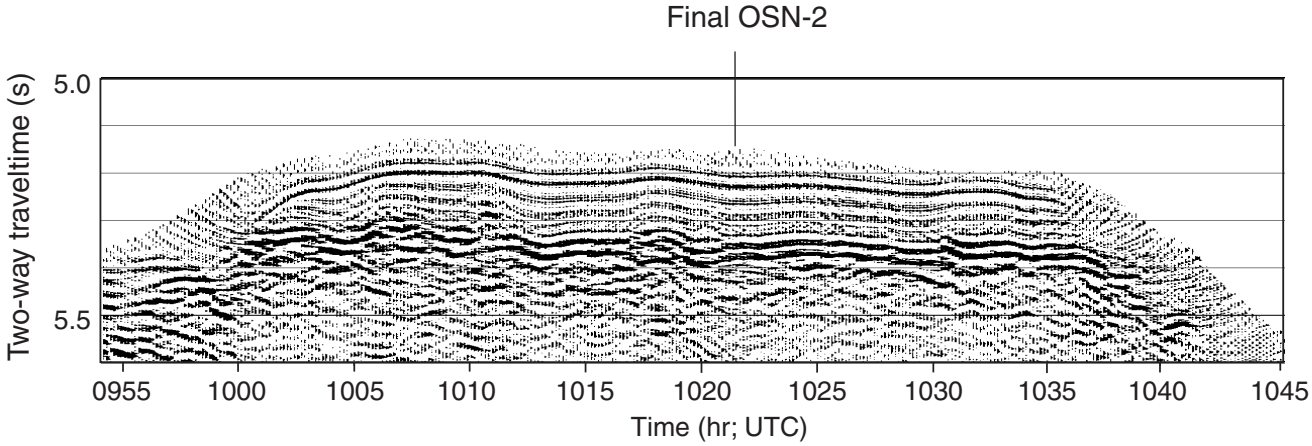

Figure F7. The data in Figure F3, p. 33, along the north-south line between waypoints 8 and 9, were migrated using the frequency-wavenumber method and a medium velocity of 1500 m/s. The basement reflection is quite clear. Comparison of this figure to Figure F4, p. 34, makes it clear that the basement is rougher in an east-west direction than in a north-south direction. This is fully consistent with the anisotropy in seafloor roughness associated with the original spreading direction (roughly east-west). OSN-2 = Ocean Seismic Network-2, UTC = Universal Time Coordinated.

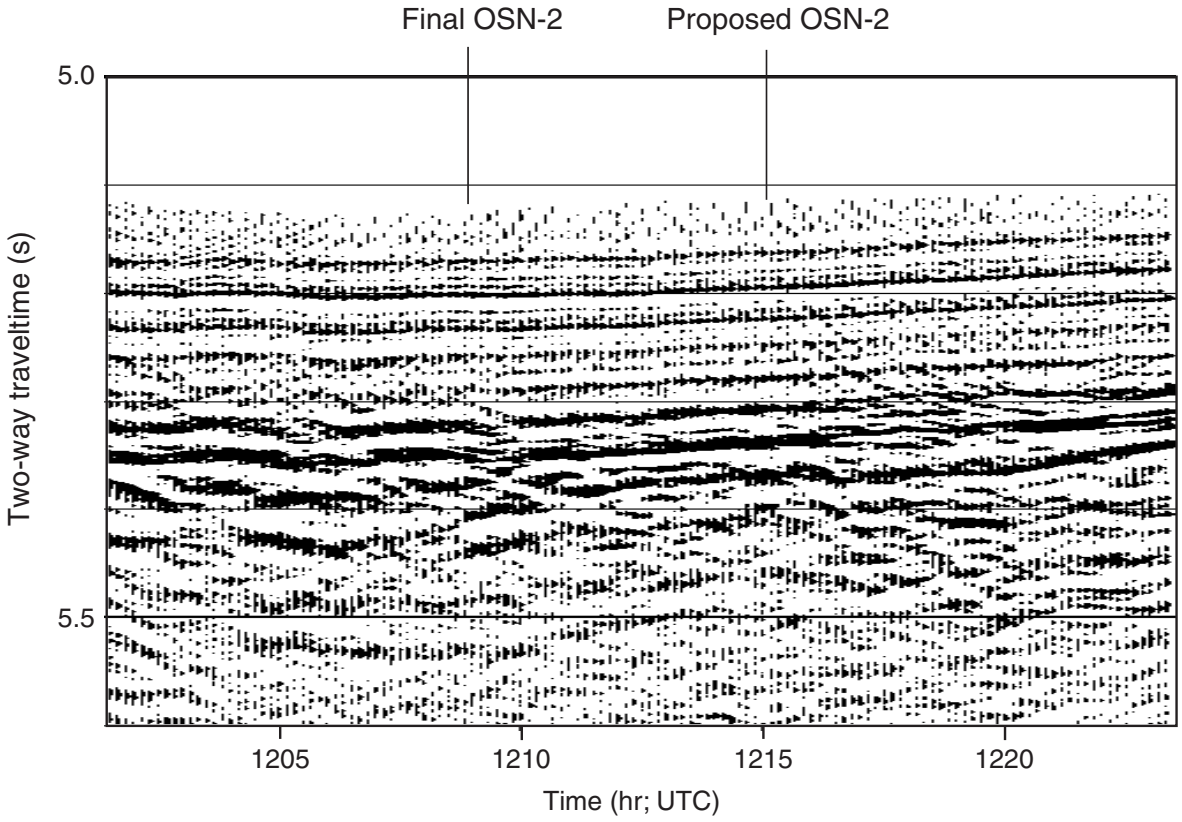

Figure F8. Lines 5–6 (see Fig. F1, p. 31) from the site survey, migrated, showing the locations of Holes 1243A and 1243B. OSN-2 = Ocean Seismic Network-2. UTC = Universal Time Coordinated.

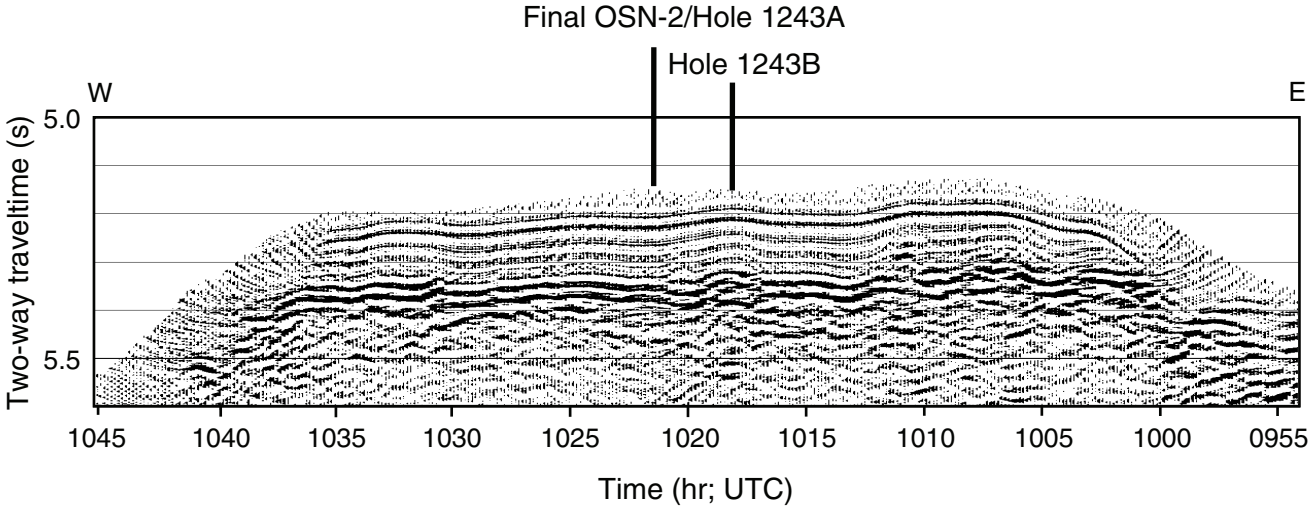

Figure F9. Schematic representation of Hole 1243A.

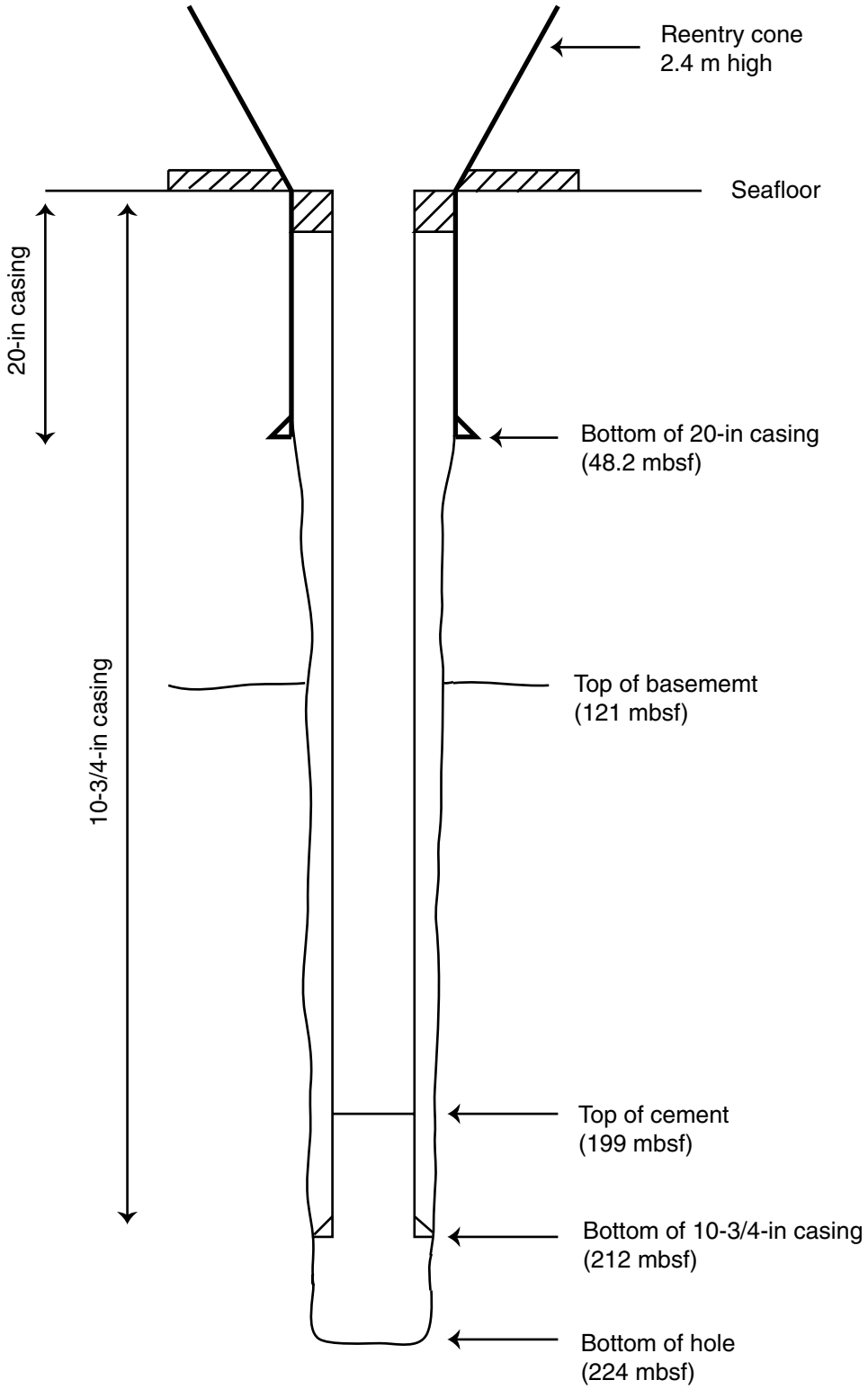

Figure F10. A. Close-up photograph of the cut surface of limestone Sample 203-1243B-2R-1, 45–47 cm. **B.** Photomicrograph of a thin section of limestone (foraminiferal micrite with spar cement between grains and filling burrows) Sample **203-1243B-2R-1, 47–49 cm** (field of view = ~1.5 mm; photomicrograph 1243B-41).

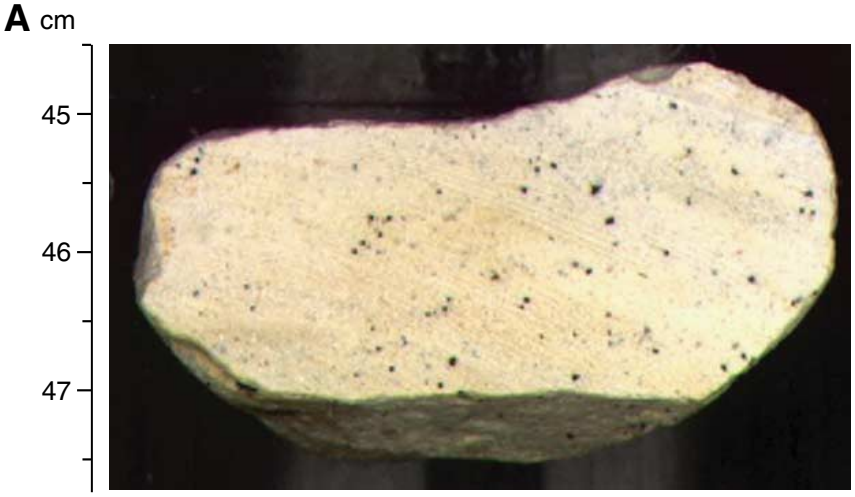

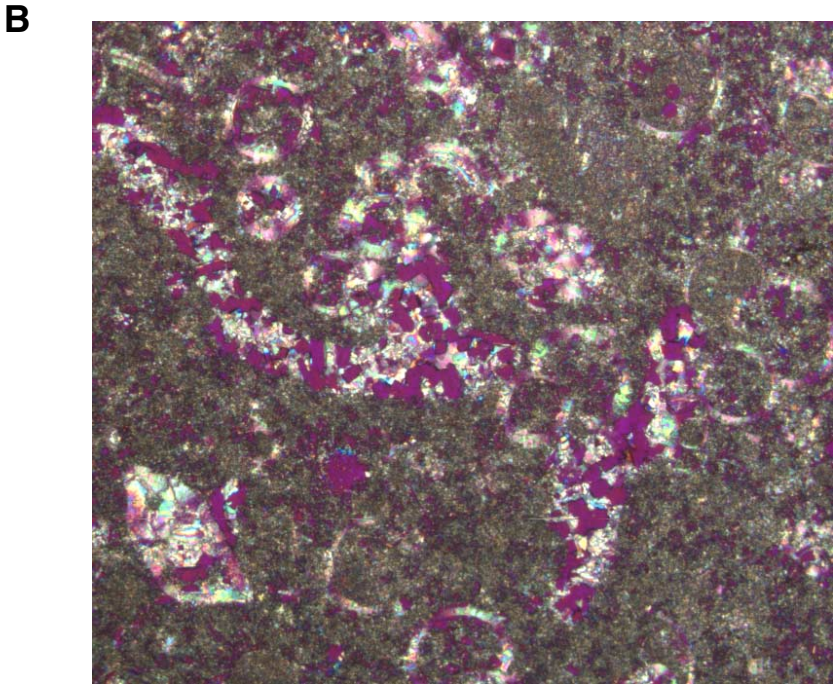

Figure F11. Lithology summary of Hole 1243B. The recovery, unit color code, unit number, phenocryst content, vesicularity, and degree of alteration are presented from left to right. T.D. = total depth.

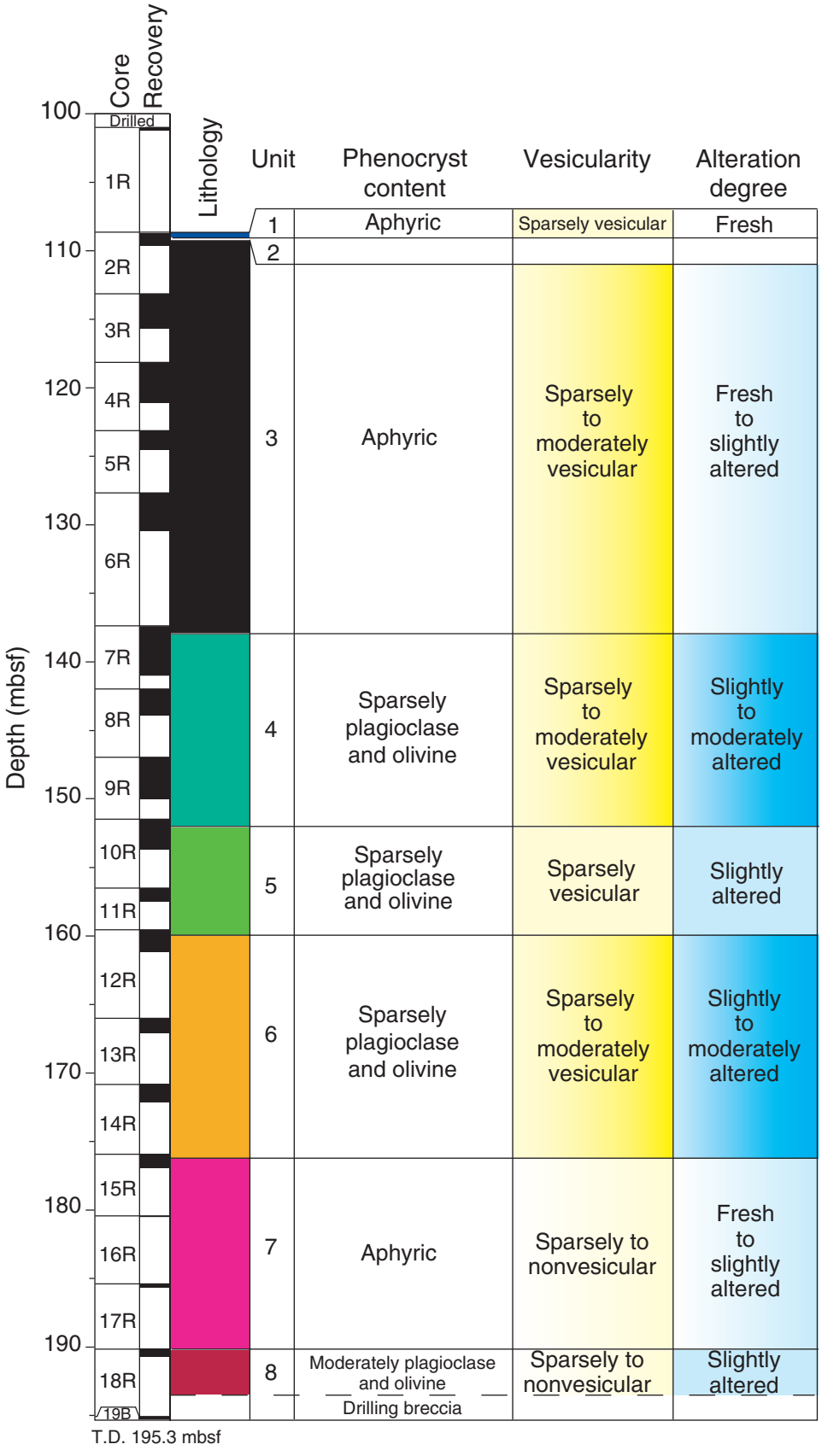

Figure F12. Main macroscopic and microscopic characteristics of Unit 1. **A.** Interval 203-1243B-2R-1, 23–30 cm. **B.** Sample **203-1243B-2R-1, 23–25 cm** (plane-polarized light [PPL]; field of view = 2.75 mm; photomicrograph 1243B-2). **C.** Sample **203-1243B-2R-1, 23–25 cm** (cross-polarized light [XPL]; field of view = 2.75 mm; photomicrograph 1243B-3).

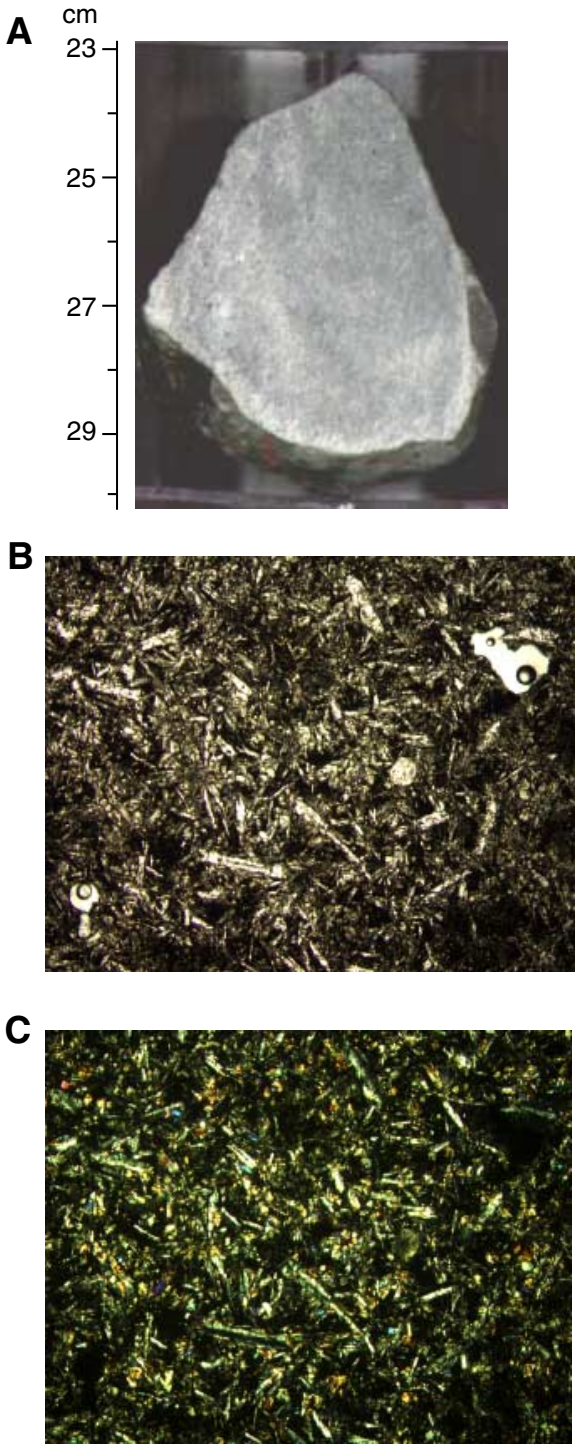

Figure F13. Main macroscopic and microscopic characteristics of Unit 3. **A.** Interval 203-1243B-3R-1, 8–27 cm. **B.** Sample **203-1243B-5R-2, 29–32 cm** (PPL; field of view = 2.75 mm; photomicrograph 1243B-28). **C.** Sample **203-1243B-5R-2, 29–32 cm** (XPL; field of view = 2.75 mm; photomicrograph 1243B-26).

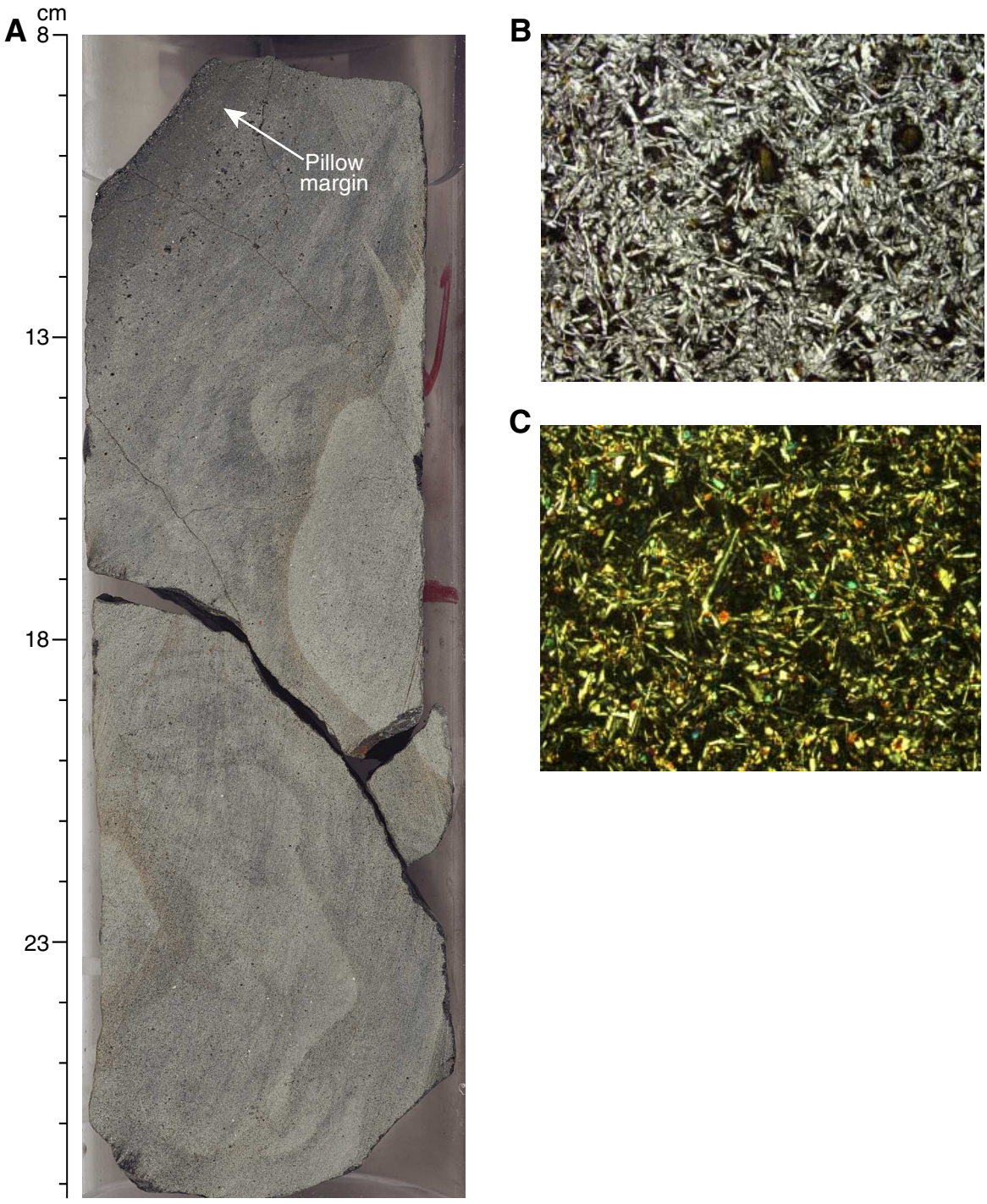

Figure F14. Main macroscopic and microscopic characteristics of Unit 4. **A.** Interval 203-1243B-8R-1, 29–40 cm. **B.** Sample **203-12437B-7R-2, 74–77 cm** (PPL; field of view = 2.75 mm; photomicrograph 1243B-5). **C.** Sample **203-1243B-7R-2, 74–77 cm** (XPL; field of view = 2.75 mm; photomicrograph 1243B-6). **D.** Sample **203-1243B-9R-2, 138–141 cm** (PPL; field of view = 2.75 mm; photomicrograph 1243B-35).

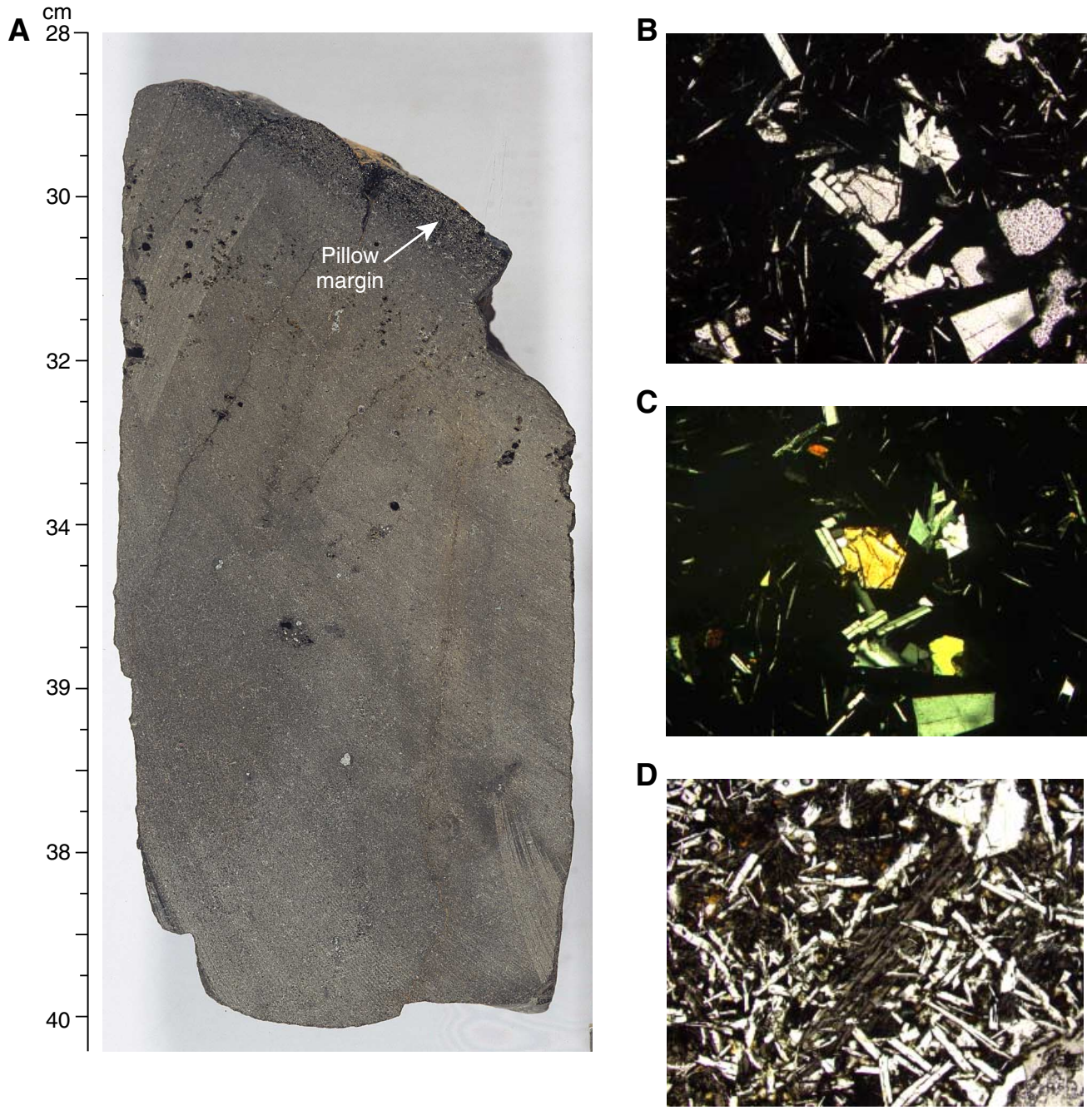

Figure F15. Main macroscopic and microscopic characteristics of Unit 5. **A.** Interval 203-1243B-11R-1, 11–20 cm. **B.** Sample **203-12437B-11R-1, 51–53 cm** (XPL; field of view = 2.75 mm; photomicrograph 1243B-14). **C.** Sample **203-1243B-11R-1, 51–53 cm** (XPL; field of view = 2.75 mm; photomicrograph 1243B-13). **D.** Sample **203-1243B-10R-2, 12–15 cm** (XPL; field of view = 2.75 mm; photomicrograph 1243B-12). **E.** Sample **203-1243B-10R-2, 12–15 cm** (PPL; field of view = 2.75 mm; photomicrograph 1243B-11).

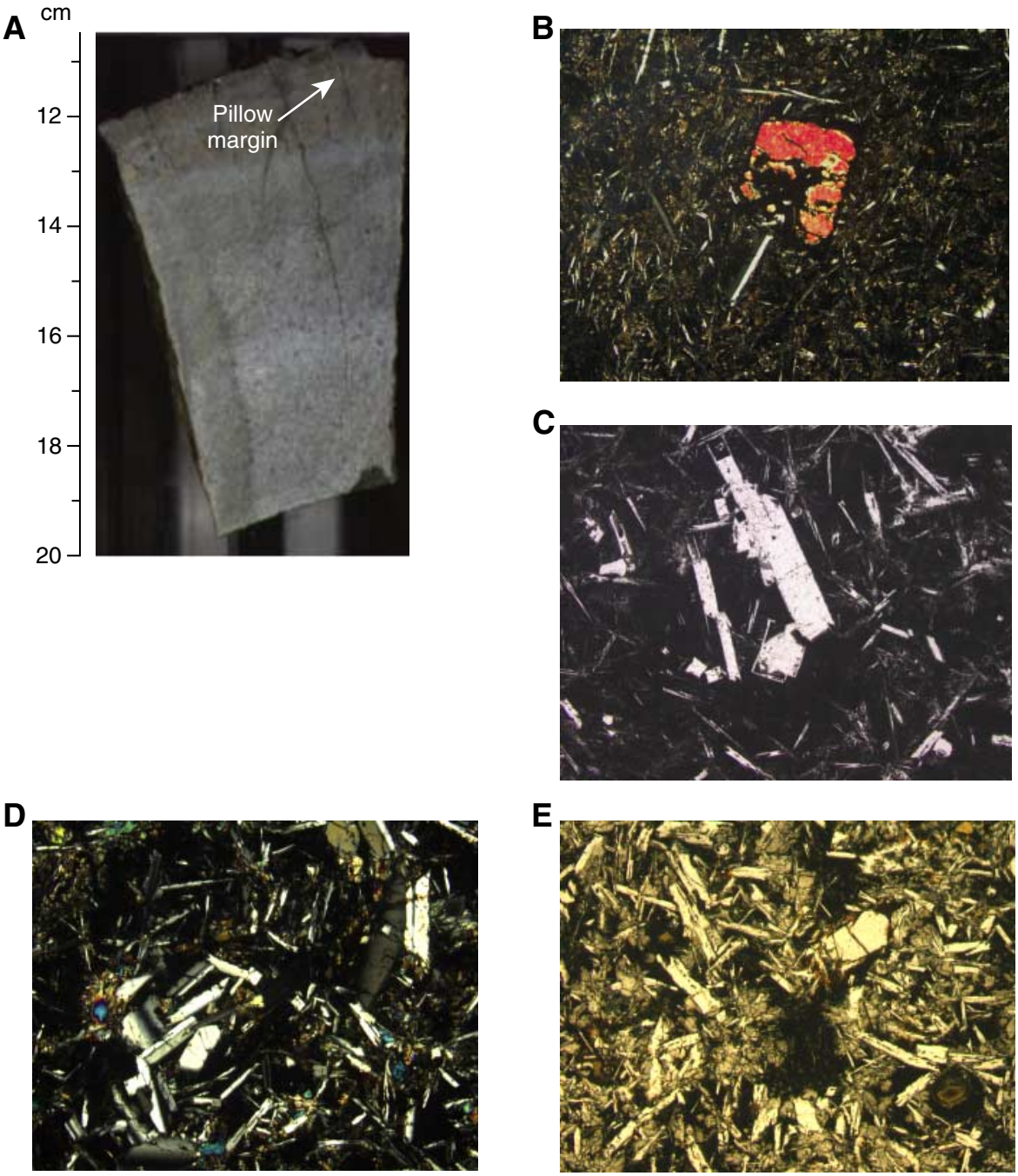

Figure F16. Main macroscopic and microscopic characteristics of Unit 6. **A.** Interval 203-1243B-13R-1, 55–67 cm. **B.** Sample **203-12437B-12R-1, 136–140 cm** (PPL; field of view = 2.75 mm; photomicrograph 1243B-42). **C.** Sample **203-1243B-13R-1, 84–87 cm** (PPL; field of view = 2.75 mm; photomicrograph 1243B-43) **D.** Sample **203-1243B-13R-1, 84–87 cm** (XPL; field of view = 2.75 mm; photomicrograph 1243B-44).

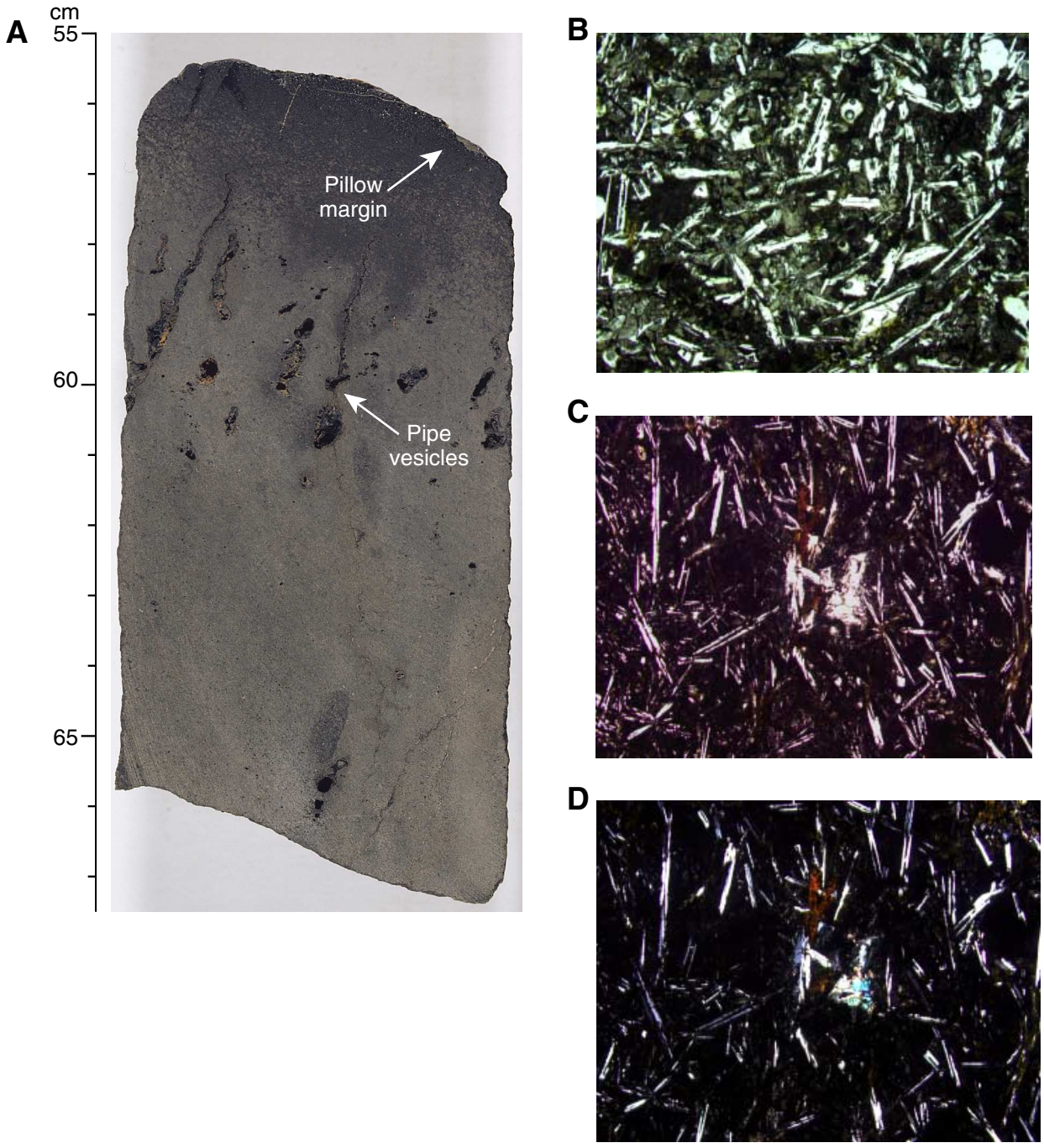

Figure F17. Main macroscopic and microscopic characteristics of Unit 7. **A.** Interval 203-1243B-17R-1, 0–21 cm. **B.** Sample **203-12437B-17R-1, 17–19 cm** (PPL; field of view = 2.75 mm; photomicrograph 1243B-45). **C.** Sample **203-1243B-15R-1, 84–87 cm** (PPL; field of view = 2.75 mm; photomicrograph 1243B-46).

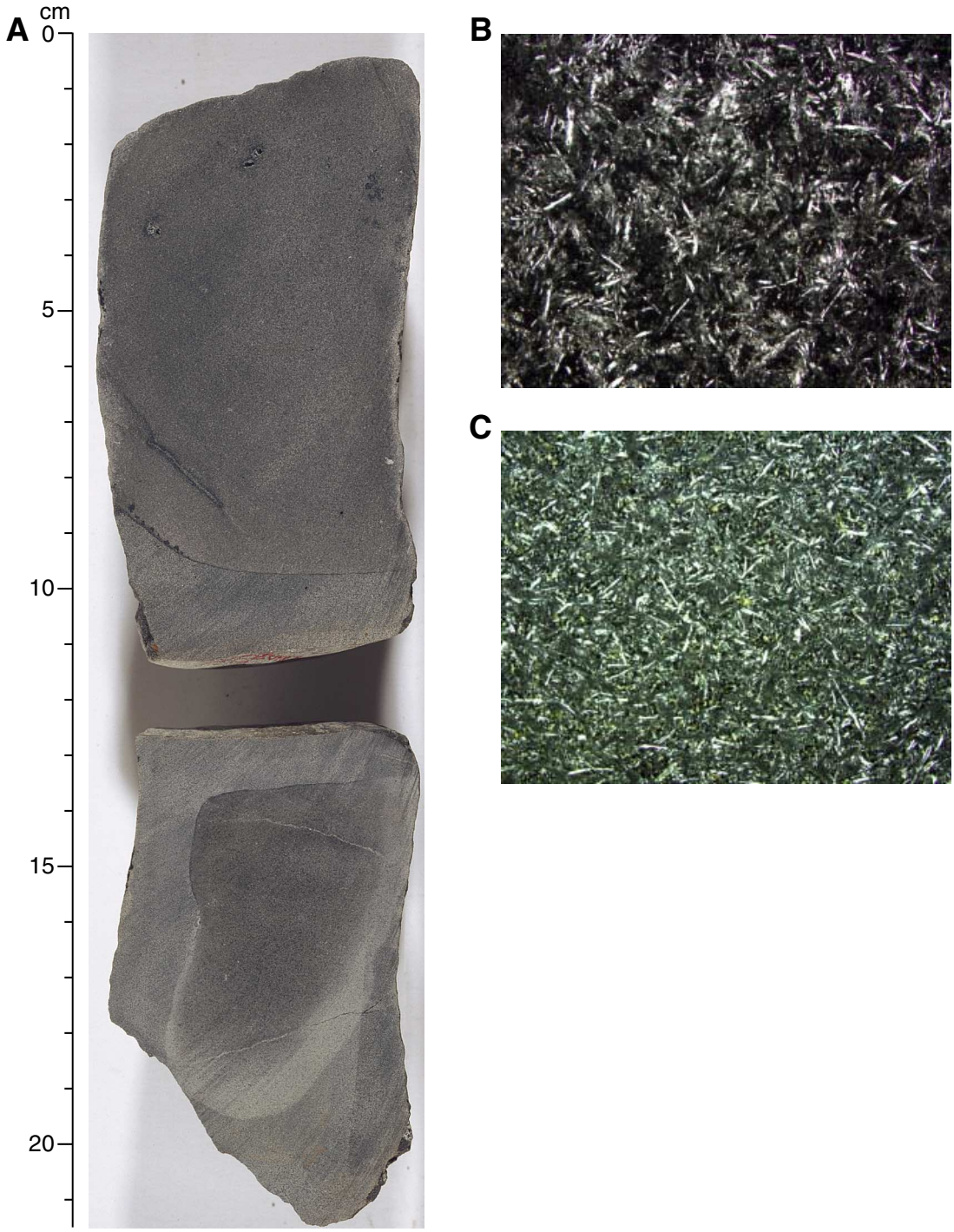

Figure F18. Main macroscopic and microscopic characteristics of Unit 8. **A.** Interval 203-1243B-18R-1, 28–53 cm. **B.** Sample **203-12437B-18R-1, 23–26 cm** (PPL; field of view = 2.75 mm; photomicrograph 1243B-47). **C.** Sample **203-1243B-18R-1, 23–26 cm** (PPL; field of view = 2.75 mm; photomicrograph 1243B-49). **D.** Sample **203-1243B-18R-1, 23–26 cm** (XPL; field of view = 2.75 mm; photomicrograph 1243B-48).

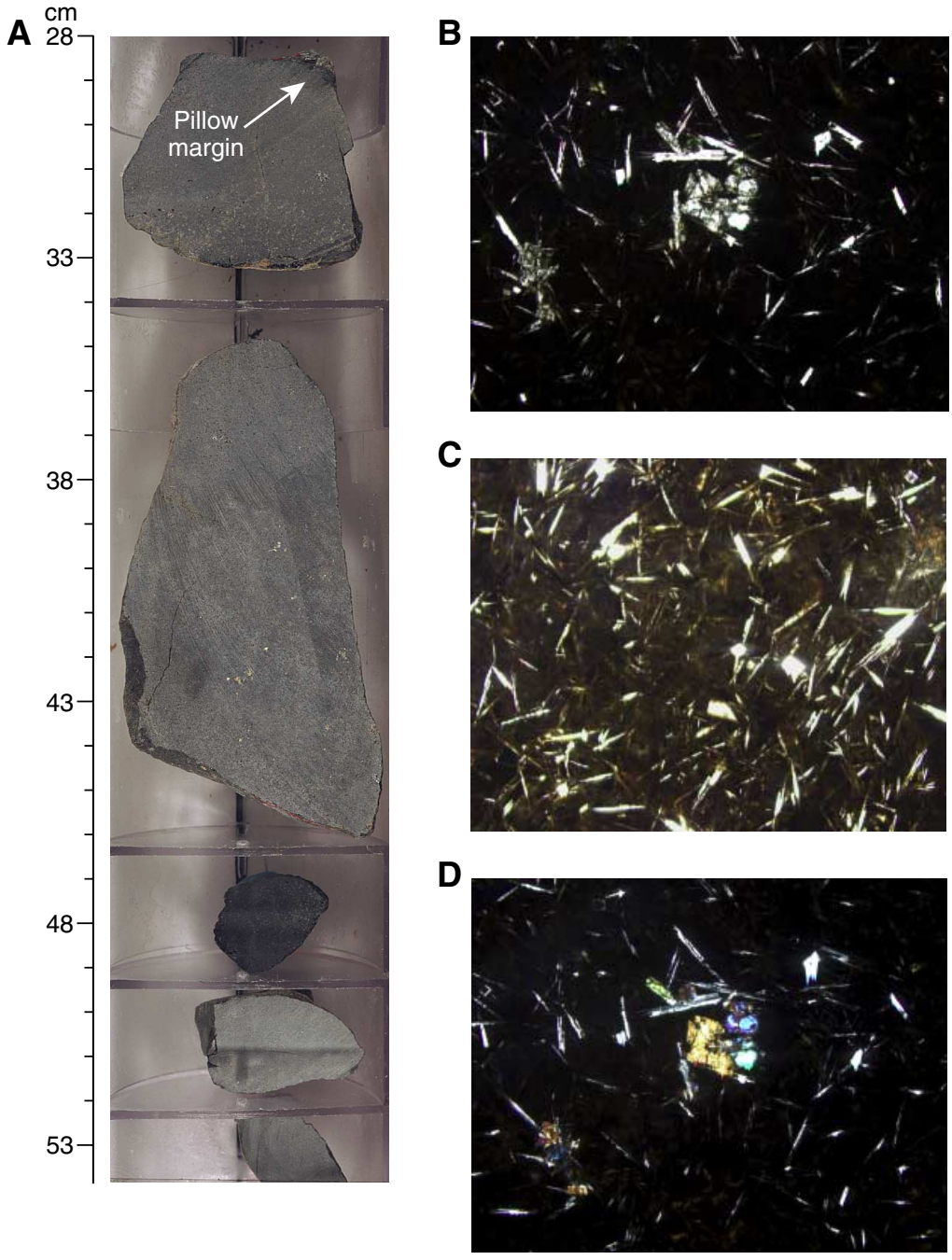

Figure F19. Hole 1243B igneous rock composition on the $Na_2O + K_2O$ vs. SiO_2 (in weight percent) classification diagram (Le Bas et al., 1986). Alkalic and tholeiitic basalt fields are separated by the Macdonald and Katsura (1964) line.

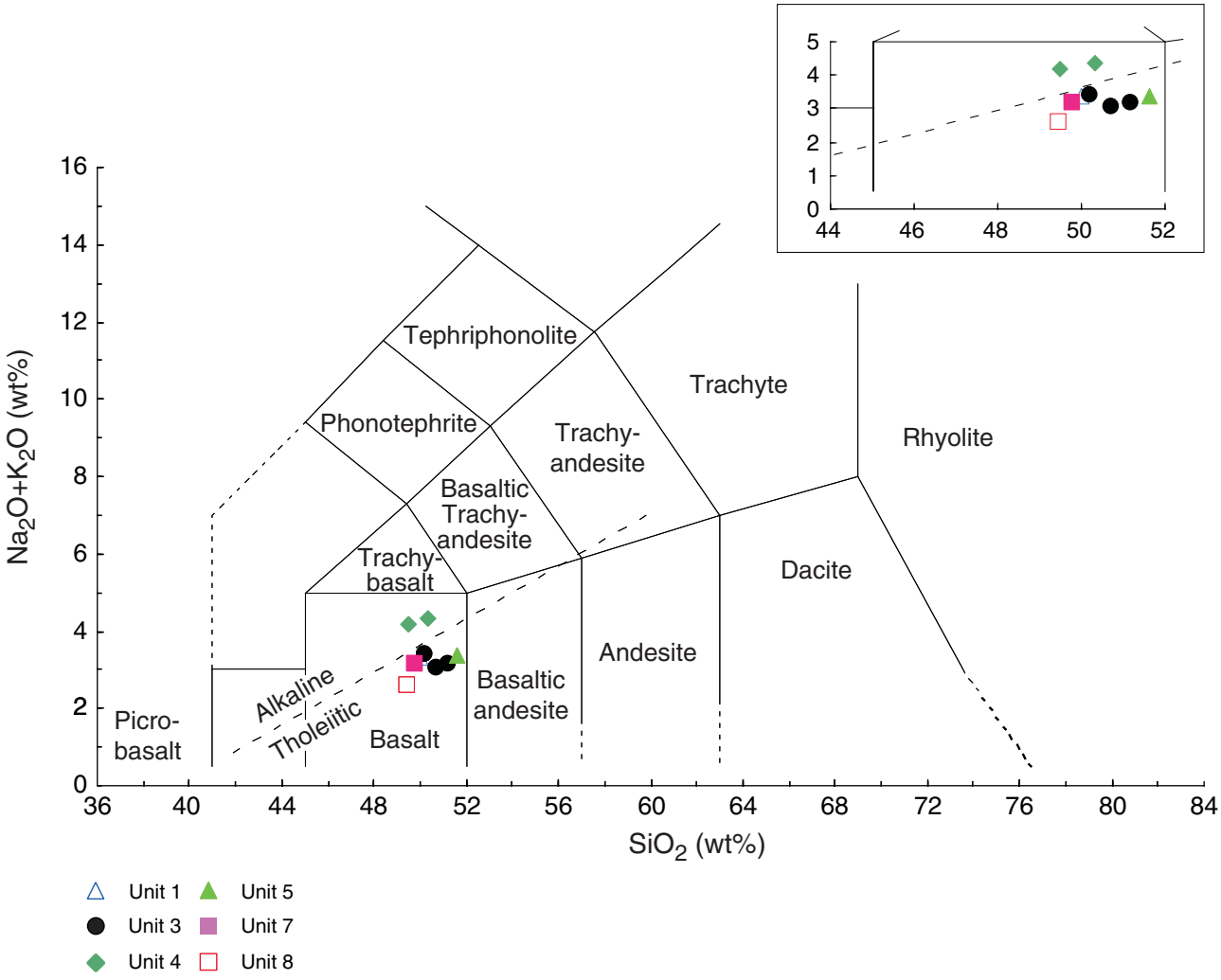

Figure F20. Downhole variations of Al_2O_3 and trace element ratios through basement Units 1, 3, 4, 7, and 8. T.D. = total depth.

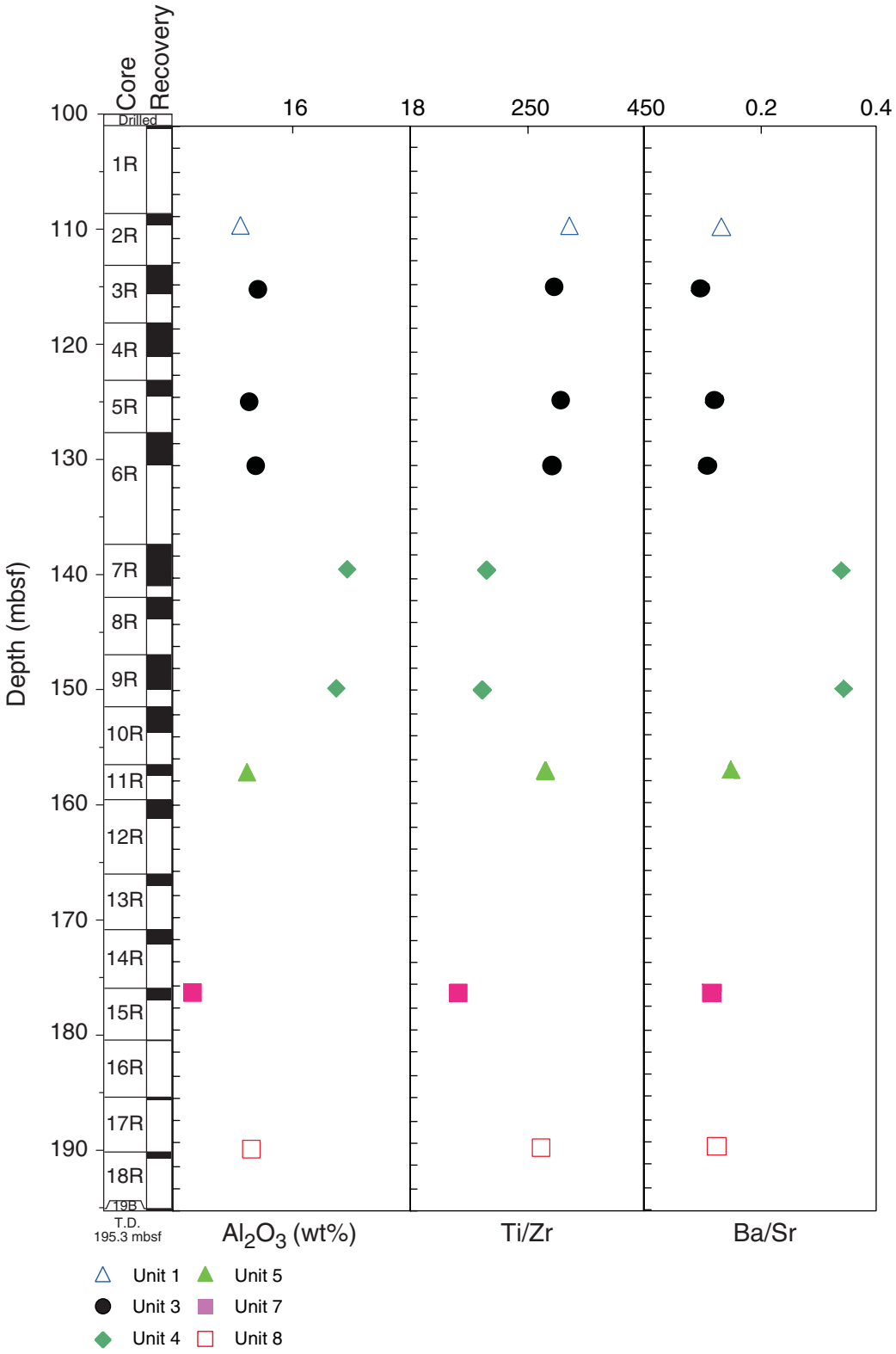

Figure F21. Al_2O_3 and Ti/Zr ratios vs. Mg#. These indicate that tholeiitic basalt of Units 1, 3, 5, 7, and 8 are probably derived from a similar mantle source, whereas alkalic basalt of Unit 4 are derived from an enriched mantle source.

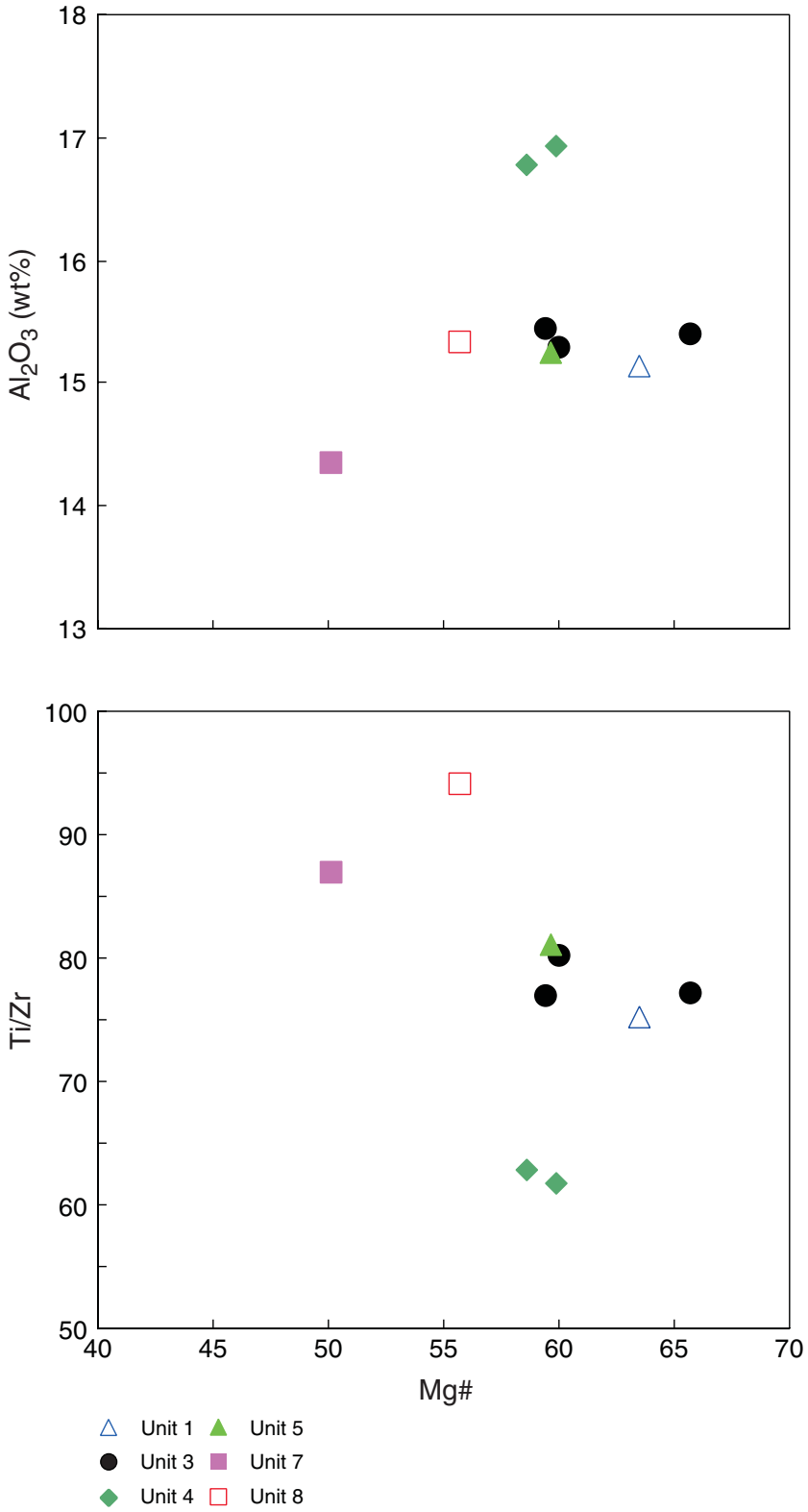

Figure F22. Abundance ratios of Zr/Y and Ba/Sr vs. Ti/Zr used to distinguish between tholeiitic and alkalic basalt. These ratios are sensitive to the presence of metasomatic component in the basaltic mantle source.

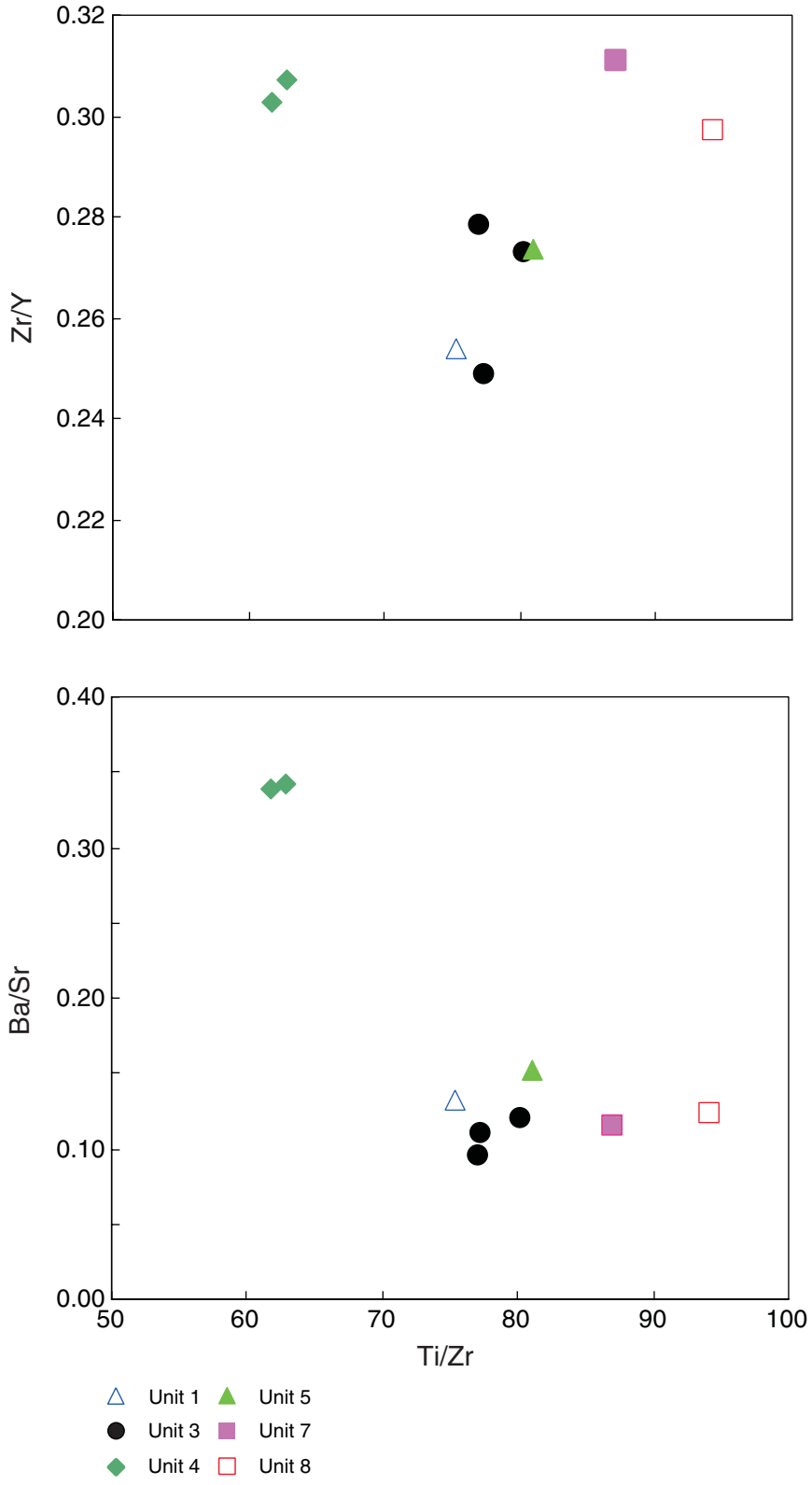

Figure F23. Incompatible trace element pattern for Site 1243 tholeiitic and alkalic basalt. Primitive mantle-normalized values of Sun and McDonough (1989). Alkali basalt of Unit 4 are enriched in incompatible elements.

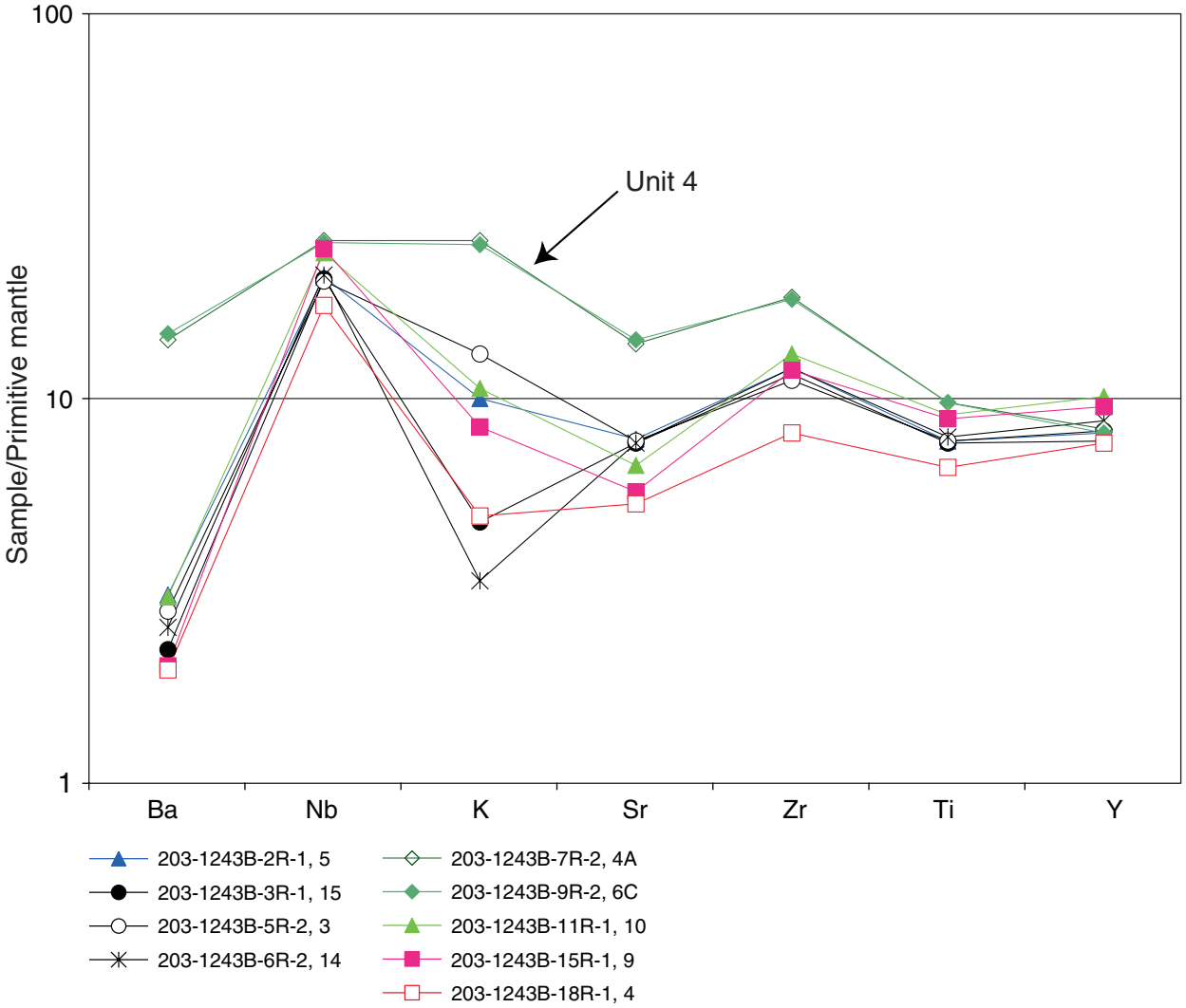

Figure F24. Main alteration features in Units 1, 3, and 7. **A.** Sample **203-1243B-5R-2, 29–32 cm** (PPL; field of view = 2.75 mm; photomicrograph 1243B-27). **B.** Sample **203-1243B-5R-2, 29–32 cm** (XPL; field of view = 2.75 mm; photomicrograph 1243B-32). **C.** Sample **203-1243B-6R-2, 105–109 cm** (PPL; field of view = 2.75 mm; photomicrograph 1243B-19).

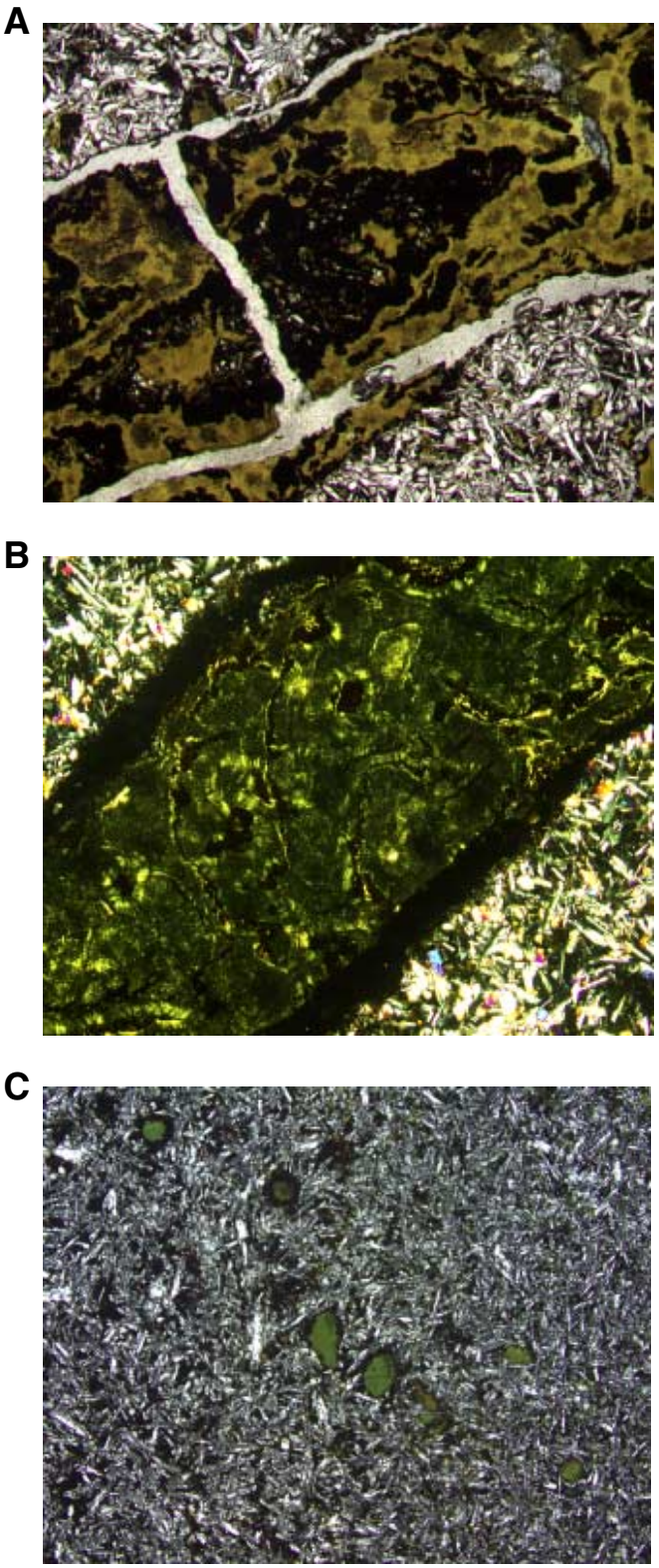

Figure F25. Main alteration feature in Units 4, 5, and 6. **A.** Sample **203-1243B-8R-2, 25–29 cm** (PPL; field of view = 2.75 mm; photomicrograph 1243B-15). **B.** Sample **203-1243B-7R-3, 20–23 cm** (PPL; field of view = 2.75 mm; photomicrograph 1243B-24). **C.** Sample **203-1243B-9R-2, 138–141 cm** (PPL; field of view = 2.75 mm; photomicrograph 1243B-34).

A

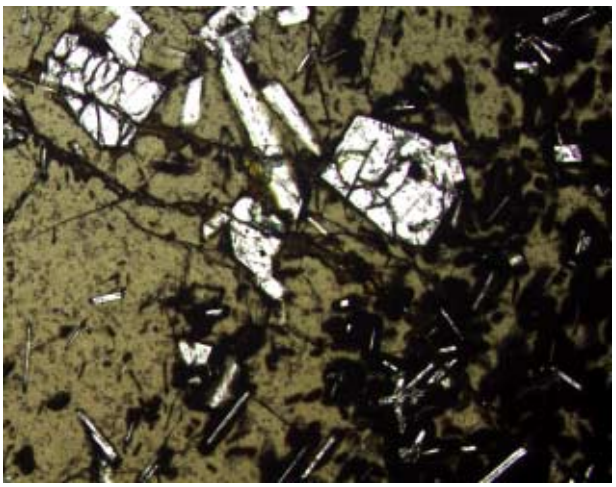

B

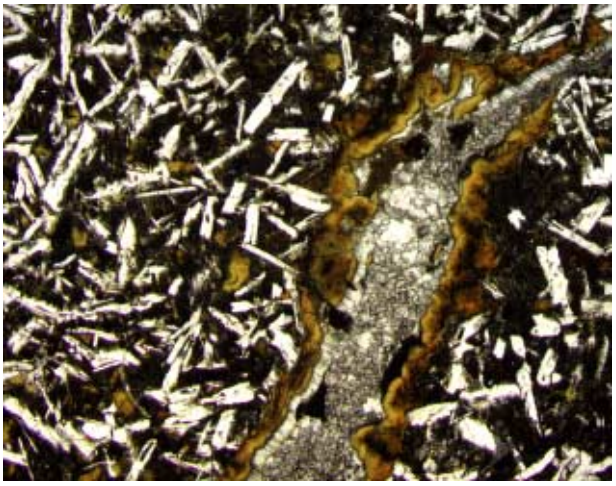

C

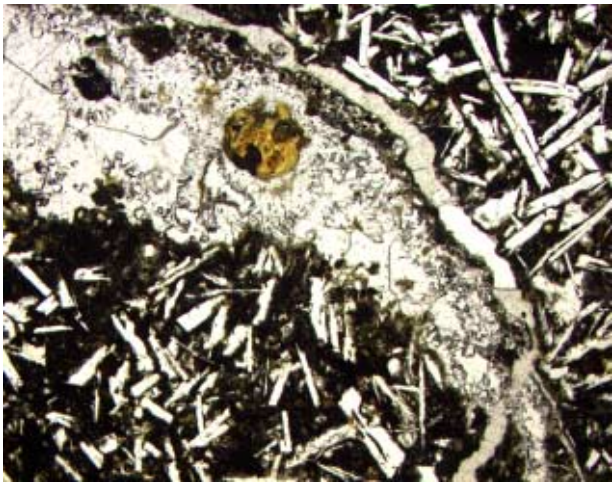

Figure F26. Loss on ignition (LOI) vs. depth in Hole 1243B samples.

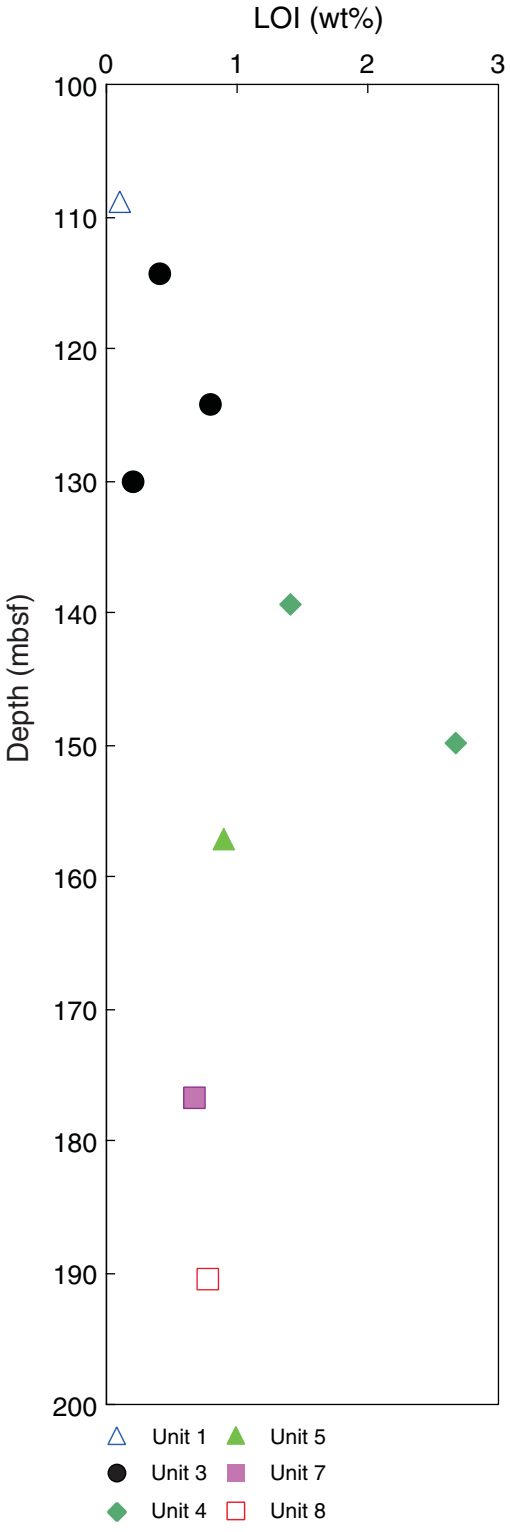

Figure F27. Downhole variations in (**A**) natural remanent magnetization (NRM) intensity and (**B**) inclination without demagnetization (black curve) and after 25-mT demagnetization (red curve) in cores from Hole 1243B. (Continued on next page.)

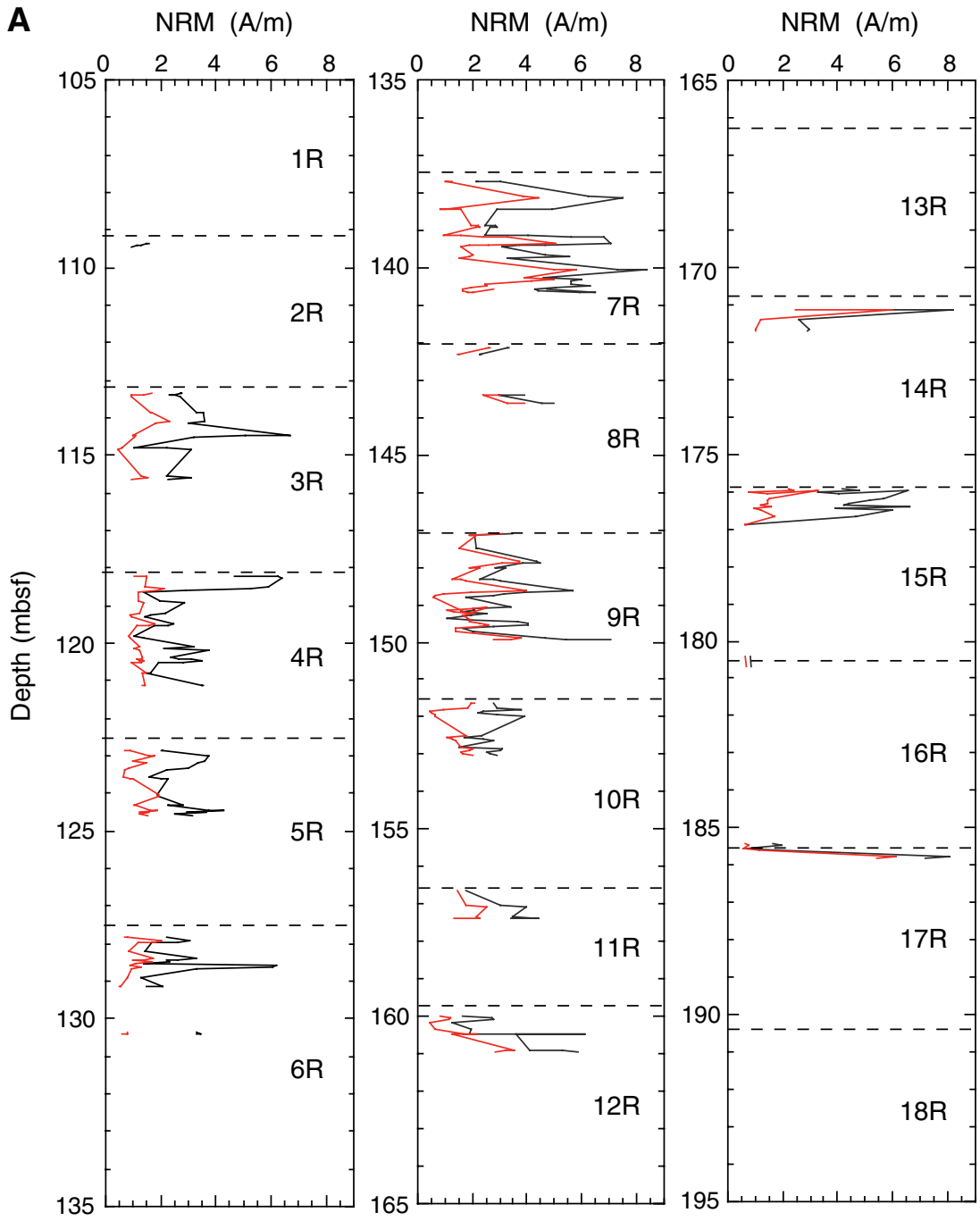

Figure F27 (continued).

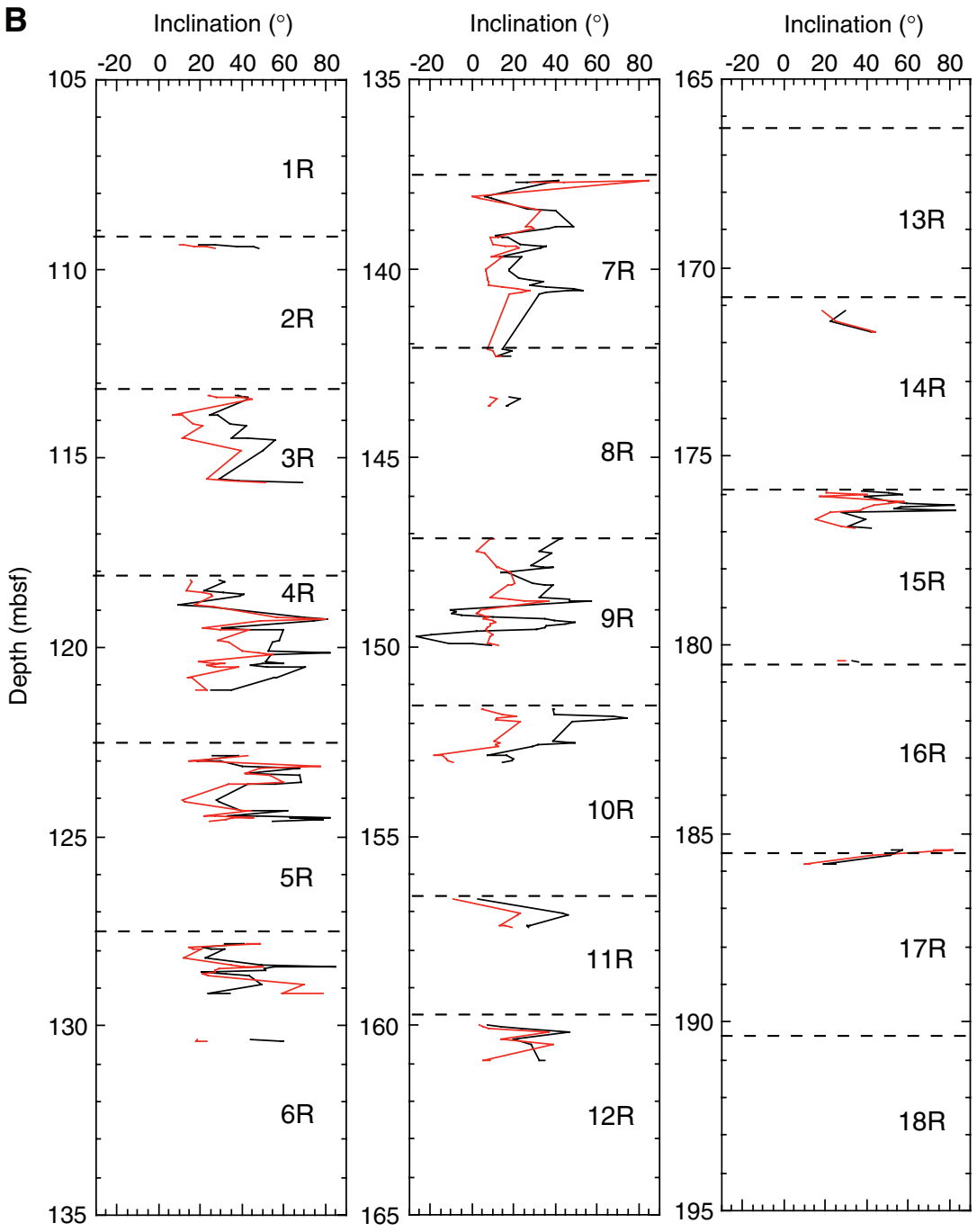

Figure F28. Downhole plot of ChRM inclinations for both pass-through long-core (red) and discrete (blue) sample measurements in cores from Hole 1243B.

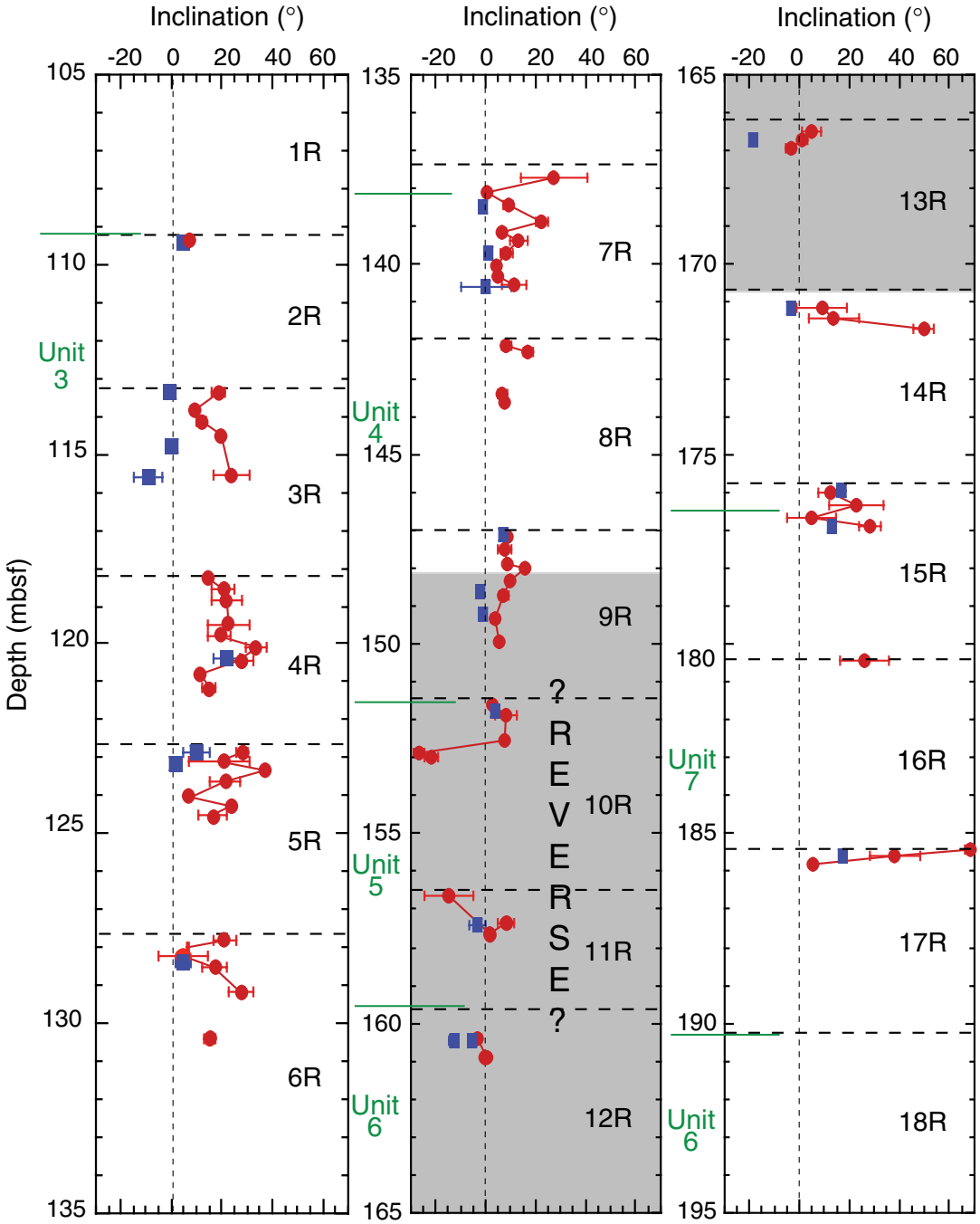

Figure F29. Downhole variation in mean characteristic remanent magnetization (ChRM) intensity, declination, and inclination for Section 203-1243B-9R-2. Circles = archive-half core, squares = discrete sample measurements. Note that discrete samples were taken on the working-half core.

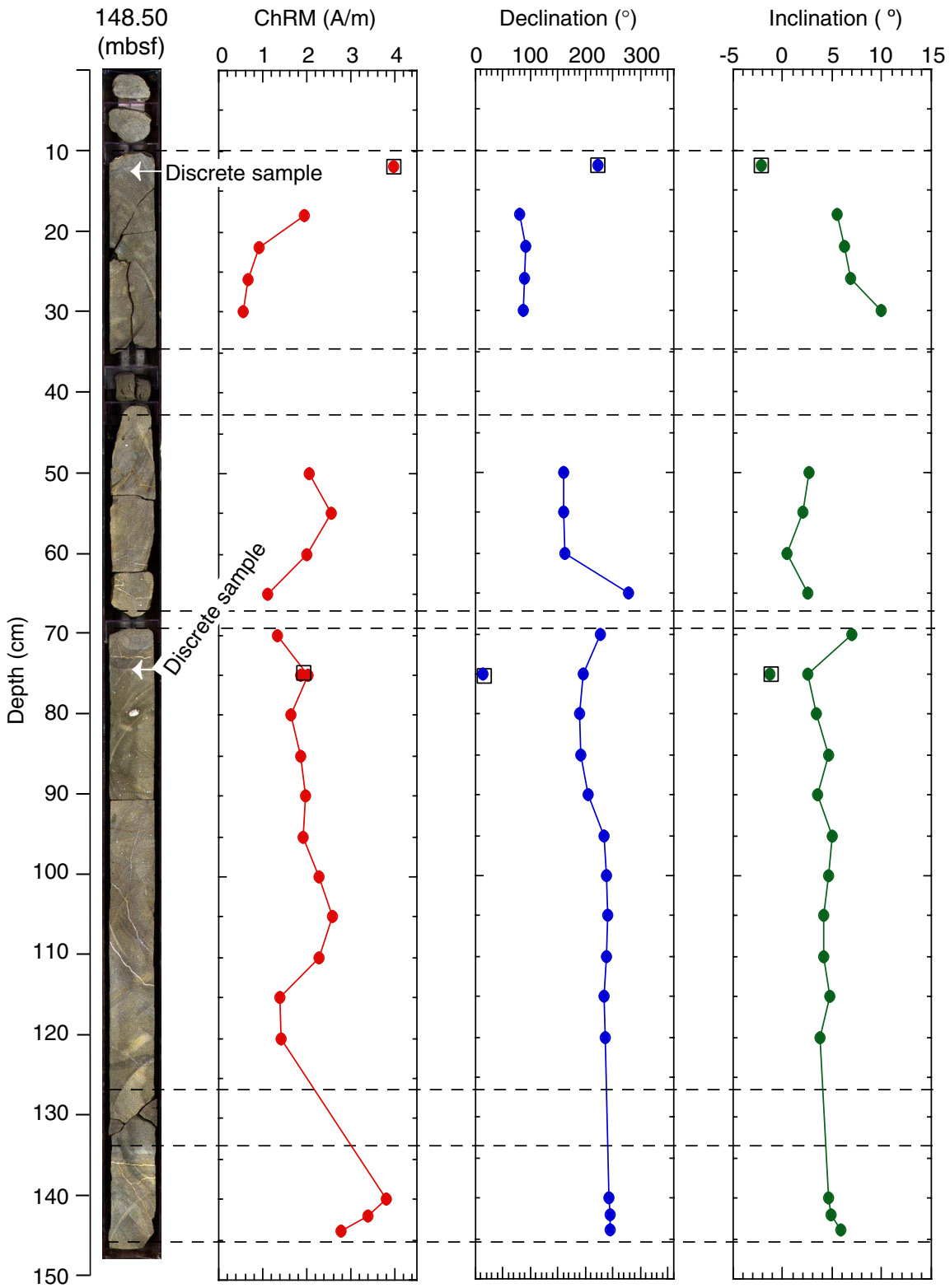

Figure F30. Representative vector endpoint diagrams showing the results of (**A**) thermal and (**B**) AF demagnetization for the two halves of the discrete sample from Section 203-1243B-9R-2, 12 cm. Also shown are examples of (**C**) good-quality AF demagnetization for discrete Sample 203-1243B-7R-1, 106–108 cm, and (**D**) typical archive-half core AF behavior measurements (Section 203-1243B-8R-1, 14 cm). Vector endpoints are projected onto the vertical (open squares) and horizontal (solid squares) planes, respectively.

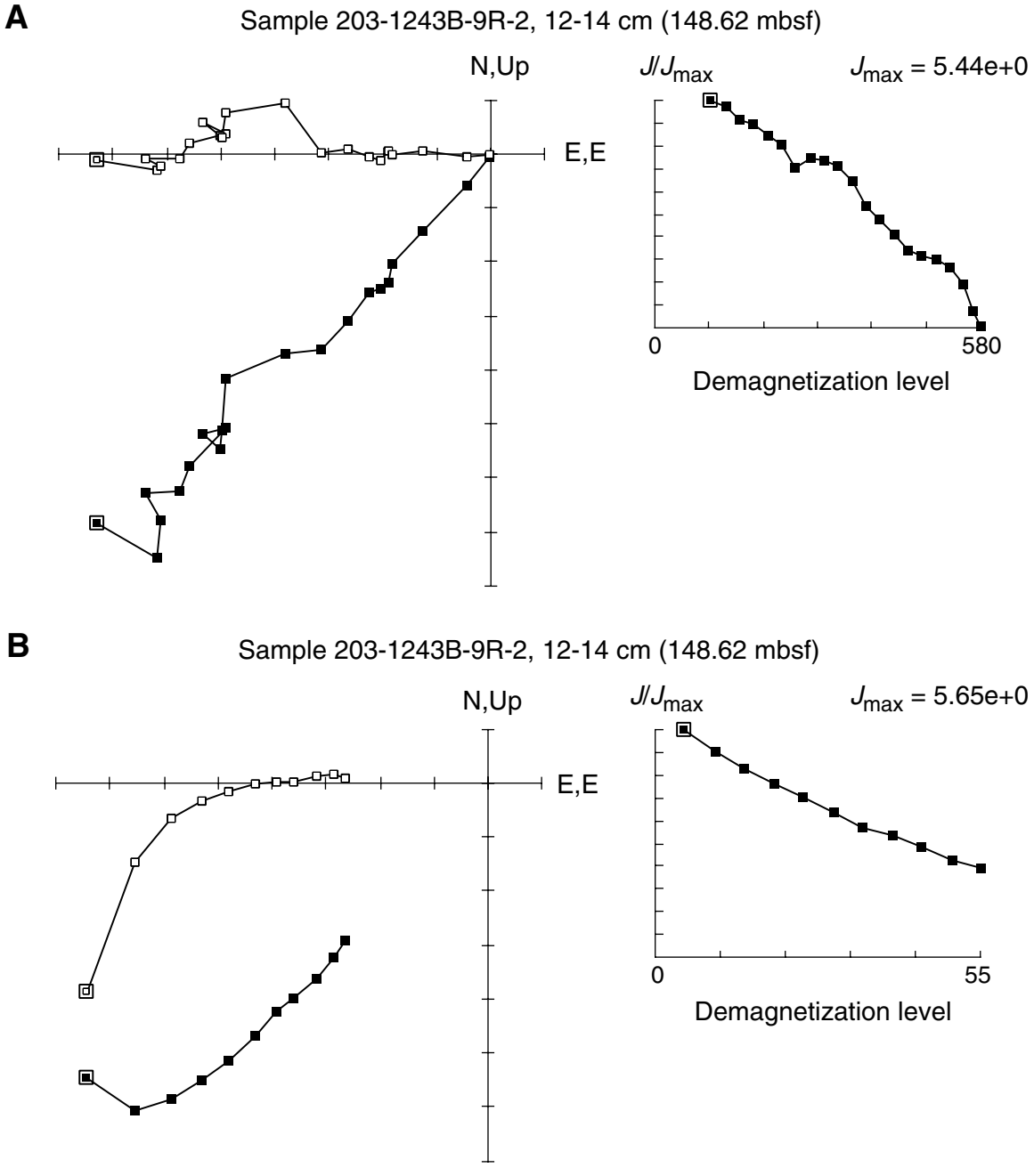

Figure F31. (**A**) Isothermal remanent magnetization (IRM) acquisition and (**B**) thermal demagnetization of the IRM on several representative discrete samples. Saturation of isothermal remanent magnetization acquisition is consistent with a fine-grained magnetite, perhaps with a single-domain component (e.g., Dunlop and Ozdemir, 1997).

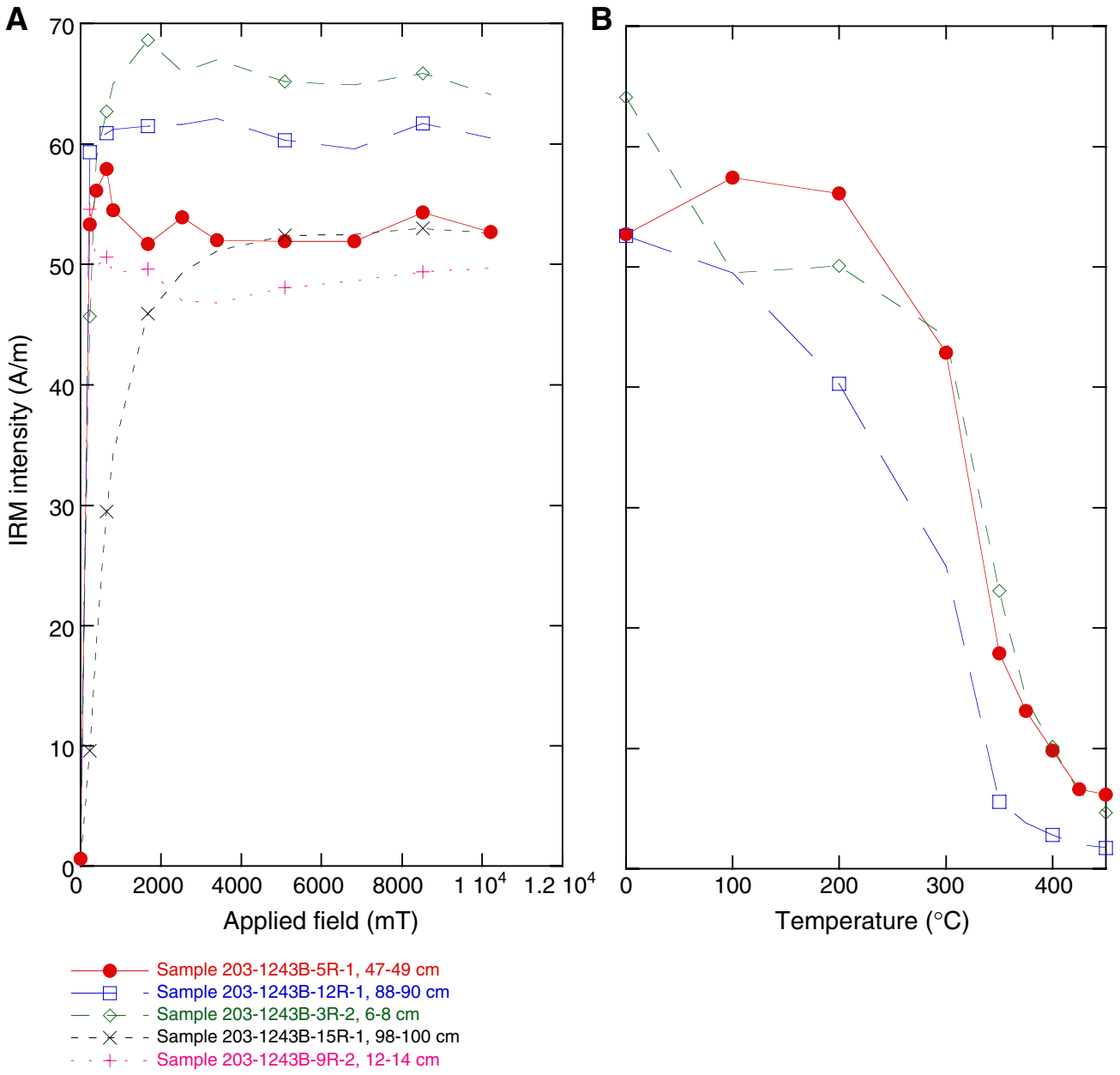

Figure F32. Overprint vs. sample position within a pillow. Vector endpoint diagrams showing the results of AF demagnetization for two closely spaced discrete samples from Section 203-1243B-12R-1. **A.** Sample 203-1243B-12R-1, 85–87 cm. **B.** Sample 203-1243B-12R-1, 88–90 cm. The characteristic remanent magnetization component is shown by a straight blue line fitting the data points. The primary component is more difficult to extract for Sample 203-1243B-12R-1, 88–90 cm (see **"Alternating-Field and Thermal Demagnetization of Discrete Samples,"** p. 18, in "Paleomagnetism").

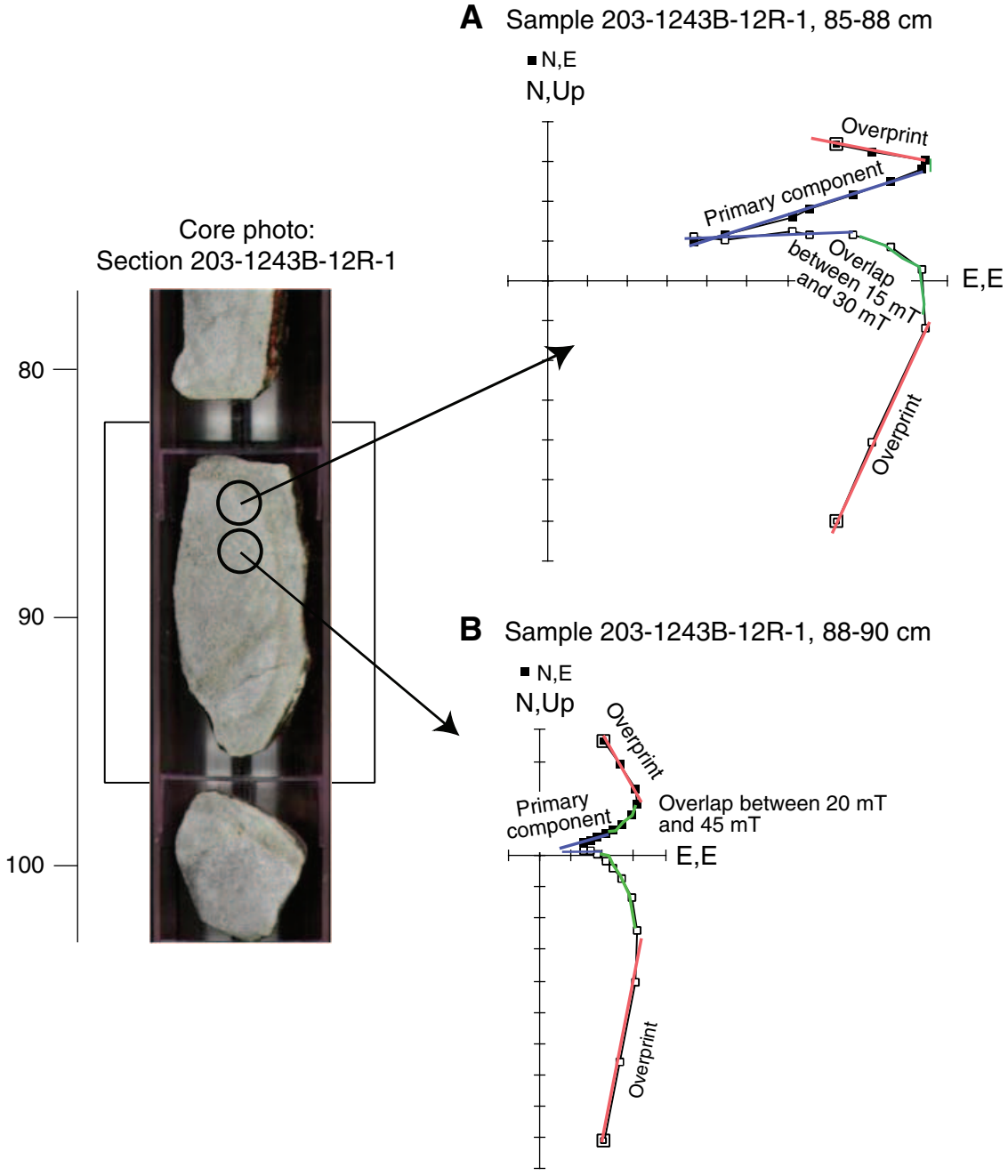

Figure F33. MS vs. depth at Hole 1243B. (**A**) Whole-core measurements at 2-cm intervals using the multisensor track and (**B**) archive-half measurements at 1-cm intervals using the archive multisensor track.

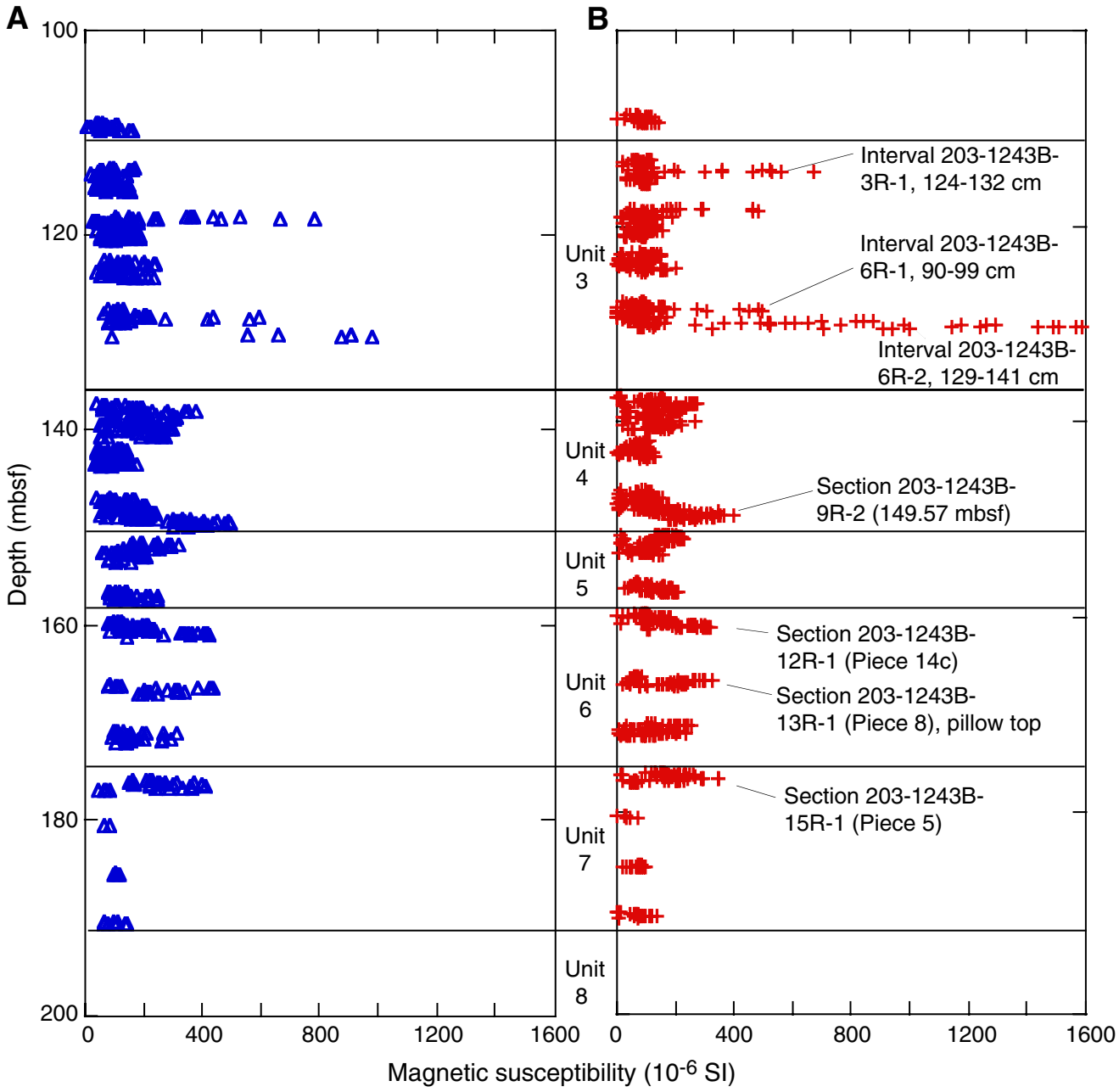

Figure F34. Physical properties of basalt samples recovered from Hole 1243B. **A.** Wet bulk density vs. porosity. **B.** Porosity vs. grain density **C.** Wet bulk density vs. grain density. **D.** Sonic velocity vs. wet bulk density. **E.** Sonic velocity vs. porosity. **F.** Sonic velocity vs. grain density.

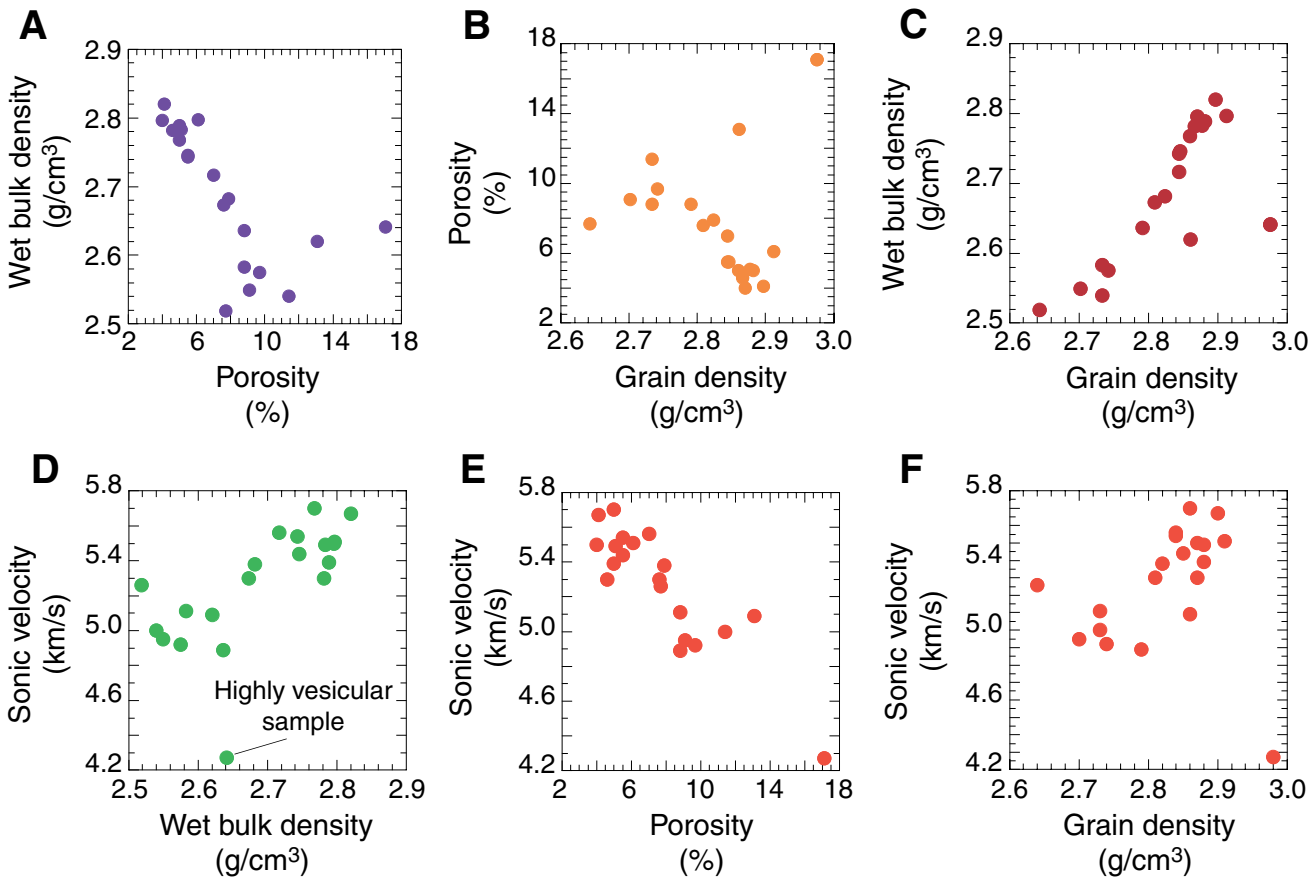

Figure F35. Porosities and measured sonic velocities in basalt samples recovered from Hole 1243B, plotted with the downhole sonic log and interval velocities computed from the Well Seismic Tool (WST) survey. Also shown is the lithostratigraphy column. Log and WST depths have been adjusted to the coring depths. s.e. = standard error.

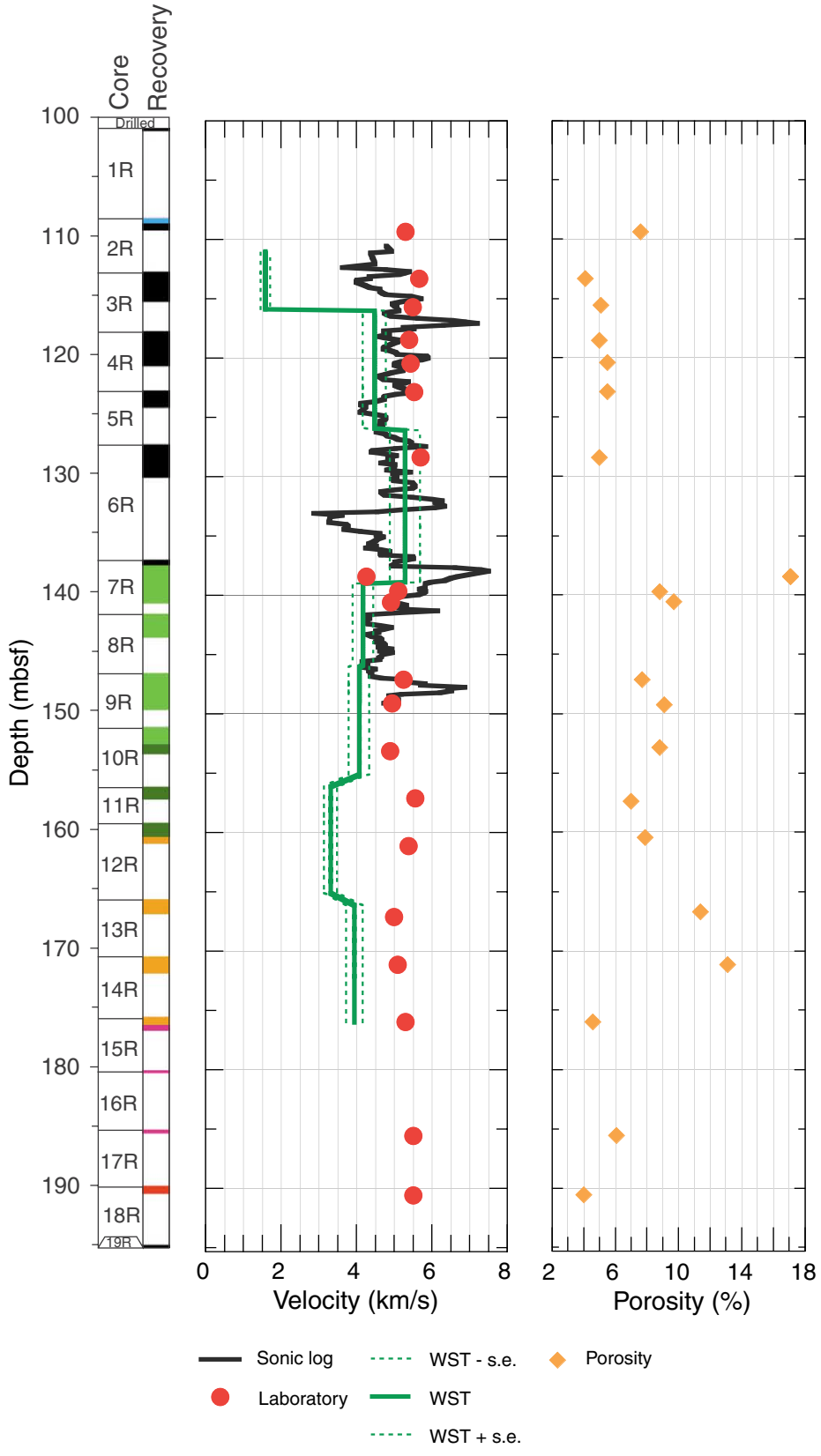

Figure F36. Full waveform images from the DSI sonic tool, covering a depth interval of 3835–3891 mbrf in Hole 1243B. gAPI = American Petroleum Institute gamma ray units.

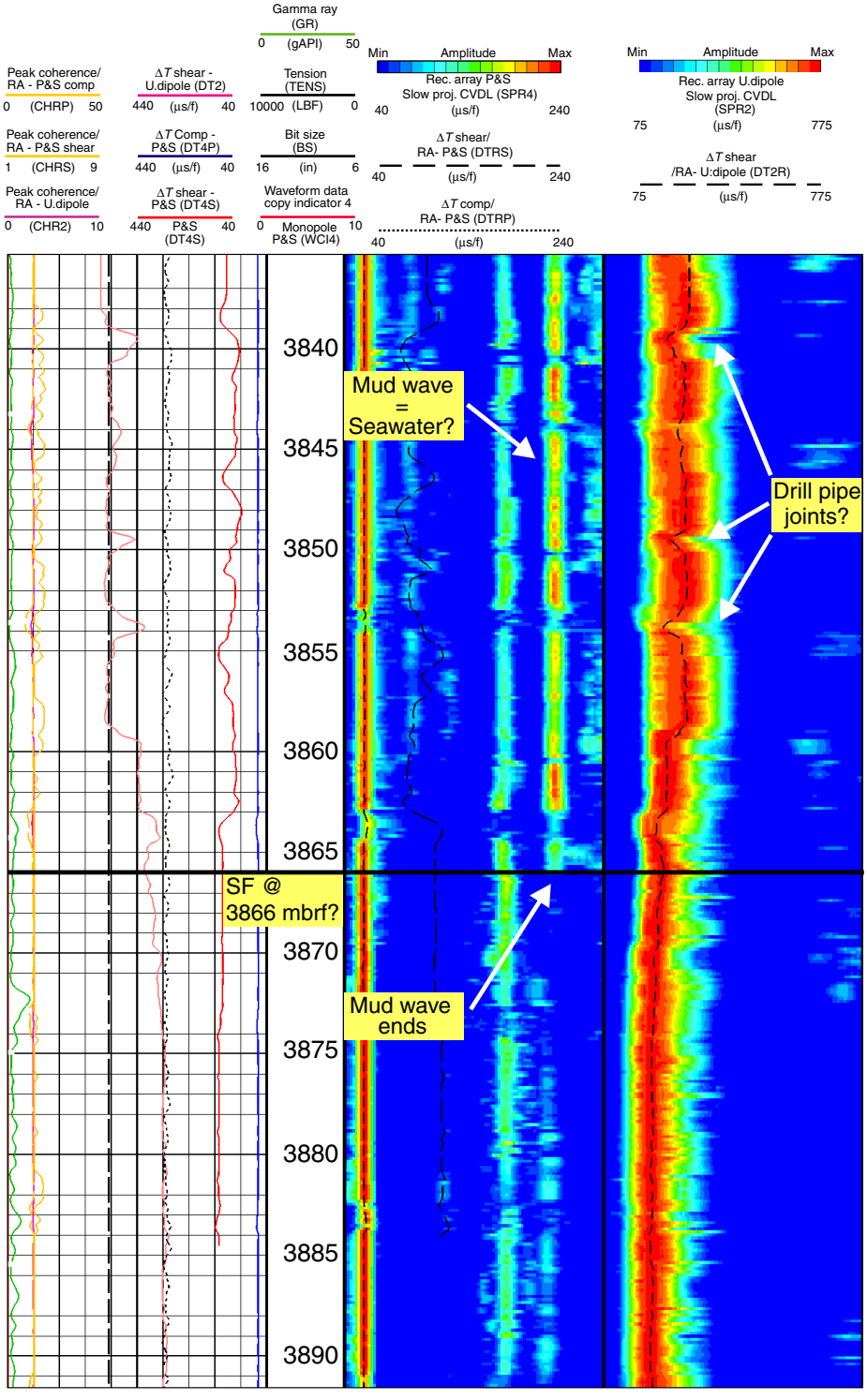

Figure F37. Full waveform images from the CBT, covering a depth interval of 4023–4088 mbrf, at Hole 1243A. The CBT records amplitudes as well as transit times in 3-ft casing bond log (CBL) and 5-ft (VDL) spacings. gAPI = American Petroleum Institute gamma ray units, BOH = bottom of hole.

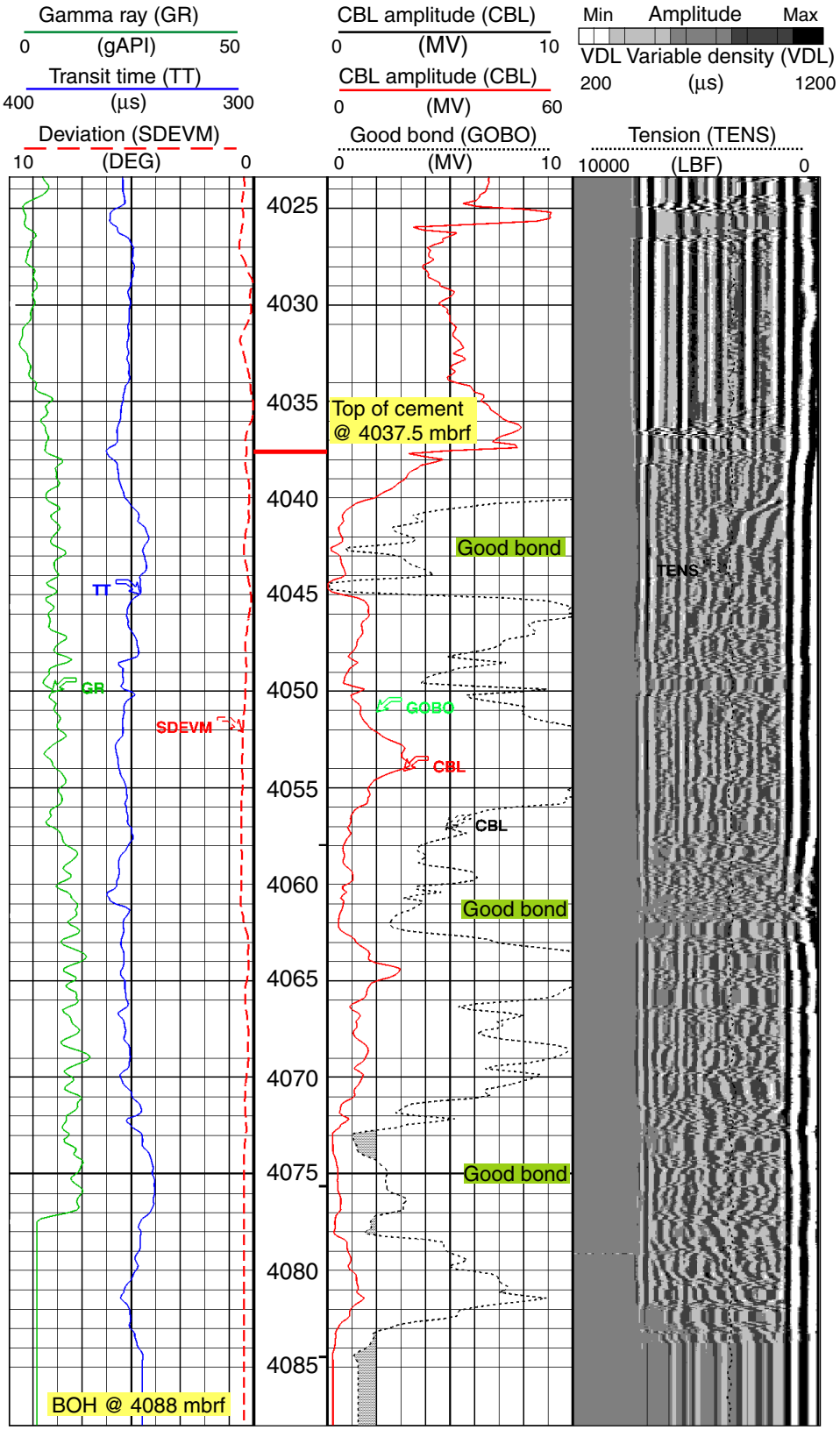

Figure F38. Composite plot of downhole measurements in the sediment and basement section in Hole 1243B. The core lithology has been shifted 6.3 m down to match the log-derived depths. gAPI = American Petroleum Institute gamma ray units, IDPH = deep induction phasor-processed resistivity, IMPH = medium induction phasor-processed resistivity, SFLU = spherically focused resistivity measurement, DTCO = ΔT *P*-wave, DTSM = ΔT *S*-wave.

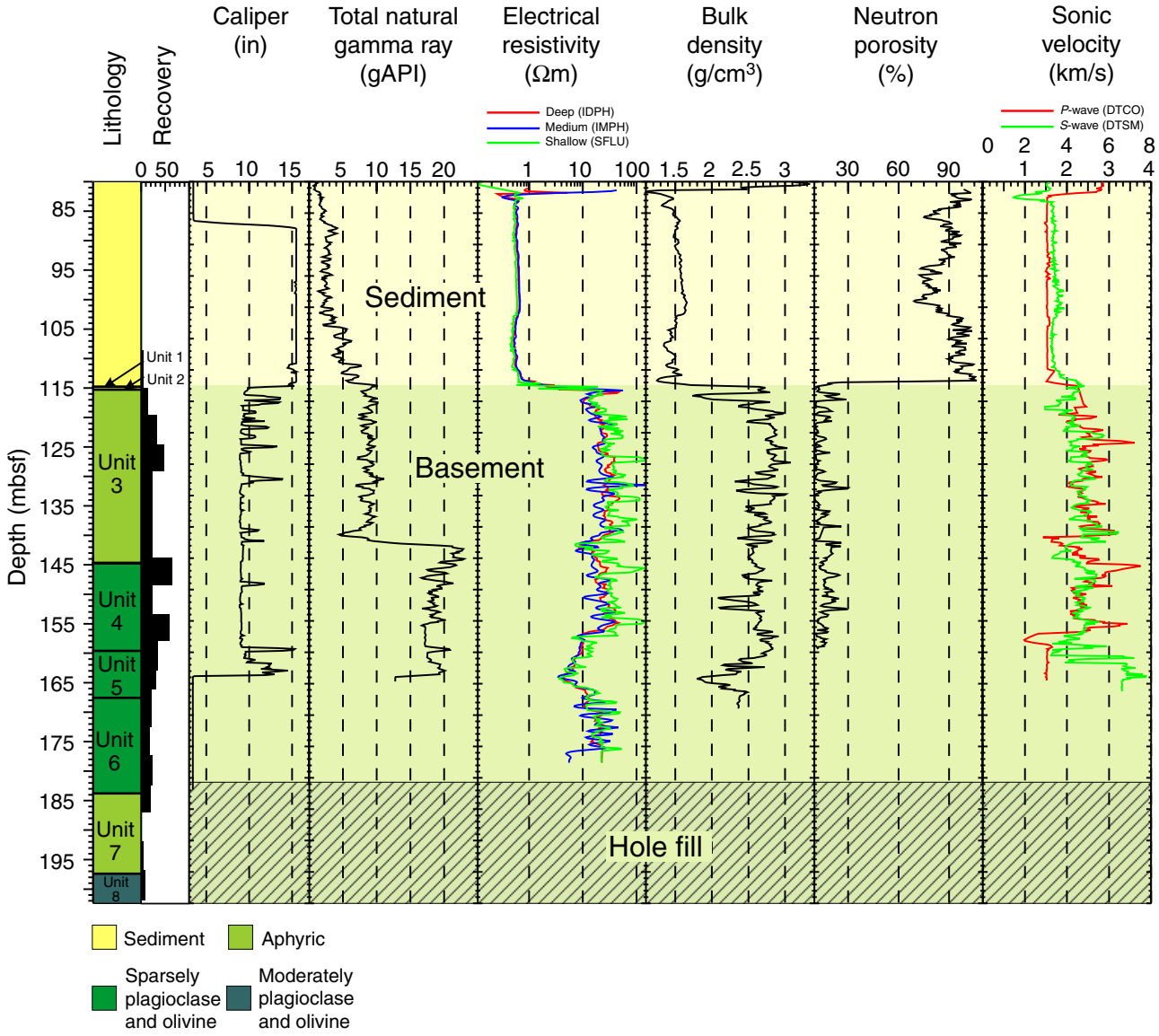

Figure F39. Scatter plots of a selection of downhole measurements in Hole 1243B. gAPI = American Petroleum Institute gamma ray units.

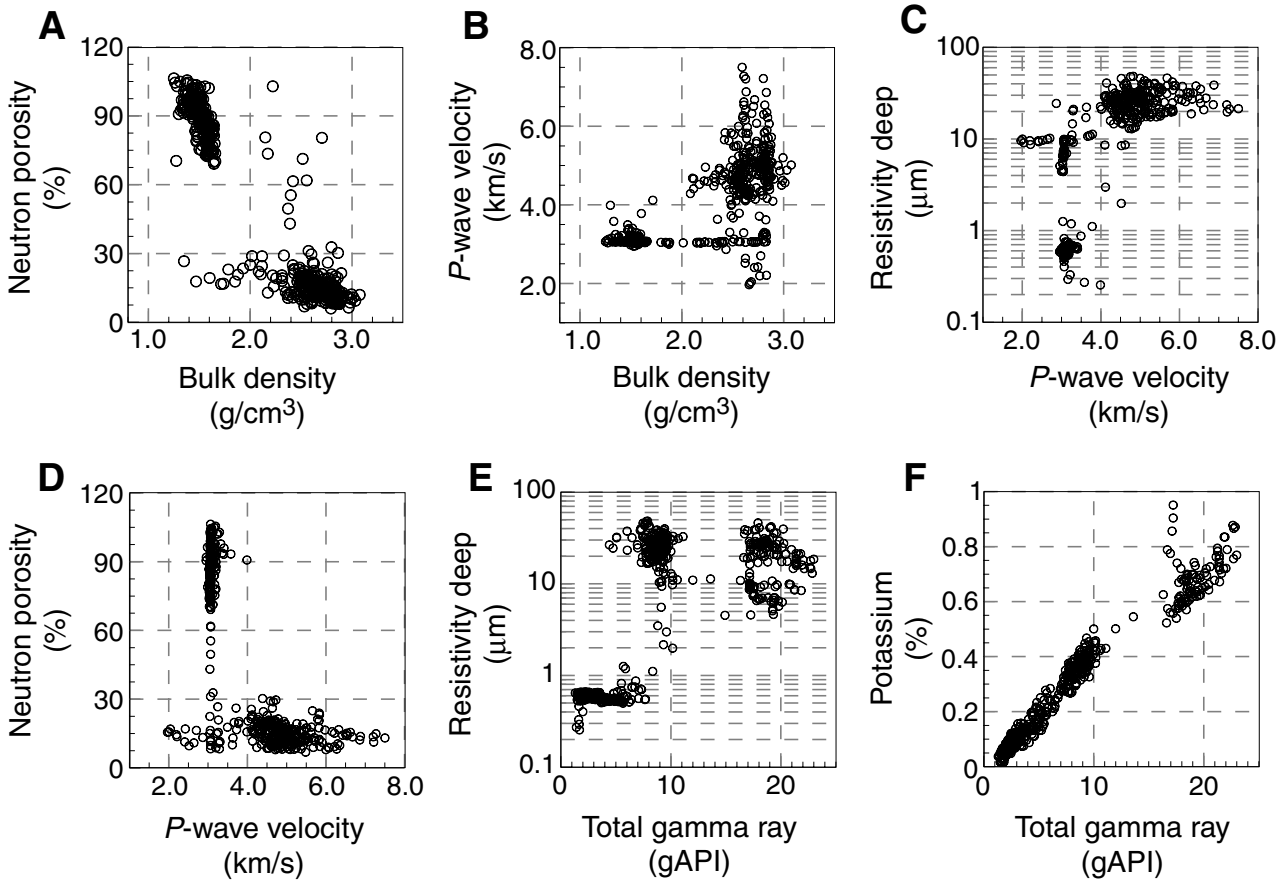

Figure F40. Full waveform images from the DSI, covering a depth interval of 3965–4021 mbrf in Hole 1243B. gAPI = American Petroleum Institute gamma ray units.

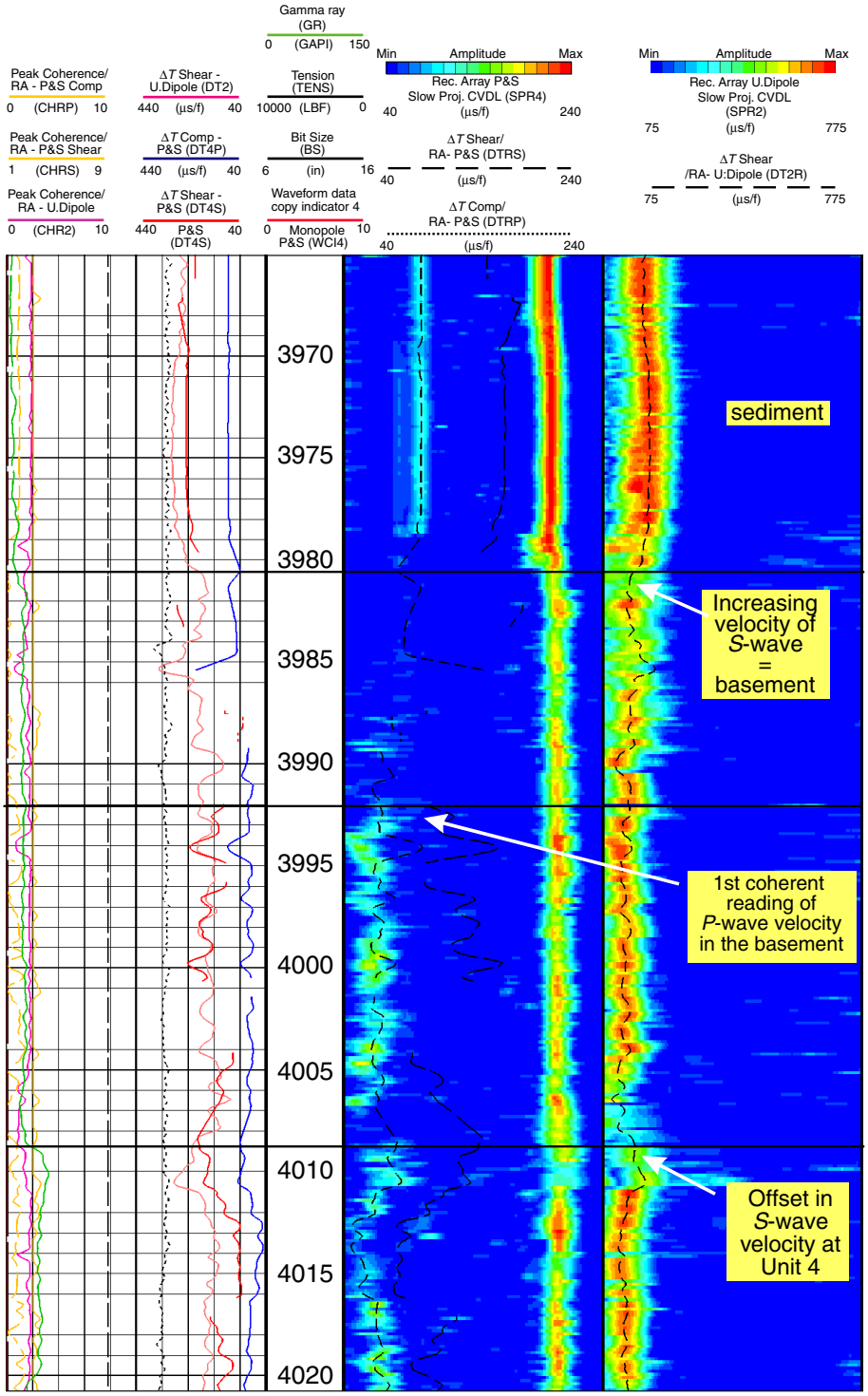

Figure F41. FMS image displaying the sediment–basement transition at 113.7 mbsf and the intercalated sediment layer (lithologic Unit 2).

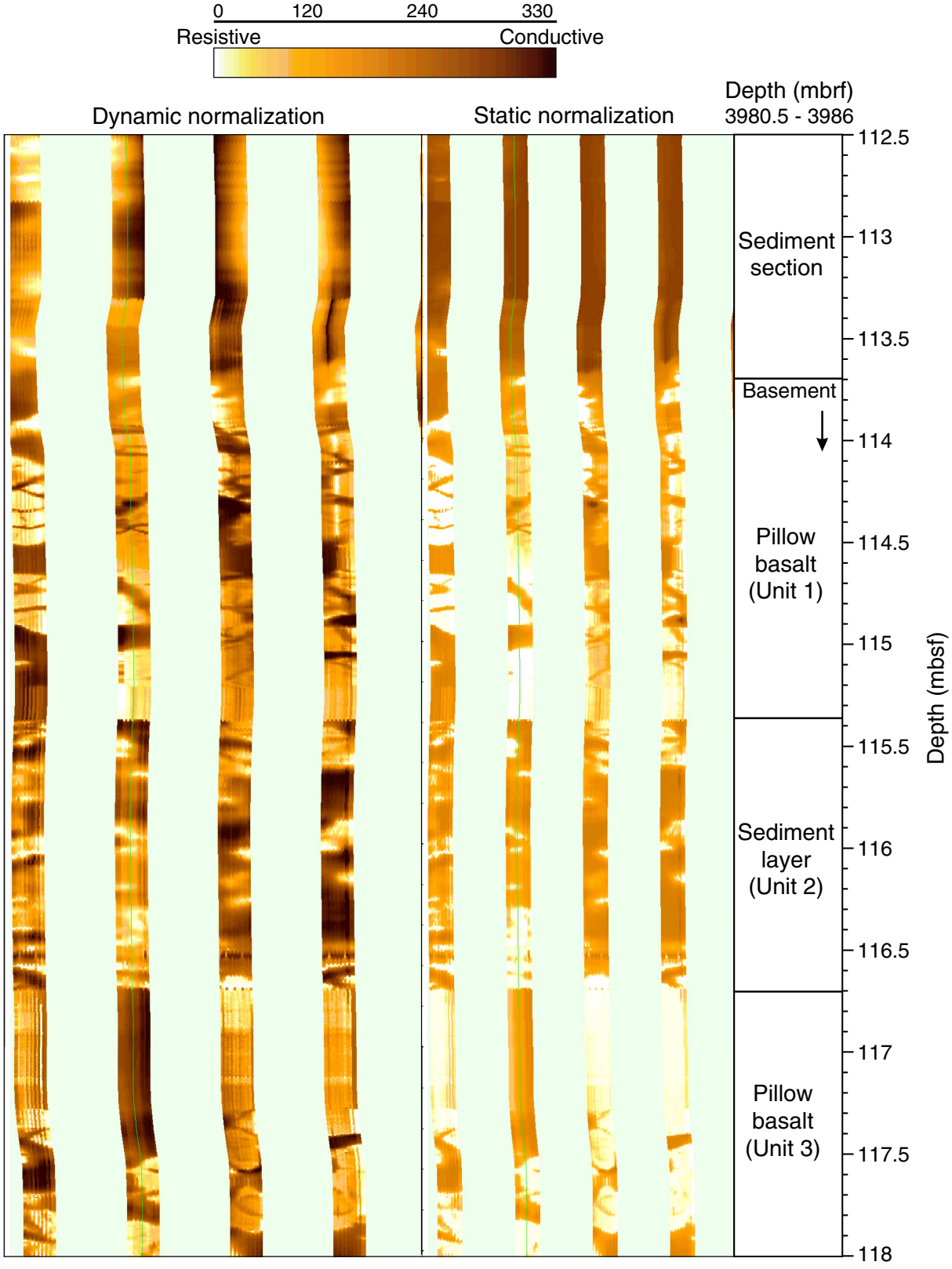

Figure F42. Composite plot of downhole measurements in comparison with petrophysical core measurements (see **"Physical Properties,"** p. 20) in the basement section in Hole 1243B. gAPI = American Petroleum Institute gamma ray units, IDPH = deep induction phasor-processed resistivity, IMPH = medium induction phasor-processed resistivity, SFLU = spherically focused resistivity measurement, DTCO = ΔT *P*-wave, DTSM = ΔT *S*-wave.

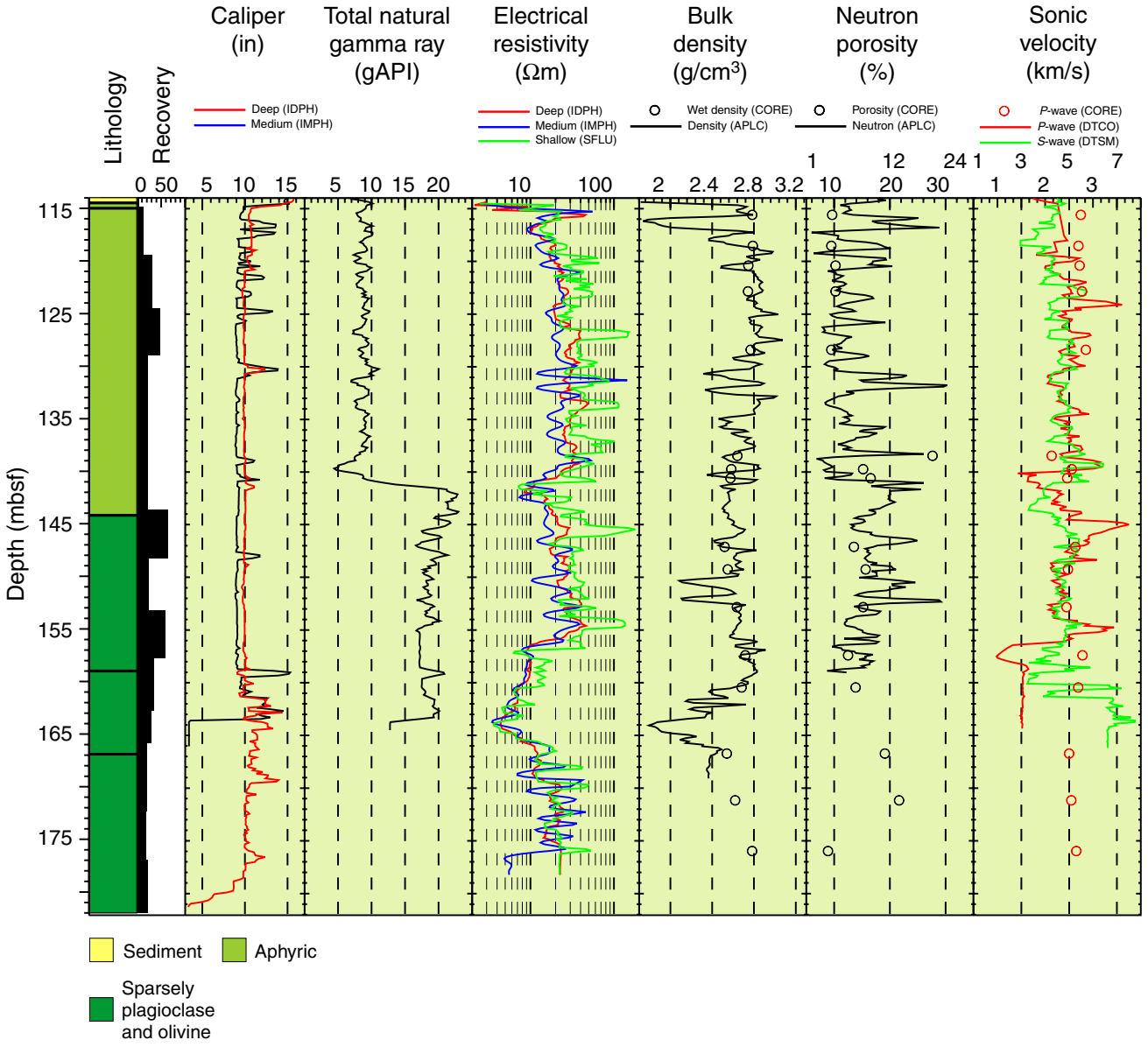

Figure F43. FMS image displaying a succession of pillow basalts. The transition between lithologic Unit 3 and 4 formations can be observed at a depth of 140.8 mbsf.

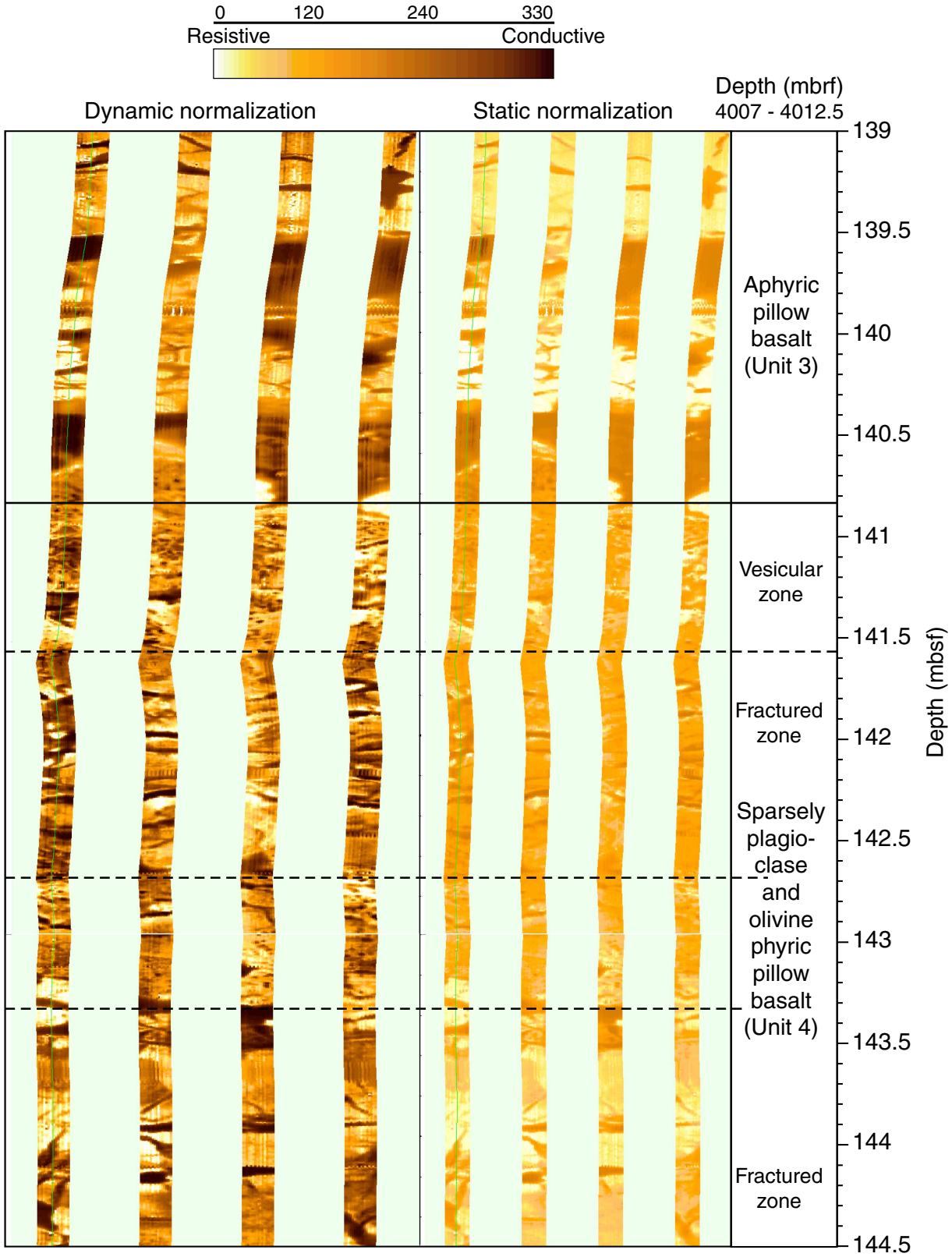

Figure F44. Gamma ray response in comparison to potassium, thorium, and uranium readings in the basement section. The increase in gamma ray at 141.5 mbsf can be related to a unit change. gAPI = American Petroleum Institute gamma ray units.

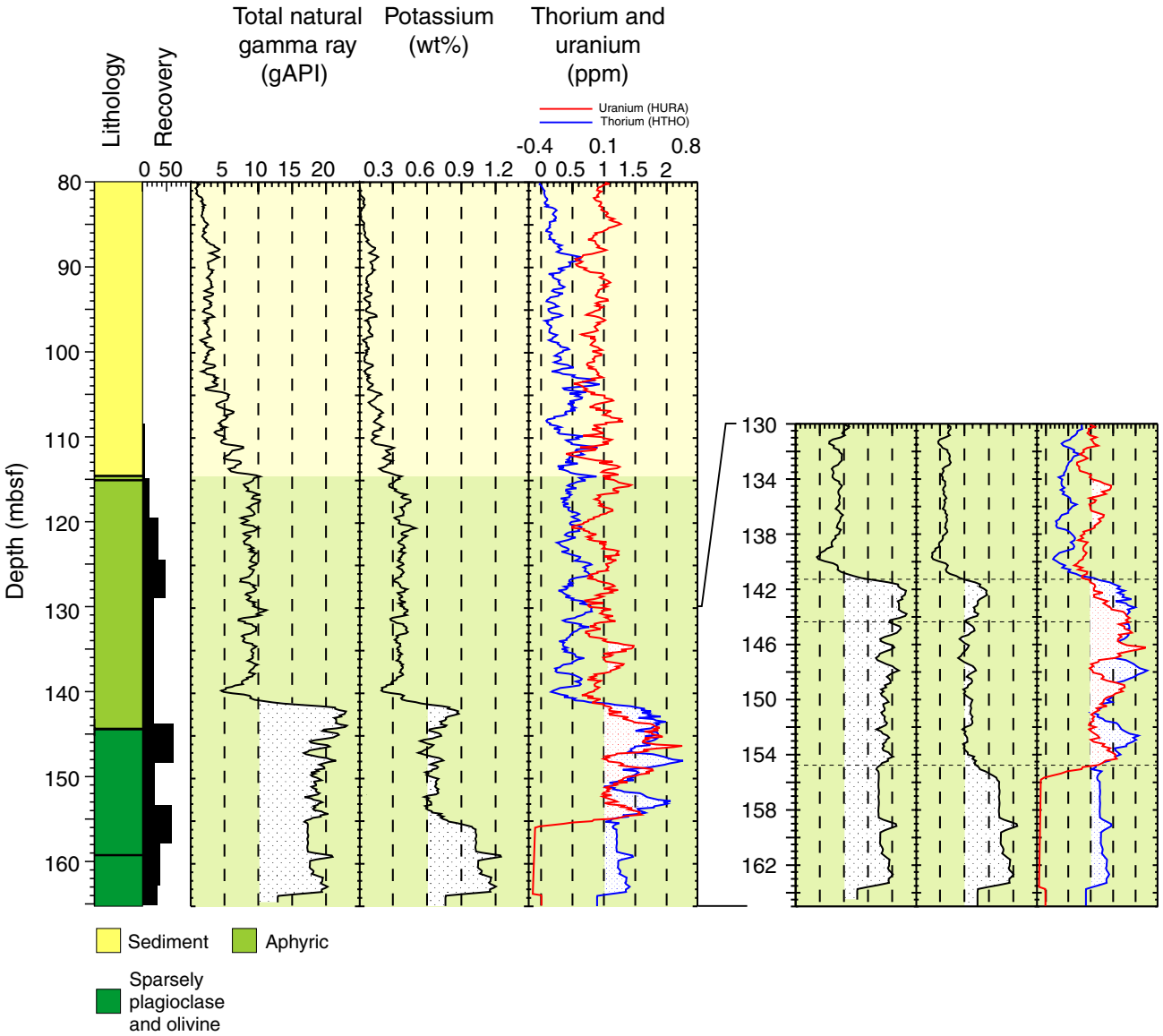

Table T1. Coring summary, Site 1243.

Hole 1243A
Latitude: 5°18.0541′N
Longitude: 110°4.5798′W
Time on site (hr): 349.25 (0600 hr, 11 Jun–1530 hr, 25 Jun 2002)
Survey time (hr): 6.0 (0000 hr, 11 Jun–0600 hr, 11 Jun 2002)
Time on Trip #1 (hr): 210.5 (0600 hr, 11 Jun–0030 hr, 20 Jun 2002)
Time on Trip #2 (hr): 20.58 (1855 hr, 24 Jun–1530 hr, 25 Jun 2002)
Total time on Hole 1243A (hr): 237.08
Seafloor (drill pipe measurement from rig floor, mbrf): 3882.4
Distance between rig floor and sea level (m): 11.1
Water depth (drill pipe measurement from sea level, m): 3871.3
Total depth (drill pipe measurement from rig floor, mbrf): 4094.4
Total penetration (meters below seafloor, mbsf): 224.0
Total length of cored section (m): 0.0
Total length of drilled intervals (m): 224.0
Total core recovered (m): 0.0
Core recovery (%): NA
Total number of cores: 0
Total number of drilled intervals: 3
Comments: Hole 1243A was drilled, cased, and cemented for the future implacement of seismic instrument. No coring was done in this hole.

Hole 1243B
Latitude: 5°18.0543′N
Longitude: 110°4.2544′W
Time on hole (hr): 112.17 (0030 hr, 20 Jun–1855 hr, 24 Jun 2002)
Seafloor (drill pipe measurement from rig floor, mbrf): 3868.0
Distance between rig floor and sea level (m): 11.4
Water depth (drill pipe measurement from sea level, m): 3856.6
Total depth (dill pipe measurement from rig floor, mbrf): 4063.3
Total penetration (meters below seafloor, mbsf): 195.3
Total length of cored section (m): 93.3
Total length of drilled intervals (m): 102.0
Total core recovered (m): 28.17
Core recovery (%): 30.2
Total number of cores: 19
Total number of drilled intervals: 1

Core	Date (Jun 2002)	Local time (hr)	Depth (mbsf) Top	Depth (mbsf) Bottom	Length (m) Cored	Length (m) Recovered	Recovery (%)	Comments
203-1243A-								
	12		*****Drilled from 0.0 to 48.0 mbsf *****					Jet in 20-in casing string at 4 joints ±48 m on 0800–1800, 12 June 2002.
	17	1745	*****Drilled from 48.0 to 134.0 mbsf *****					1200 hr, 13 June–0745 hr, 14 June 2002
	17	2000	*****Drilled from 0.0 to 102.0 mbsf *****					0600 hr, 16 June–2000 hr, 17 June 2002
			Drilled total:		224.0			
203-1243B-								
			*****Drilled from 0.0 to 102.0 mbsf *****					
1R	20	0915	102.0	108.6	6.6	0.26	3.9	
2R	20	1130	108.6	113.2	4.6	0.61	13.3	
3R	20	1515	113.2	118.2	5.0	1.59	31.8	
4R	20	1955	118.2	122.7	4.5	2.15	47.8	
5R	21	0045	122.7	127.7	5.0	1.54	30.8	
6R	21	0555	127.7	137.4	9.7	2.22	22.9	
7R	21	1030	137.4	142.0	4.6	2.93	63.7	
8R	21	1425	142.0	147.0	5.0	1.20	24.0	
9R	21	1805	147.0	151.5	4.5	2.67	59.3	
10R	21	2125	151.5	156.5	5.0	1.77	35.4	
11R	22	0130	156.5	159.6	3.1	0.94	30.3	
12R	22	0515	159.6	166.1	6.5	1.37	21.1	
13R	22	1000	166.1	170.8	4.7	0.86	18.3	
14R	22	1240	170.8	175.9	5.1	1.15	22.6	
15R	22	1625	175.9	180.4	4.5	0.86	19.1	
16R	22	1950	180.4	185.4	5.0	0.08	1.6	
17R	23	0255	185.4	190.2	4.8	0.21	4.4	
18R	23	0620	190.2	195.2	5.0	0.46	9.2	
19B	23	0900	195.2	195.3	0.1	5.3*	5300.0	
				Cored totals:	93.3	28.17	30.2	
				Drilled total:	102.0			
				Total:	195.3			

Note: * = Core 203-1243B-19B, which is composed entirely of cuttings and cavings from higher in the hole.

Table T2. Basement unit characteristics defined, Hole 1243B.

Lithologic unit	Rock name	Upper contact (core, section, piece)	Lower contact (core, section, piece)	Interval (mbsf)
		203-1243B-	203-1243B-	
1	Aphyric basalt	2R-1, 1	2R-1, 8	108.60–109.05
2	Limestone	2R-1, 9	2R-1, 9	109.05–109.12
3	Aphyric basalt	2R-1, 10	7R-1, 7	109.12–137.90
4	Sparsely plagioclase and olivine phyric basalt	7R-1, 8	10R-1, 16	137.90–152.69
5	Sparsely plagioclase and olivine phyric basalt	10R-1, 17	12R-1, 12	152.69–160.63
6	Sparsely plagioclase and olivine phyric basalt	12R-1, 13	15R-1, 8B	160.63–176.74
7	Aphyric basalt	15R-1, 9	17R-1, 2	176.74–185.62
8	Moderately plagioclase and olivine phyric basalt	18R-1, 1	18R-1, 9	185.62–195.30

Note: This table is also available in **ASCII.**

Table T3. Mineral assemblage and proportions described in thin sections, Hole 1243B.

Thin section	Core, section, interval (cm)	Unit	Phenocryst		Groundmass					
			Olivine	Plagioclase	Olivine	Plagioclase	Clinopyroxene	Magnetite	Ilmenite	Glass
	203-1243B-									
1	2R-1 (Piece 5, 23–25)	1				xxxxxx	xxx	x		
2	2R-1 (Piece 9, 47–49)	3								
3	3R-1 (Piece 15, 114–117)	3	+			xxxxxx	xxx	x		
4	3R-1 (Piece 16B, 130–134)	3				xxxxxx	x	x		x
6	5R-2 (Piece 3, 11–14)	3				xxxx	xxxx	x		x
5	5R-2 (Piece 5, 29–32)	3				xxx	xxx	x		x
7	6R-2 (Piece 14, 105–109)	3				xxxxxx	xx	x		x
8	7R-1 (Piece 11, 75–78)	4				xxx	xx	+		x
9	7R-1 (Piece 12, 81–84)	4		+		xxxxxx	x	+		x
10	7R-2 (Piece 4A, 55–57)	4	+	+		xxxxxxx	x	+		x
11	7R-2 (Piece 5, 74–77)	4	+	+		xxxxxx	+	+		xx
12	7R-3 (Piece 2, 20–23)	4	+	+		xxxxxx	+	+		x
13	8R-2 (Piece 4, 25–29)	4	++	+++++		xxxx	+	x		xx
14	9R-2 (Piece 6C, 138–141)	4	+++	+++++	+	xxxxx	xxxx	x		x
15	10R-1 (Piece 3, 14–17)	4		+	+	xxxxx	xxx	+	+	x
16	10R-2 (Piece 1B, 12–15)	5	+			xxxx	x	x		x
17	11R-1 (Piece 10, 51–53)	5	+	+		xxxx	x	x		xx
19	12R-1 (Piece 14C, 136–140)	6				xxxx	xx	+		xx
18	13R-1 (Piece 10, 84–87)	6	+	+		xxxxx	+	+	+	xx
21	15R-1 (Piece 5, 50–53)	6		+		xxxx	xxx	+	+	x
20	15R-1 (Piece 9, 84–87)	7	+	+		xxxxxxx	+	+		x
22	17R-1 (Piece 2, 17–19)	7				xxxxx	xxxx	+		+
23	18R-1 (Piece 4, 23–26)	8	++	x		x				xxxxxxx

Notes: single + = <1% modal volume, multiple +'s = 1% modal volume each, single x = 5%–10% modal volume, multiple x's = 10% modal volume each. This table is also available in **ASCII.**

Table T4. Major and trace element concentrations determined by inductively coupled plasma–atomic emission spectroscopy, Hole 1243B.

	203-1243B-								
Core, section:	2R-1	3R-1	5R-2	6R-2	7R-2	9R-2	11R-1	15R-1	18R-1
Interval (cm):	23–25	116–118	16–17	102–104	54–57	135–138	58–60	84–87	24–26
Piece:	5	15	3	14	4A	6C	10	9	4
Unit:	1	3	3	3	4	4	5	7	8
Depth (mbsf):	108.83	114.36	124.33	130.1	139.31	149.85	157.08	176.74	190.44
Major element oxide (wt%):									
SiO_2	49.99	50.67	50.17	51.16	50.31	49.49	51.64	49.77	49.42
TiO_2	1.69	1.67	1.68	1.72	2.12	2.12	1.98	1.93	1.43
Al_2O_3	15.13	15.45	15.30	15.40	16.92	16.77	15.25	14.34	15.33
Fe_2O_3t*	9.73	10.22	10.11	8.88	9.25	9.45	9.62	13.65	12.17
MnO	0.18	0.17	0.18	0.16	0.15	0.15	0.17	0.17	0.17
MgO	7.25	6.43	6.51	7.29	5.92	5.74	6.11	5.89	6.55
CaO	12.56	12.11	12.51	12.02	10.66	11.74	11.66	10.89	12.18
Na_2O	3.04	2.94	3.01	3.08	3.57	3.42	3.04	2.93	2.48
K_2O	0.30	0.14	0.39	0.10	0.78	0.75	0.32	0.25	0.15
P_2O_5	0.12	0.19	0.15	0.18	0.32	0.36	0.21	0.18	0.11
Totals:	100	100	100	100	100	100	100	100	100
LOI	0.10	0.40	0.80	0.20	1.41	2.69	0.90	0.70	0.80
Mg#	63.5	59.4	60.0	65.7	59.9	58.6	59.7	50.2	55.6
Trace element (ppm):									
Ba	22	16	20	18	100	104	21	15	14
Cr	322	298	306	291	180	175	283	138	281
Sc	46	45	47	45	31	31	44	50	50
Sr	165	162	164	162	293	302	142	127	116
V	344	344	353	330	267	281	373	434	353
Y	37	35	37	40	38	37	46	46	36
Zr	135	130	125	133	205	204	147	139	94
Zn	67	62	61	68	61	98	106	103	80
Co	41	44	42	40	42	41	42	55	48
Cu	99	94	96	97	120	118	111	116	82
Nb	15	15	14	15	18	18	17	18	13
Ni	109	83	81	79	79	65	132	45	76

Notes: * = total iron as Fe_2O_3. LOI = Loss on ignition. Mg# = $Mg/(Mg+Fe^{2+}) \times 100$; Fe^{2+} estimated as 85% of total ions. This table is also available in **ASCII.**

Table T5. Summary of paleomagnetic analyses of cores recovered, Hole 1243B. (See table notes. Continued on next page.)

Core, section	Type	Max. treat. (mT)*	Depth in core (cm)	Depth (mbsf)	NRM without treatment (A/m)	Dec (°)	Inc (°)	MAD (°)	Interval used (mT)*	Mean Inc (°)	MAD (°)	Mean depth of sample (mT)
203-1243B-												
2R-1	Long	60	76	109.36	1.56	142.7	4.8	0.4	50–60			
		60	78	109.38	1.49	141.8	5.2	0.5	50–60			
		60	80	109.40	1.30	139.9	8.2	0.8	50–60	6.1	1.8	109.38
2R-1	Disc	70	78	109.38	1.94	–33.6	4.6	2.5	40–70	4.6	2.5	109.38
3R-1	Long	60	13	113.33	2.69	253.3	16.6	1.8	40–60			
		60	15	113.35	2.75	253.7	17.7	1.9	35–60			
		60	17	113.37	2.46	249.6	21.8	2.4	40–60	21.2	5.6	113.35
		60	19	113.39	2.31	243.6	28.9	1.9	50–60			
3R-1	Disc	70	14	113.34	3.51	57.6	–0.3	1.1	60–70	–0.3	1.1	113.34
3R-2	Disc	55	6	114.76	1.02	–13.0	0.5	0.5	50–55	0.5	0.5	114.76
3R-2	Disc	580°C	6	114.76	2.68	–6.7	6.9	6.5	500°–580°C			
3R-2	Long	40	84	115.54	2.21	44.9	18.5	1.0	35–40			
		40	88	115.58	3.10	51.1	28.9	0.8	35–40	23.7	7.3	115.56
3R-2	Disc	70	89	115.59	1.82	240.5	–9.1	5.6	50–70	–9.1	5.6	115.59
3R-2	Long	40	32	118.52	5.92	14.7	14.3	1.2	15–40			
		40	36	118.56	5.28	19.4	21.5	2.1	20–40			
		40	40	118.60	2.92	30.5	23.2	1.8	30–40			
		40	44	118.64	1.39	35.3	24.1	2.0	30–44	20.7	4.4	118.58
4R-2	Disc	70	70	120.40	2.31	246.9	21.9	5.1	35–70	21.9	5.1	120.40
5R-1	Disc	70	15	122.85	2.13	49.7	9.8	5.4	50–70	9.8	5.4	122.85
5R-1	Long	70	28	122.98	3.71	49.4	8.2	2.6	40–70			
		70	32	123.02	3.77	54.7	10.0	1.4	50–70			
		70	44	123.14	3.58	189.6	34.5	2.6	50–70			
		70	48	123.18	3.36	183.0	23.5	1.9	50–70	19.0	12.3	123.08
5R-1	Disc	55	47	123.17	4.31	7.5	2.0	0.4	50–55	2.0	0.4	123.17
5R-1	Disc	580°C	47	123.17	2.62	13.2	–0.5	2.0	425°–580°C	2.0	0.4	123.17
5R-2	Long	70	26	124.43	3.74	64.6	14.2	4.2	40–70			
		70	30	124.47	4.27	68.5	17.8	3.8	40–70			
		70	34	124.51	2.97	91.8	22.2	2.1	50–70			
		70	32	124.49	3.64	73.9	22.9	4.4	40–70			
		70	38	124.55	2.52	125.0	11.5	1.1	50–70			
		70	42	124.59	3.14	125.6	8.6	1.2	50–70	16.2	5.8	124.51
6R1	Disc	70	69	128.39	6.56	56.3	4.5	3.0	60–70	4.5	4.5	128.39
7R-1	Disc	55	106	138.46	2.93	268.1	–1.0	0.8	50–55	–1.0	0.8	138.46
7R-2	Long	50	10	138.87	2.44	222.4	19.3	2.4	40–50			
		50	12	138.89	2.83	222.3	21.5	2.6	40–50			
		50	14	138.91	2.89	222.6	23.6	2.6	40–50			
		50	16	138.93	2.63	223.0	24.7	2.4	40–50	22.3	2.4	138.90
7R-2	Long	50	38	139.15	4.05	–19.9	7.9	6.1	35–50			
		50	40	139.17	5.60	–17.1	6.5	4.6	35–50			
		50	42	139.19	6.80	–15.3	5.3	3.7	35–50	6.6	1.3	139.16
7R-2	Long	50	58	139.35	7.09	254.0	8.3	0.6	35–50			
		50	62	139.39	4.66	258.6	12.4	1.8	35–50			
		50	64	139.41	3.73	263.3	15.8	3.0	35–50			
		50	66	139.43	3.10	268.5	15.7	4.0	35–50	13.0	3.5	139.40
7R-2	Long	50	90	139.67	4.66	–10.8	6.7	4.2	40–50			
		50	94	139.71	5.56	–15.8	9.9	5.6	40–50	8.3	2.3	139.69
7R-2	Disc	55	96	139.73	3.26	191.3	1.1	1.0	50–55	1.1	1.0	139.73
7R-3	Long	50	4	140.26	4.62	146.4	6.1	0.2	40–50			
		50	8	140.30	5.99	146.9	4.7	0.3	40–50			
		50	12	140.34	5.62	148.9	4.6	0.3	40–50	5.1	0.8	140.30
7R-3	Long	50	22	140.44	5.59	9.6	3.5	0.2	40–50			
		50	26	140.48	6.32	12.2	7.7	0.4	40–50			
		50	30	140.52	5.07	15.8	11.3	0.8	40–50			
		50	34	140.56	4.29	18.3	14.2	1.1	40–50			
		50	38	140.60	4.43	18.3	17.5	2.7	35–50			
		50	42	140.64	5.90	18.7	14.5	2.2	35–50			
		50	46	140.68	6.52	19.2	11.0	1.6	35–50	11.4	4.7	140.56
7R-3	Disc	55	37	140.59	4.74	192.9	0.1	10.0	55	0.1	10.0	140.59
9R-1	Disc	55	11	147.11	3.49	51.8	6.9	0.1	50–55	6.9	0.1	147.11
9R-1	Long	55	132	148.32	2.28	263.9	11.0	3.4	35–50			
		55	134	148.34	2.81	254.5	9.4	2.3	40–50			
		55	136	148.36	3.05	248.3	8.4	1.7	40–50	9.6	1.3	148.34
9R-2	Disc	55	12	148.62	5.65	222.0	–2.1	0.4	50–55	–2.1	0.4	148.62
9R-2	Disc	580°C	12	148.62	5.44	220.9	–0.3	1.5	400°–580°C	–2.1	0.4	148.62

Table T5 (continued).

Core, section	Type	Max. treat. (mT)*	Depth in core (cm)	Depth (mbsf)	NRM without treatment (A/m)	Dec (°)	Inc (°)	MAD (°)	Interval used (mT)*	Mean Inc (°)	MAD (°)	Mean depth of sample (mT)
9R-2	Long	50	18	148.68	3.94	79.1	5.5	0.6	35–50			
		50	22	148.72	3.14	91.2	6.2	2.4	40–50			
		50	26	148.76	2.81	88.2	6.9	2.6	40–50			
			30	148.80	1.80	86.4	9.9	3.2	40–50	7.1	1.9	148.74
9R-2	Disc	55	75	149.25	3.34	13.7	–1.3	1.1	50–55	–1.3	1.1	149.25
9R-2	Long	50	50	149.00	2.72	159.3	2.7	2.5	40–50			
		50	55	149.05	3.44	160.4	2.1	2.2	40–50			
		50	60	149.10	2.02	162.0	0.5	2.7	40–50			
		50	65	149.15	2.07	278.6	2.6	6.3	35–50			
		50	70	149.20	1.59	227.7	7.0	3.0	35–50			
		50	75	149.25	2.51	196.2	2.5	3.1	35–50			
		50	80	149.30	1.98	189.7	3.4	2.3	40–50			
		50	85	149.35	1.11	190.2	4.7	2.0	40–50			
		50	90	149.40	1.94	205.3	3.5	1.2	40–50			
		50	95	149.45	3.65	234.2	5.0	0.4	40–50			
		50	100	149.50	4.03	238.1	4.6	0.3	40–50			
		50	105	149.55	4.01	239.6	4.1	0.2	40–50			
		50	110	149.60	2.81	239.0	4.2	0.3	40–50			
		50	115	149.65	1.67	233.1	4.8	0.3	40–50			
		50	120	149.70	2.00	235.1	3.8	0.4	40–50	3.7	1.5	149.35
9R-2	Long	50	140	149.90	4.67	243.4	4.7	0.3	40–50			
		50	142	149.92	5.41	244.0	4.9	0.5	40–50			
		50	144	149.94	7.09	245.3	5.9	1.0	40–50	5.2	0.6	149.92
10R-1	Disc	55	27	151.77	2.92	270.0	3.9	1.1	45–55	3.9	1.1	151.77
10R-2	Disc	55	9	152.83	1.52	187.0	–49.0	0.2	50–55	–49.0	0.2	152.83
10R-2	Long	50	10	152.84	3.07	9.3	–28.0	1.9	40–50			
		50	14	152.88	3.01	7.8	–25.0	1.8	40–50	–26.5	2.1	152.86
10R-2	Long	50	20	152.94	2.52	9.6	–23.9	1.8	40–50			
		50	25	152.99	2.67	14.5	–22.8	1.6	40–50			
		50	30	153.04	2.90	17.7	–18.6	0.6	40–50	–21.8	2.8	152.99
11-R1	Disc	55	90	157.40	3.41	159.7	–3.3	3.4	40–55	–3.3	3.4	157.40
12R-1	Disc	55	85	160.45	1.93	75.3	–12.7	2.0	40–55	–12.7	2.0	160.45
12R-1	Disc	55	88	160.48	6.13	72.8	–5.7	1.0	50–55	–5.7	1.0	160.48
12R-1	Disc	580°C	88	160.48	2.25	86.0	–11.6	2.8	425°–580°C	–5.7	1.0	160.48
12R-1	Long	50	40	160.00	1.62	48.6	–5.7	1.9	40–50			
		50	44	160.04	2.70	53.6	–3.2	1.9	40–50			
		50	48	160.08	2.76	50.3	–1.5	1.6	40–50	–3.5	2.1	160.40
12R-1	Long	50	130	160.90	4.07	109.0	0.0	0.6	35–50			
		50	132	160.92	5.29	108.4	0.4	0.9	35–50			
		50	134	160.94	5.89	107.5	1.2	1.2	35–50	0.5	0.6	160.92
13R-1	Long	50	34	166.44	NA	306.0	0.8	0.8	40–50			
		50	36	166.46	NA	305.8	3.5	0.6	40–50			
		50	38	166.48	NA	305.1	6.1	0.6	40–50			
		50	40	166.50	NA	304.5	9.5	0.6	40–50	5.0	3.7	166.47
13R-1	Disc	55	62	166.72	8.37	59.6	–18.6	0.4	30–55	–18.6	0.4	166.72
14R-1	Disc	55	36	171.16	8.18	–42.9	–3.5	0.8	45–55	–3.5	0.8	171.16
15R-1	Disc	55	7	175.97	6.55	34.5	17.0	1.7	45–55	17.0	1.7	175.97
15R-1	Disc	55	98	176.88	0.67	225.5	13.0	0.5	40–55	13.0	0.5	176.88
15R-1	Disc	580°C	98	176.88	1.06	248.3	19.1	6.0	375°–580°C	13.0	0.5	176.88
17R-1	Disc	55	17	185.57	0.69	266.9	17.4	1.0	45–55	17.4	1.0	185.57

Notes: All values mT, except where noted. Natural remanent magnetization (NRM) intensity without treatment, ChRM direction (Dec [Declination] and Inc [Inclination]), and maximum angular deviation (MAD) angle (which is a measure of how well the vector demagnetization data fit a line) are listed for selected basalt pieces. Long = long core section, Disc = discrete sample. * = except where noted. NA = not available. Max. treat. = maximum treatment. This table is also available in **ASCII.**

Table T6. Summary of physical properties of basalt samples, Hole 1243B.

Core, section, interval (cm)	Depth (mbsf)	Wet bulk density (g/cm^3)	Grain density (g/cm^3)	Porosity (%)	Sonic velocity (km/s)
203-12343B-					
2R-1, 78–80	109.38	2.67	2.81	7.6	5.30
3R-1, 14–16	113.34	2.82	2.90	4.1	5.67
3R-2, 89–91	115.59	2.78	2.88	5.1	5.49
4R-1, 33–35	118.53	2.79	2.88	5.0	5.39
4R-2, 70–72	120.40	2.75	2.85	5.5	5.44
5R-1, 15–17	122.85	2.74	2.84	5.5	5.54
6R-1, 69–71	128.39	2.77	2.86	5.0	5.70
7R-1, 106–108	138.46	2.64	2.98	17.1	4.27
7R-2, 96–98	139.73	2.58	2.73	8.8	5.11
7R-3, 37–39	140.59	2.58	2.74	9.7	4.92
9R-1, 11–13	147.11	2.52	2.64	7.7	5.26
9R-2, 75–77	149.25	2.55	2.70	9.1	4.95
10R-2, 9–11	152.83	2.64	2.79	8.8	5.23
11R-1, 90–92	157.40	2.72	2.84	7.0	5.56
12R-1, 85–87	160.45	2.68	2.82	7.9	5.38
13R-1, 62–64	166.72	2.54	2.73	11.4	5.00
14R-1, 36–38	171.16	2.62	2.86	13.1	5.09
15R-1, 7–9	175.97	2.78	2.87	4.6	5.30
17R-1, 17–19	185.57	2.80	2.91	6.1	5.51
18R-1, 38–40	190.58	2.80	2.87	4.0	5.50

Note: This table is also available in **ASCII.**

Table T7. Well Seismic Tool data summary, Site 1243B.

Station	Depth (mbrf)	Depth (mbsf)	Traveltime (ms)	*N*
1	4044	176	2664.16 ± 0.11	16
2	4034	166	2661.63 ± 0.09	11
3	4024	156	2658.62 ± 0.12	11
4	4014	146	2656.16 ± 0.11	12
5	4004	136	2653.77 ± 0.11	11
6	3994	126	2651.88 ± 0.09	11
7	3984	116	2649.65 ± 0.12	12
8	3979	111	2646.50 ± 0.21	5

Note: This table is also available in **ASCII.**

Table T8. Well Seismic Tool interval velocities, Hole 1243B.

Stations interval	Depth interval (mbsf)	ΔZ (m)	ΔT (ms)	Velocity* (km/s)
1–2	166–176	10	2.53 ± 0.14	3.95 ± 0.22
2–3	156–166	10	3.01 ± 0.15	3.32 ± 0.17
3–4	146–156	10	2.46 ± 0.16	4.07 ± 0.27
4–5	136–146	10	2.39 ± 0.16	4.18 ± 0.27
5–6	126–136	10	1.89 ± 0.14	5.29 ± 0.40
6–7	116–126	10	2.23 ± 0.15	4.48 ± 0.30
7–8	111–116	5	3.15 ± 0.24	1.59 ± 0.12

Notes: * = velocity; velocity = $\frac{\Delta Z}{\Delta T}$. This table is also available in ASCII.

Table AT1. Recovered glass samples, Hole 1243B.

Core	Rock piece number	Glass samples number			Alteration	Veins
		Total	Oriented			
			UGZ	LGZ		
203-12343B-						
1R	0	0	0	0		
2R	14	2	1	0		
3R	28	2	1	0		
4R	38	5	1	0	Moderate	Brown
5R	28	1	1	0		
6R	38	4	1	1		
7R	34	4	1	0	Moderate	White
8R	27	7	1	0		
9R	28	4	0	0	Moderate	White
10R	28	4	0	0		
11R	24	2	1	0		
12R	18	2	0	1		
13R	13	3	1	0		
14R	28	3	0	0		
15R	11	0	0	0		
16R	1	0	0	0		
17R	2	0	0	0		
18R	9	3	0	0		
19R	0	0	0	0		
Total	359	46	9	2		

Note: UGZ = upper glass zone, LGZ = lower glass zone.